Department of Precision and Microsystems Engineering

Design of a next generation Schottky field emission gun with improved operation- and beam stability.

L.A. Musters

Report no : 2020.038
Coach : Ir. J. P. Kappelhof
Professor : Prof. Dr. Ir. J. L. Herder
Specialisation : Opto-Mechatronics
Type of report : Master of science Thesis
Date : September 24, 2020

Design of a next generation Schottky field emission gun with improved operation- and beam stability.

by

L.A. Musters

to obtain the degree of
Master of Science
at the Delft University of Technology,
to be defended publicly on Thursday September 24, 2020 at 14:30 AM.

Student number:	4354311	
Project duration:	October 1, 2019 – August 31, 2020	
Thesis committee:	Dr. Ir. L. A. Cacace	TU Delft,
	Dr. Ir. A. C. Zonnevylle,	Raith B.V., supervisor
	Dr. Ir. N. Bhattacharya,	TU Delft
	Prof. Dr. Ir. J. L. Herder	TU Delft
	Prof. Dr. Ir. P. Kruit,	TU Delft

This thesis is confidential and cannot be made public until September, 24, 2022.

An electronic version of this thesis is available at `http://repository.tudelft.nl/`.

TU Delft

Abstract

The manufacturer of an electron beam lithography machine pushes a better understanding and higher performance of the optical column to provide a better product with each iteration. At the heart of the column is the source of electrons: the gun lens. It holds the field emitter from which the electrons originate and accelerates the beam to a first crossover. The main work in this thesis was concerned with development of a new and better gun lens design. Considerations of several physical phenomena is required in order for the gun lens to be more robust and with a more stable beam. It was found that the heating transient plays a large role in the operation of the gun lens. By defining the requirements clearly including by ray-tracing the optical geometry to find optical sensitivities, the main challenges of the project became evident. A new concept design is presented where the heat transport inside the gun lens is improved and thermal drift is greatly diminished. By using the ceramic insulators as flexures the short- and long-term stability of the lenses are improved and the thermal transient settling time is reduced from 26 hours to below 6 hours. By opening up the geometry inside the gun lens the local vacuum at the emitter is much better, which increases its lifetime. The electrostatic fields are made much more robust by burying the triple junction, which required using a new insulator shape. The final result is a gun lens concept design which improves in all aspects while remaining simple in construction.

Acknowledgements

Many thanks to both Pieter Kappelhof and Christiaan Zonnevylle who have taught and shown me not only many aspects of scientific research, but also how to operate in an industry environment. Because of their help and knowledge I can be as proud as I am of my work today. Also a big thanks to Lennino Cacace, who assisted me and asked critical questions to show me where I could improve.

Contents

1 Introduction

The push for going faster, smaller and cheaper in the semi-conductor industry has not skipped Raith B.V. [43], a producer of Electron Beam Lithography (EBL) machines. One of their work horses - the EBPG series - is constantly being improved to be competitive and provide higher value to customers. As preparation to future changes, this graduate project was established to have a look at the gun lens inside the machine for improvements. Contrary to many approaches to electron optical designs, this project was approached from the angle of a mechanical engineer; everything has to perform 'perfectly', even when it has to be manufactured by imperfect machines. Because of this contradiction, the report contains many trade-offs that are necessary in order to end up with a design that is as good as it can be while being realistic.

I may have lost you already at some of the jargon in the previous paragraph. Luckily, this chapter will be dedicated to provide a baseline of knowledge. The remainder of the report uses this information and terminology to avoid cumbersome explanations later on. The chapter moves from a global look at the machine to detailed information. Details of the machine have been written down before; the preceding literature study (appendix A) includes many details on the system and gun lens, and a different graduate project focused around the metrology system at the wafer stage [55]. Some of these details will be repeated here to provide clarity.

1.1. EBPG

Raith produces and develops two machines in Best, The Netherlands called the EBPG5150 and EBPG5200, see 1.1. The different numbers indicate the usable wafer size (150mm and 200mm respectively), and is for this graduate project not relevant, as both columns are identical. Therefore they are grouped under a common name, the EBPG. The machines are used to write nanostructures onto wafers using a process called Electron Beam Lithography (EBL), which is shown schematically in Figure 1.2 and roughly works as follows. A thin layer of material is spread out over the wafer, called 'resist'. The machine then exposes specific areas of the resist to an electron beam for a fraction of a second, changing the material properties locally. The pattern that is left at the end can be developed by washing away the unexposed resist and a nanostructure remains. The structures are used for various purposes. The EBL can be used to create custom nanostructures without the need for a mask pattern, reducing the initial investment cost to create a structure on the wafer.

To see how the EBPG can perform EBL accurately and quickly, we start on a global level. The machine holds the wafer at a very high precision in the wafer stage, and generates the electron beam using the column. Both of these are suspended in high vacuum, although at different levels. Electrons get absorbed by molecules when they interact and therefore the system is kept on a strict no-air diet to ensure the entire electron beam can travel through to the wafer. The wafer stage enjoys a 'comfortable' 10^{-5} mbar pressure, while some parts of the column go down to a 10^{-9} mbar. Reaching this vacuum is not trivial; hardware store vacuum pumps perhaps reach 1% of ambient pressure, while in this situation 0.0000000001% is necessary. Several interesting physical effects take place at this amount of nothingness, see section 2.2.

Leaving the wafer stage for what it is and zooming in on the column several major parts can be found inside. First there is the generation of electrons, which happens at the tip of a tungsten wire inside the gun lens called a Schottky emitter, see section 1.3. The electrons are then guided down the column, interacting with several correction mechanisms and lenses before ending at the wafer. To understand how these can

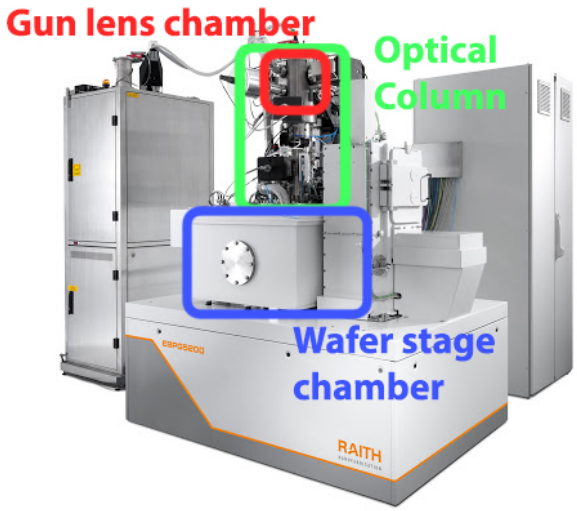

Figure 1.1: The EBPG5200.

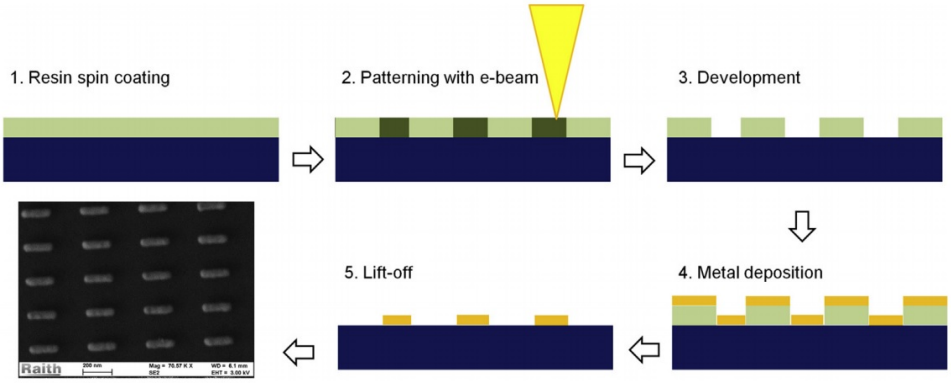

Figure 1.2: [19] An example of a the E-beam lithography process, where gold nanorods are deposited as a result.

manipulate electrons the next section is dedicated to electron optics. For much more in-depth information than is given here regarding the EBPG column, see appendix A. General information on electron optics can be found in [42] [30].

1.2. Electron optics

Electron optics (EO) falls under the umbrella term charged particle optics (CPO), which includes other things like ions. Charged particles can be manipulated by using the electromagnetic field. This field exerts a force on the particles. Clever shaping of these fields creates a functional electrostatic lens. Although both are instrumental to the EBPG, magnetic lenses will not be discussed further, as it adds unnecessary information. The most important system to understand is the gun lens, which is purely electrostatic.

A simple lens

The electrostatic lenses that will be discussed here are rotational symmetric. Figure 1.3 shows a cross-section of a simple lens. This lens was simulated using SIMion [47], a first order CPO ray-tracing program. The green and purple solids in the shape of a flat doughnut are electrodes; the parts both have a potential applied to them. Because of their potential difference an electrostatic field is formed in between. The path of electrons are going from left to right and are shown in black, and the electrostatic field is shown in red. This lens is called an decelerating lens; the electrons slow down while going through it. Their potential starts as 500eV. As they cross the field lines, they are effectively going 'uphill' (as they are negatively charged, they are repelled by a lower potential!) and lose some energy while doing so. At the end, only 70eV is left. Now the question remains why a focal point is observed if only deceleration was the intended purpose. The force vector is dependent

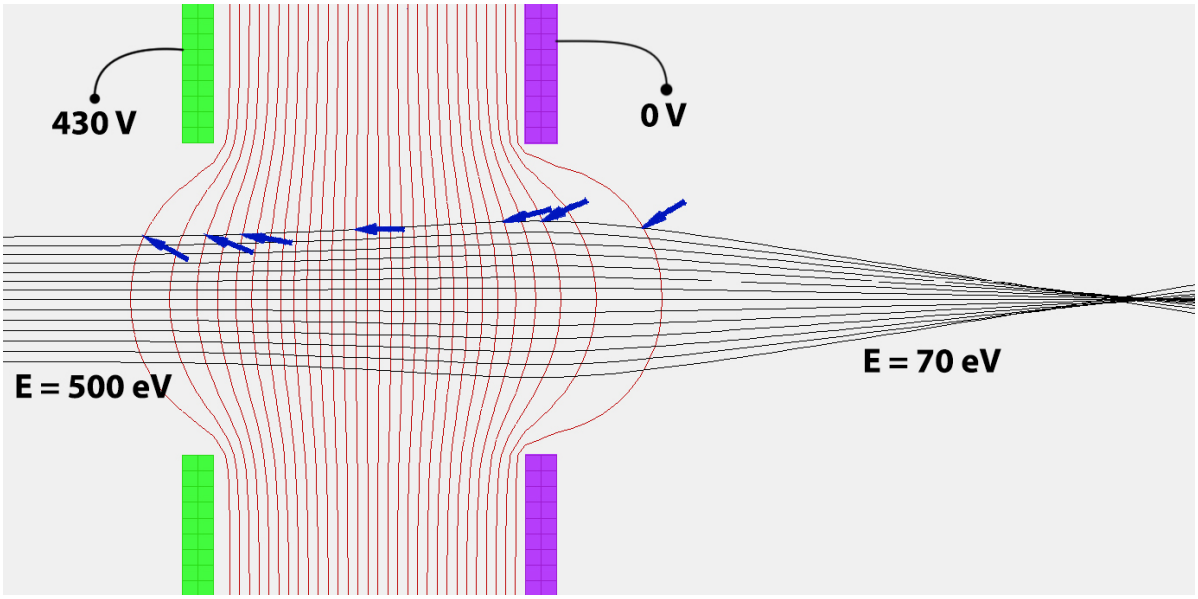

Figure 1.3: An example of an electrostatic lens.

on the local field direction. This is visualized with the blue arrows. Due to the inevitable field leaking at the entrance and exit of this lens, some curvature is created in the field lines. This curvature pushes the electrons radially. As the beam potential is higher at the lens entrance, the outwards force is not as effective in changing the momentum. However, once the electrons have slowed down, the inwards forces at the lens exit have a much greater effect on the beam path, and a net deflection inwards can be observed, which creates a focal point.

Aberrations

In the simple example of the previous subsection it can be seen that the focal point is actually not a single point, but already has some blur attributed to it. This lens suffers from spherical aberration; something which cannot be corrected for in simple electrostatic lenses [46], as the shape of the electrodes can not be made such that the field lines perfectly focus to one point. Another effect is chromatic aberration, which is equivalent to light optics when the source is not monochromatic. As these effects cannot be corrected for, they often contribute quite a lot to the final spot size of a system. Both of these effects scale with the final aperture angle α_{im} [30], see equation (1.1) for example. It is the equation for the confusion circle caused by spherical aberration present in a lens with spherical aberration coefficient C_s. For this reason EO systems often works with a very small aperture angle to reduce this effect, in the range of milliradians. This has other negative implications. For example diffraction actually benefits from a larger aperture angle. These effects have to be balanced to create the overall smallest spot size. The total probe size that can be expected at the wafer can be calculated using equation (1.2) [31]. It uses the image size d_I, the diffraction spot d_A, the contribution from spherical aberration d_s and chromatic aberration d_c. The equations to find their magnitude can be found in A [31].

$$d_s = 0.18 C_s \alpha_{im}^3 \tag{1.1}$$

$$d_p = ((d_I^{1.3} + (d_A^4 + d_s^4)^{1.3/4})^{2/1.3} + d_c^2)^{1/2} \tag{1.2}$$

Adding to the aberrations, CPO suffers from the charged nature of the beam. As the particles have a charge, they emit their own electrostatic field. This will cause individual particles to interact. This effect is called Coulomb interactions, and is generally an unwanted effect in electron beams, as it reduces the beam quality. The magnitude of these effects increase with the current and decrease with higher beam potential [26]. Intuitively it makes sense; if there are more electrons and at lower velocity, they will push each other around more during travel. Depending on the beam characteristics, the interactions either increase or decrease with the aperture angle. In EO systems with high currents, these effects can contribute heavily to the spot size if no measures are taken to prevent it. These effects are added to the final probe size d_p in dif-

ferent ways. One called Boersch effect, increases the chromatic aberration, while another called trajectory displacement creates an additional confusion circle, which is added quadratically to (1.2). A third effect - the so-called space charge - results in a defocus of the beam. As this can be corrected by the adjustment of lens excitations, this effect is not as relevant for the EBPG. The measures taken in the EBPG column are discussed in section 1.3.

Unwanted consequences of lenses

The electrodes in a lens discharge between each other if the electrostatic field breaks down. These discharges shut down the machine, halting production. There are several mechanics that cause the breakdown of the field and in short they are all related to the surface finish of the electrodes (which should be as smooth as possible, without local micro-protrusions) and the local contaminations in the vacuum. If those two aspects can be controlled, and the field in between two electrodes is not too high, the discharges can be prevented. More details are given in subsection 2.3.1.

The information in this section is kept to what is deemed necessary. In Appendix A more types of lenses are discussed and in more detail, and the on-axis aberration types (spherical, chromatic, diffraction, coulomb interactions) are explained thoroughly. This includes how to calculate them and how to create a model that will provide the ray-tracing data that is required, as any practical EO system cannot be modelled analytically. Educational references to electron optics can also be found online [12, 30].

1.3. Column

Walking through the parts

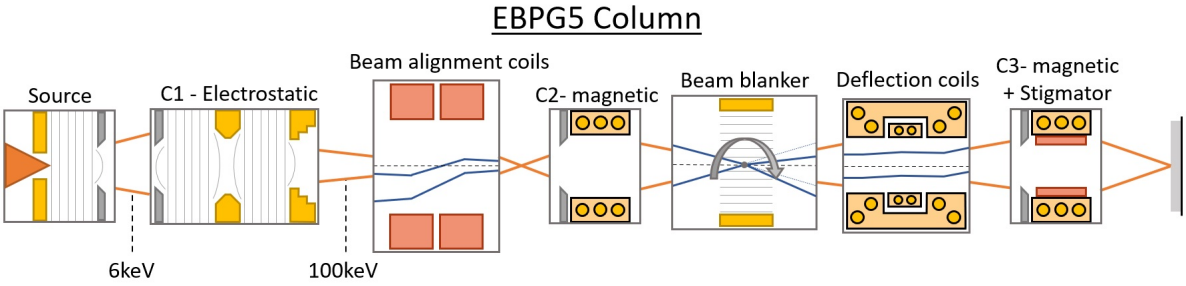

Figure 1.4: A schematic of the EPBG column, showing the optical components. The gun lens is a combination of the 'Source' and 'C1 - Electrostatic' boxes. In total the column has three crossovers: one before C2, one after and finally the probe.

Transitioning from lens theory, the column of the EBPG is schematically shown in Figure 1.4. The specific layout of the column has been openly developed and discussed in literature [28, 29]. Again starting big, **the source** of the electrons is shown on the left, which is constantly on throughout operation. The gun lens holds this source and at the same time is also responsible for the first focussing action, which we call **the C1 lens**. When the electrons exit the source, the beam energy is about 6keV. To decrease the aberrations (specifically diffraction and coulomb interactions) the beam is accelerated to 100keV using the gun lens and anode, more on that in section 1.4.**The beam alignment coils** can move the beam however necessary in 4 degrees of freedom to align the beam with the rest of the column. The parameter are determined during the calibration procedure in Best before the machine is sent to the customer.

After that the aligned beam enters **the second lens** - called C2 - which is magnetic and focuses it to the centre of **the beam blanker**. This is done for a good reason: as mentioned before, the source is always on and would therefore always shine a spot onto the wafer. To turn the beam off at the wafer (if the beam should be moved to a different location on the wafer without writing), the system uses conjugate blanking. By activating an electrostatic field between two parallel plates at the conjugate crossover of the probe, the electron are pushed to one side and will no longer cross the aperture at the third lens. It is very important that this happens at a crossover of the beam, such that only a pure pivoting action occurs. Otherwise, the probe will move around while being blanked and an unwanted line appears on the product. This system is required because simply turning off the source is not possible as it experiences transitioning effects during start-up that last many hours [5].

Next, the beam continues to **the deflection coils**, which take care of the writing process. The mainfield deflection is a larger and slower coil, which moves the beam to a sub-square on a $1x1mm^2$ area where the system can write. Within that sub-square the smaller and faster subfield deflection coil is used to write the patterns. This is repeated until the writing in the area has been completed, after which the wafer stage is moved to the next area.

Lastly, **the third and final lens** is responsible for imaging the probe onto **the wafer**. Within this lens a stigmator is present. It can correct for previously unexpected 'built up' astigmatism in the beam, and also corrects the astigmatism caused by the deflection fields [17].

Coulomb interactions mitigation

All the major lenses C1, C2 and C3 have an aperture (the grey razorblades in Figure 1.4) that limits the current. This is to improve the coulomb interactions; only a very small fraction of the current coming from the source propagates to the probe, and all the additional current only serves to mess up the beam quality through coulomb interactions. Therefore it is beneficial to cut off current as much and as soon as possible.

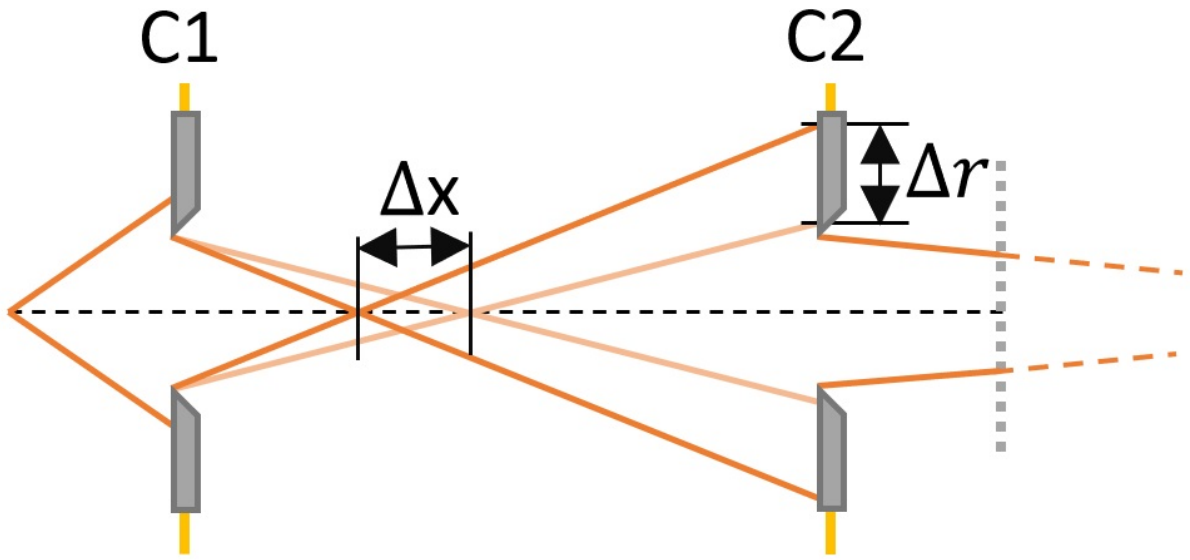

Figure 1.5: Visualisation of how the focal point of C1 can determine the amount current crossing the C2 aperture. Movement of Δx results in a beam radius change at the aperture of Δr. The magnification is also decreased when the focal point is pulled back. The geometry of the beam after C2 is independent of the first crossover.

Variable focus scheme

So far almost the full geometry has been defined for the column, except for 1 thing: the first crossover after the C1 lens. This is done for a very specific reason. CPO lenses being what they are means that you can change their lens strength without changing their geometry, but just by changing the potential of the electrode, or in the case of the magnetic lens the current. The first crossover point can be moved along the optical axis around while keeping the rest of the system identical by changing the lens strength of C1 and C2, see figure 1.5 for a schematic. Doing so will change the entrance angle at C2 and thus the amount of current that passes through the aperture. Since the beam geometry is constant after C2, the movement of C1 will change what amount of current propagates to the probe! Secondly, the magnification of the system is also changed, producing a smaller probe when less current passes and vice versa. A variable probe size with variable current can thus be achieved. This is useful for the customer as they can do broad strokes with a large probe size, and fine detail with a small probe size whenever they like. To really visualize this the magnification, probe size and current data can be extracted as a function of the lens excitation. The data is extractor from the preceding literature study. Results are shown with probe current on the x-axis in Figure 1.6.

1.4. Gun lens

Now that the overall function of the column is explained, we can focus in on the gun lens and how it executes its functions. A cross-section of the current gun lens is shown in Figure 1.10. The main functions of the gun

Figure 1.6: Some results from Appendix A which will be used throughout this thesis. Note that these parameters sometimes vary more than two orders of magnitude across the operational range of the EBPG.

lens are the source of electrons, and the lens action of C1, which also accelerates the beam. All of these elements have to be aligned properly, and stay aligned to a certain degree while under the influence of dynamics and temperature variations. If these cannot be guaranteed, the quality of the beam deteriorates more than is acceptable by Raith. For more detail on these requirements, see chapter 3.

Emitter

Starting at the source: a tungsten tip, see Figure 1.7. This tip emits electrons because it is motivated to do so; Whenever the energy of an electron inside the material exceeds the potential energy just outside it, it can 'jump' out as described by [5], see figure 1.8. The energy of the electrons is increased by heating the tip to 1800K, and the energy barrier between the material and the vacuum - also called the work function - is decreased by the smart selection of materials; the tip has a ZrO_x mono-layer and the tungsten has its

{100} crystal plane at the tip end. This mono-layer can be supplied by fresh ZrO_x from the reservoir on the tungsten wire through surface diffusion. Lastly, by applying a strong field at the tip, the vacuum potential at the tip is decreased which drastically improves the emission properties. The combination of all these factors is called Schottky emission. The vacuum at the tip should be sufficiently low; 1×10^{-9} mbar is the operational requirement [42]. However, safe operation is already possible at 1×10^{-8} mbar from experience by Raith.

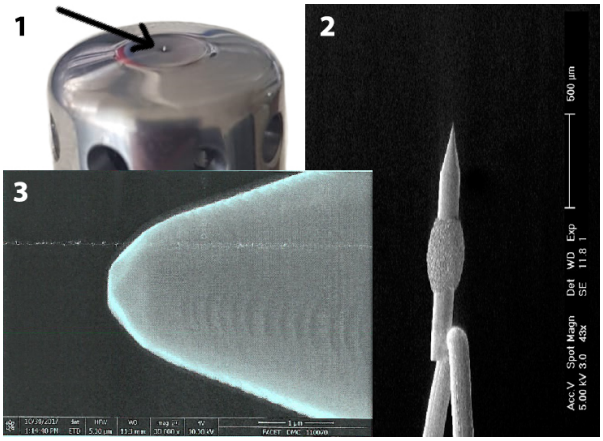

Figure 1.7: From Appendix A: "1 The emitter from Thermo-Fischer used by Raith B.V For their EBPG. 2 [9] An electron microscope image of a Schottky tip. Also in the image is the ZrO_x reservoir and the legs to provide a heating current. 3 SEM image of a typical Schottky tip delivered by Thermo-Fischer.

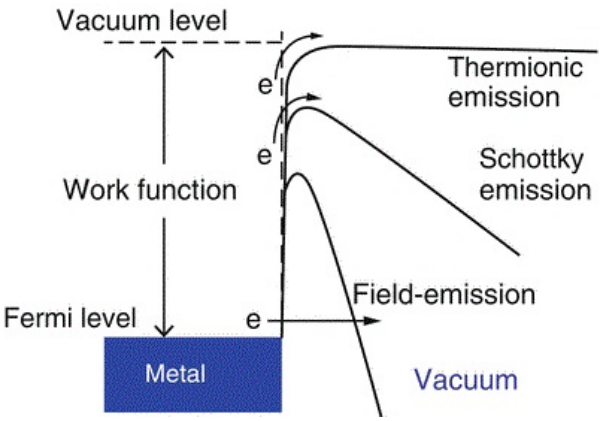

Figure 1.8: [13] A picture showing how electrons can exit a metal into vacuum using different techniques.

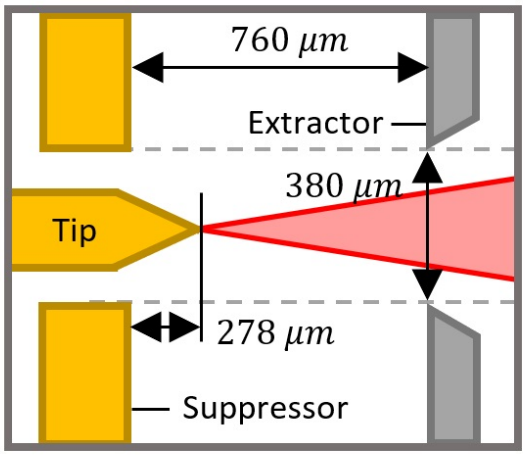

Figure 1.9: Standard geometry around the tip. Note that the proportions are not correct.

The consensus about the optimal geometry of the area around the Schottky tip for optimal performance is pretty clear and is given in Figure 1.9. These were found through geometry variation studies such as [56]. The suppressor, extractor and tip are given different potentials to generate the electrostatic fields. The sharpness of the tip (radius of $1\mu m$) creates a large field magnification, many times higher than the macroscopic field around it. The manufacturer of the source used by the EBPG is Thermo-Fischer [15], which deliver a integrated suppressor-tip combination. They also indicate standard potentials for the suppressor and extractor to generate the field, which are varying around -400V and 6300V relative to the tip respectively. These potentials can be adjusted to tweak the field which is necessary if the geometry is not perfect. This is also performed during calibration.

The Schottky emitter is certainly not the only emitter which could be used [31] [58]. Table 1.1 shows a comparison of three emitters on some important aspects. One of the most important aspects to consider for this system when picking a source is the maximum brightness. Brightness in electron optics is a measure of

how much current one can emit from an area (in this case the virtual source size d_v) into a certain solid angle, and is equivalent to the brightness in light optics. If the brightness is corrected for the beam potential V, it is constant across the system if coulomb interactions are zero (one part of coulomb interactions, trajectory displacement, results in the degradation of brightness). Using that assumption, brightness B_r determines directly how much current I_p will end up in a certain probe size at the wafer stage, as shown in equation (1.3), with the system magnification M. A higher brightness thus means faster writing times, as the exposure time of the relevant areas go down.

$$I_p = B_r \frac{\pi}{4}(Md_v)^2 \pi \alpha_l^2 V \tag{1.3}$$

Type of source	LaB_6 thermionic	Schottky emission	Cold field emission
Material	LaB_6	ZrO/W	W
ϕ (eV)	2.7	2.8	4.5
T (K)	1800	1800	300
E (V/m)	low	$\approx 10^8$	$> 10^9$
$J_e(A/m^2)$	$\approx 10^6$	$\approx 10^7$	$\approx 10^9$
$B_s(A/m^2/sr)$	$\approx 10^{10}$	$\approx 10^{11}$	$\approx 10^{12}$
d_s (um)	≈ 10	≈ 0.02	≈ 0.01
Vacuum (Pa)	$< 10^{-4}$	$< 10^{-7}$	$\approx 10^{-8}$
Lifetime (h)	≈ 1000	$\approx 10^4$	$\approx 10^4$
ΔE (eV)	1.0	0.5	0.3

Table 1.1: Comparison table for different emitters [12]. LaB_6 Was the technology used by Raith B.V. before the upgrade to the Schottky emitter.

It may be quite surprising then to find that the brightness of a Schottky emitter is not the highest of all common electron sources. However, it has several other great advantages such as stability and easy of operation that make it an obvious choice for the application, where long and reliable writing times are required . The cold field emitter has superior brightness, but the problematic current stability makes it unsuitable for long writing times [58]. The lifetime of the Schottky emitter is typically limited by the change of the shape on the tip [42] [5]. This is dependent on the operational settings, which includes the local pressure. At higher pressures, the so-called rate of {100} plane collapse of the tip increases. Simply put, this will increase the radius of the tip. Sufficient dulling will increase the virtual source size of the tip and reduce the field enhancement, reducing the brightness. A natural end of the tip life is the evaporation of the ZrO_x monolayer reservoir. However, from practical environments it is seen that plane collapse is the limiting lifetime effect. Improper handling of the vacuum can also create more catastrophic failures, see section 2.3.1.

The lens part of the gun lens

The electrons exit the tip with distribution in energy, but also in solid angle [5]. Flying through the extractor hole and into a field free region, they meet the first aperture of the system, see figure 1.10. This aperture is currently 0.4mm in diameter, but can be changed to alter the passing current. The aperture is the same potential as the extractor (hence the field free region), and is the starting aperture of the acceleration lens, accelerating the beam to 100keV. The exit aperture is the anode. As the electrons are negatively charged, the gun lens is on negatively charged with respect to the anode such that they can accelerate towards 100kV. In between the two apertures a large third electrode is placed, which we call the C1 lens. By having a different potential, it creates additional curved field lines inside the acceleration lens. This lens can influence the focal point of the gun lens, which is necessary for the variable current feature of the column.

Practical gun lens elements

Additional elements are shown in Figure 1.10 that have not yet been discussed. To hold the aperture in its place, a component called the aperture seat is used. The seat significantly alters the field lines which meet the electron beam, being so close to the optical axis. Therefore it has an influence on the gun lens performance.

So far the components which have been discussed are all part of the package which has to be copied over to the new design. As long as they offer the same optical performance, their shapes can be altered. For more details on these module requirements, see chapter 3. Other components are not required to be used, but they

Figure 1.10: Cross-section of the gun lens excluding the anode. Additional elements are given indicated by numbers. 1) Aperture clamp 2) Emitter seat 3) lens stack clamping bolt 4) Titanium shield ring 5) Kovar lens interface 6) Kovar ring 7) Electrical connections.

will be discussed here nonetheless as most of them will probably find their way into the new design one way or another.

One vital aspect of the gun lens is to keep the components with different potentials separated. This is done with insulators. In Figure 1.10 these are given in yellow. As can be seen, the extractor and aperture seat are not separated by an insulator as they have the same potential. The material of the insulators have several strict requirements depending on the specific implementation, one being a very high electrical resistivity. For more information, see section 2.3.

Other components are greyed out as they serve purely mechanical purposes. Going from the bottom to the top in Figure 1.10, the first grey part we find is a clamp (1) used to hold down the aperture into its seat. The second part is called the emitter seat (2). It holds the (Thermo-Fischer) emitter which is the suppressor-tip combination. It essentially serves as an interface between the off the shelf design of the emitter and the insulators above and below it. During the stacking of the lens, the outer radius of the emitter seat is concentrically aligned with the emitter tip using a microscope and by rotating the assembly until the tip seems to be in the centre. Moving even further up, the inverted L-shape (3) on the inside of the C1 lens is a large custom bolt used to squeeze the assembly below it together. On the outside of the C1 lens it is clamped to the base by a titanium ring (4). The base is a large insulator onto which an invar ring (6) is attached using an interference fit. Permanently attached to this invar is the part (5) which has thread and the interface surfaces to the C1 lens. The threaded discharge ring pushes the C1 lens and the interface on the base together. Finally in the top and centre of the figure the connections for the emitter and electrodes (7) are shown. These supply the current to the tungsten wire for heating but also ensure that every electrode has the proper potential. The thin wires are also shown in grey.

The geometry of the gun lens chamber can be seen in Figure 1.11. Here the anode is shown in relation to the rest of the gun lens. The C1 lens and its inner components are held by the HV insulator to isolate the

Figure 1.11: Coloured technical drawing of the gun lens chamber. The column continues to the right, behind the anode. The openings in the chamber, pointing up and down in this picture, are holes occupied by vacuum pumps.

gun lens from the vacuum chamber. The vacuum chamber has two holes on the sides of the insulator. These are occupied by the vacuum pumps that keep the chamber at a high vacuum. To measure this vacuum a pressure sensor is installed within the chamber (not shown). And finally, around the vacuum chamber there are heating coils (not shown). These are used for a process called bake-out which is relevant to achieve a high vacuum, see section 2.2.

More aspects relevant for a gun lens design are not given here. These will be provided whenever necessary. chapter 2 contains analyses of the current system, where many more interesting considerations arise in the electric, thermodynamic and vacuum regimes.

1.5. Project scope

The EBPG of Raith consists of many individual components which have to work in harmony in order to achieve their goals. In the future, Raith is looking at improvements of their current machine for a next generation column. This thesis will serve to support that goal and research what can be improved on in the gun lens. Therefore the research question that will be answered is:

"What are feasible performance levels for an electron beam lithography gun lens assembly using current analysis and synthesis techniques?"

Raith has several requirements for a next generation design, and the report will show which are feasible and which are not. To support this, the following sub-questions are answered:

"Which aspects are important for the electron beam lithography gun lens assembly, and which should get priority?"

"Which analysis and synthesis techniques are useful for the redesign of the electron beam lithography gun lens assembly?"

The sub-questions are answered in chapter 2.

2

Practical gun lens theory

Before the requirements of the project can be provided additional theory behind the relevant engineering disciplines is provided. This is not typical theory that is given when reading up on a gun lens, but is absolutely necessary when considering the inherent imperfections during the manufacturing process and other practical considerations such as temperature/heat and vacuum. The theory will be given using the current design as an example. Some of the requirements in chapter 3 are based on these initial analyses as an absolute performance is difficult to determine but one relative to the current assembly is feasible. The topics that will be discussed are:

- Thermal effects
- Electrostatic field stability/Gas discharge
- Vacuum science

2.1. Thermal effects

The gun lens has two sources of heat; both the emitter tip at 1800K and the area around the aperture are responsible for heated surfaces. The emitter wires are heated through joule heating by applying a 3.5V potential difference, which initiates 2.3A of current, totalling ≈8W of heating. The aperture is bombarded by electrons. From data of Raith a current of 150μA at 6750V is found, resulting in ≈1W. These values vary over the lifetime of the tip, due to small changes in the tip geometry. By adjustment of the suppressor the slowly increasing 150μA current that exits the emitter can remain limited over its lifetime, learned in a private conversation at Raith. All this heat is dissipated to the surroundings and eventually the environment. To understand the problem, we return to the basics of heat transfer.

Classically there are four main modes of heat transport: conduction, convection, radiation and evaporation. During the operation of the gun lens, convection and evaporation effects are non-existent. Conduction within a material is unchanged, but because of the high vacuum in the chamber, there is very little conduction between two touching surfaces. Surface conduction generally benefits from interstitial gas between the ridges of the two rough surfaces, but this is not possible in vacuum. Even a polished surface will have peaks and troughs, where only the largest peaks touch the opposite material. A very small effective conduction area follows. The size and frequency of the contact points are dependent on material strength, surface finish, clamping force and flatness [48] [7], and can be estimated using some simple equations. An accurate number for surface finish remains difficult, as there are some repeatability problems for high quality surface finishes [16].

The second relevant thermal effect is radiation. Radiative power of a grey surface to its surroundings can be found with equation (2.1) [39], which shows dependency on the surface area A, emissivity ϵ and temperature of the hot and cold surfaces T_h and T_c. The emission is very low at a low temperature difference due to the fourth power dependency on the temperature T^4.

$$Q = A\epsilon\sigma(T_h^4 - T_c^4) \tag{2.1}$$

Figure 2.1: Different materials in the current gun lens. The design is dominated by low magnetic stainless steel, a very common high vacuum material.

The implications of the limited conductivity of the system is analysed in COMSOL [8]. Details on the model are given below. As inputs contact thermal resistances is required which will be expanded on below. At the end the thermal expansion effects are given.

2.1.1. Model input

To determine the contact resistance between two surfaces based on clamp pressure, material strength and others the equations from [48] are used, see (2.2) and (2.3). For σ_B, use the lower value of the two touching materials. The torque on the clamping ring and the ring holding the gun lens module to the large insulator was estimated. For the aperture the clamping is assumed as only the weight of the aperture, since the clamping ring does not seem to provide any additional vertical force. Figure 2.1 shows the different materials inside the gun lens. Table 2.1 provides the data on thermal conductivity k, yield strength σ_B, emissivity ϵ and thermal expansion coefficient γ used for contact resistance and for thermal radiation (Though not relevant here, the thermal heat capacity in the table is C_p). The data was obtained through CES Edupack 2019 (https://grantadesign.com), [14] and [1]. The calculated resistances as a function of surface area $\frac{R}{A}$ are as follows:

1. Extractor on aperture seat (steel-steel): $1.25\frac{K}{Wm}$
2. MACOR®on steel: $0.9\frac{K}{Wm}$
3. Emitter on emitter seat (titanium-steel): $0.24\frac{K}{Wm}$
4. Aperture on aperture seat (molybdenum-steel): $1400\frac{K}{Wm}$

$$R = \frac{3\sigma_B A}{2N k_M} * 10^{-5}[\frac{K}{Wm}] \tag{2.2}$$

$$k_M = \frac{2k_1 k_2}{k_1 + k_2} \tag{2.3}$$

These resistances are only valid for the bare surfaces on metallic contacts (as a note, the ceramic is not metallic, but the result should suffice for an initial analysis, and the magnitude will turn out to not influence the result too much).

2.1.2. Thermal transient and equilibrium

A numerical analysis is performed using collected data. COMSOL includes a heat transport package allowing analysis of complex geometries in transients and steady state. For this analysis, a 2D rotational-symmetric

Material name	$k[W/mK]$	$\sigma_B[MPa]$	ϵ	$\gamma[1/K]$	$C_p[J/kgK]$
Stainless steel 316	15	250	0.075	16.5×10^{-6}	790
Molybdenum	140	850	0.1	5.2×10^{-6}	260
MACOR®	1.5	34.5	0.97	13×10^{-6}	790
Tungsten	165	-	0.04	4.45×10^{-6}	135
Titanium	7	1000	0.2	9×10^{-6}	500

Table 2.1: Table with material data for thermal calculations. The emissivity data was taken from [14]. For MACOR®, it was taken from [1]. Other data is provided by CES Edupack 2019 (https://grantadesign.com)

model is selected. Although some detail is lost, such as the repeating holes to improve vacuum and many of the electrical contacts near the top, the improvement in computation time compared to a 3D model combined with the low relevance of the mentioned aspects is significant enough to warrant this decision.

The wall of the vacuum chamber was given a constant temperature of $300K$, which is also the initial condition for all materials. The connection to the large insulator is not included in the model. Due to the small clamping force, thin connection structures and large thermal insulator the heat transfer through it is negligible.

The model uses a radiation-conduction multi-physics module, allowing it to combine the thermal conduction in and between touching volumes with radiation in the vacuum of space. The heat sources are defined as described before. The viewport of the simulated model can be seen in figure 2.2. Steady state temperatures are reported in table **??**.

Redacted

Figure 2.2: View of COMSOL's viewport of the 2D thermal model. The colour range is capped at 1100K for improved contrast, but the emitter tip is 1800K.

Redacted

Figure 2.3: Simulation of the transient behaviour of the FEG module. There are two blue lines; C1 is the colder temperature compared to the suppressor. Only after 26 hours all parts reach the 0.1K stability window of the machine.

A transient simulation is done for the same model. This simulation shows what happens once the tip starts emitting. The component temperatures as a function of time are displayed in figure 2.3. Over time, the component reach their equilibrium temperature. The vacuum chamber temperature is controlled to within 0.1K. This window of stability is reached at 26 hours according to the simulation. This is comparable to the time to stability found in practice (24 hours as provided by staff at Raith B.V.).

The sensitivity of the results to the heat flow boundary conditions was done, as some variation across the different emitters can be expected. The result is visualized in figure 2.4. Variations from the baseline are followed by similar heating across all surfaces, such that temperature difference between surfaces remain the same. Due to different expansion coefficients an error is still expected. At 20% variation, additional error incurred is in the worst case (Using 316 and MACOR expansion coefficients, and $L = 50mm$) an error of roughly $10\mu m$, or 10% of the normal expansion. The heating variation is in reality much smaller and mostly dependent on the heating required for the tungsten filament.

Figure 2.4: Heating variation study. The baseline heating is multiplied with the heating error, as shown on the x-axis. Temperature changes seem similar across all components. C1 Lens is the coldest, Emitter housing the hottest component.

2.1.3. Thermal expansion

The final analysis regarding thermal effects is the translation between heated components and their effects on the tolerances. Due to thermal expansion, these tolerances can shrink, grow or stay somewhat the same depending on the details of the specific contacting surfaces. From figure 2.3 we have seen that the temperature differences between components change over time. The different rates of expansion will result in unpredictable stick slip behaviour. The performance of the optics stack over the heating period therefore becomes unpredictable as well, which explains movement of the probe as observed by the production team. The differential change in length ΔL due to a temperature change ΔT of the two components with their respective expansion coefficients ϵ is found by equation (2.4) which uses the characteristic length at the interface L. The combined tolerance δ_{total} is calculated from the base tolerance δ_0 with equation (2.5). The change in tolerances at steady state temperature is given in table **??**. In most interfaces, the expansion takes a large role over the manufacturing tolerances in determining the placement accuracy. One can easily criticize whether it was very useful to put initial tight tolerances on some of the parts.

$$\Delta L = L(\epsilon_1 \Delta T_1 - \epsilon_2 \Delta T_2) \tag{2.4}$$

$$\delta_{total} = \delta_0 + \frac{\Delta L}{2} \tag{2.5}$$

Some conclusions can be drawn from the analyses shown above. The system clearly suffers from a long thermal settling time to the stability window of about 26 hours. Furthermore these simulations have shown that finding the exact temperatures of the parts to an acceptable accuracy is difficult if not impossible with the result of Figure 2.4. Designs that rely on knowing these temperatures will be difficult to guarantee the required accuracy. It is recommended that a design which either has a low sensitivity to component temperature changes, or can control the temperatures better should be pursued to fall within the requirements. Some solutions that tailor to these conclusions are given below.

2.1.4. Improvements

The problems can be categorized in thermal settling time and predictability of thermal expansion. Note that the latter is not 'predictability of the temperature' on purpose; It is the thermal expansion which is causing the problems, not the temperature. Having a look at settling time, there are several basic formulas that can be

used from heat transport theory to gain insight. One is the Biot number [39], see equation (2.6). It relates the heat transfer to a component to the thermal conductivity inside the body. The Biot number involves the heat transfer coefficient to the object h_c. In the case of the gun lens, two effects are present in terms of external heat transfer: thermal radiation and conductance through contact. The characteristic length L and thermal conductivity k represent the internal conductance. At small Biot numbers ($Bi \leq 0.1$), the components behave like a lumped thermal capacity; Thermal gradients inside the object are negligible compared to the gradient near the surface, and the object can be assumed to have a constant temperature.

A second number often used is the Fourier number [39], see (2.7). It is used for unsteady conduction calculations and indicates how far the system with characteristic length L is from steady conduction or equilibrium. Other parameters are the specific heat capacity C_p, density ρ and thermal conductivity k and time t. In our case higher Fourier numbers are preferred. From the equation one method is obvious, which is just waiting for a long time. Since time not a free parameter, other parts of the equation should be improved for a better Fourier number. Below some methods are summarized.

$$Bi = h_c L/k \tag{2.6}$$

$$Fo = \frac{kt}{C_p \rho L^2} \tag{2.7}$$

- The term $\frac{k}{C_p \rho}$ is also called thermal diffusivity. This is a measure of how good a material is at moving heat from one location to another inside the material. It is only dependent on the material used, and not the geometry. Materials like aluminium generally have a much better thermal diffusivity than stainless steel, for example.

- A smaller characteristic length L results in both a better Biot and Fourier number. The thinner something is, the easier it is to conduct heat from one side to the other and to heat up (due to a lower thermal mass). The design prefers small and thin over big and thick. Specifically the thickness should be reduced in the direction of the thermal gradient, and not perpendicular to it. Doing so will avoid creating a locally increased thermal resistance inside the part.

- A general note is to lower the part count wherever possible to reduce contacts. A solution can be vacuum diffusion bonding [18]. This method, where two materials are fused by pressing them together in a vacuum and at elevated temperatures for a long time, ensures a perfect thermal contact between two parts. It remains to be seen whether the stresses induced at the fusion location can remain limited when an insulator is bonded with a metal part and temperature changes cause different thermal expansion.

- A larger effective contact patch between components improves the h_c. A common material used in the industry is indium foil, known for its great vacuum compliance and soft properties, which allows it to be used as an interstitial material to improve conductance. Other methods to improve the conductance are found by looking at equation (2.2): Pressure on the contact and conductance of the materials. Higher flatness would also result in better contact between the two surfaces, as a thinner foil can be used.

- A second mechanism to improve h_c is through radiation by selecting the reflection/absorption characteristics and by improving the 'view' each surface gets to another. Low reflection coatings are generally used, which improve the emission and absorption. Unfortunately many surfaces inside the gun lens have to remain very smooth and flat (for vacuum and electrostatic field stability), which goes against many of the working principles of these coatings. Some companies claim a UHV complaint coating, but in general it is unclear whether the coating also holds up to strong electrostatic fields.

The thermal expansion of the parts is unavoidable and should be managed to stay within the stability requirements. The expansion due to the heating from the tip, but also due to the variability of the chamber ($0.1K/h$) are sources of errors. Some general methods are summarized in a list:

- Absolute temperature: By improving the conductivity between parts, the temperature differences decrease and thus effective tolerances δ_{total} decrease. Many methods to achieve this were given in the previous list.

- Expansion adjustment: The tolerances can be adjusted to account for the thermal expansion. This should be done with caution, as the temperature is not accurately predictable and so the tolerance can be too tight as a result.
- Thermal centre: the sensitivity of the temperature swing during operation can be reduced by implementing a thermal centre in the design [50]. Parts with a thermal centre remain stationary on the centre when subjected to temperature changes. The centre can be made a point, line or plane depending on the configuration. For example, if a thermal centre line is aligned with the optical axis, radial movement through thermal expansion is suppressed, while movement along the optical axis can be expected.
- Expansion compensation: the thermal expansion effects can be reduced by purposefully introducing materials with a different expansion coefficient. If the expansion of this new material is in the opposite direction compared to the parasitic expansion, compensation of the thermal expansion can be achieved. The applicability of this technique is limited as material options are small inside the gun lens due to requirements regarding the outgassing and field stability.

2.2. Vacuum science inside the bell

As explained in section 1.4 electron optics requires a vacuum. Because of the use of a Schottky emitter a more strict vacuum is required near the tip compared to the rest of the column, at $10^{-6}Pa$. When trying to achieve such a high vacuum several mechanisms inhibit the progress. It can take several weeks before the desired level is reached. In the following subsections the mechanisms are explained and a numerical model is created to analyse local pressures.

2.2.1. FEG and vacuum

There are several reasons why a vacuum is needed in the gun lens chamber:

- The work function of the Schottky emitter-vacuum interface is highly dependent on the vacuum. If the vacuum is contaminated the source brightness reduces [42].
- ion impacts on the tip can damage the tungsten body and disturb the mono-layer of ZrO_2 [4, 42]. These events reduce the lifetime of the tip considerably.
- Particles absorb electrons and disturb the electron beam quality [12].
- Section 2.3 discusses field breakdown due to the contamination of a vacuum between two electrodes.

Unfortunately a vacuum in a chamber has several means of accumulating more gas particles. The typical pressure-time graph of a vacuum chamber can look something like figure 2.5. At the start of the sequence the majority of the particles are evacuated by pushing particles out of the chamber and creating a pressure difference such that the gas is 'sucked' out. Pretty soon in the process, the pressure becomes governed by individual particles de-sorbing from chamber surfaces [52]. The particles consist of water molecules that accumulate on the surfaces thanks to the humid environment of the clean-room (up to 10^{13} molecules/cm^2 [25]), surface contaminants but also materials of which the vapour pressure exceeds the local pressure, which is called outgassing. It is therefore not only important to have a small overall surface area, but also to properly select materials with vapour pressures below your desired final pressure. The desorption phase takes up a significant portion of the overall pumping process [35]. Commonly the chamber is baked to several hundreds of degrees. Desorption rate $\frac{dn_s}{dt}$ scales exponentially with a increasing temperature T [37], see equation (2.8). By baking, the desorption rate is improved.

$$log\frac{dn_s}{dt} \propto -\frac{1}{T} \tag{2.8}$$

When the baking ends, the system is well into the diffusion regime. High vapour pressure particles from deep inside the material are slowly diffusing towards regions with lower concentration i.e. the surface levels. Once at the surface they de-sorb as described previously. When this effect is eventually mostly diminished, the remaining source of gas is through permeation of the vacuum chamber walls. The resulting pressure is a balance between the pumping speed (around 200L/s for the gun lens vacuum chamber) and the rate of particle introduction through permeation and diffusion. The dominating molecule inside the chamber becomes hydrogen, as its small size easily permeates the chamber walls.

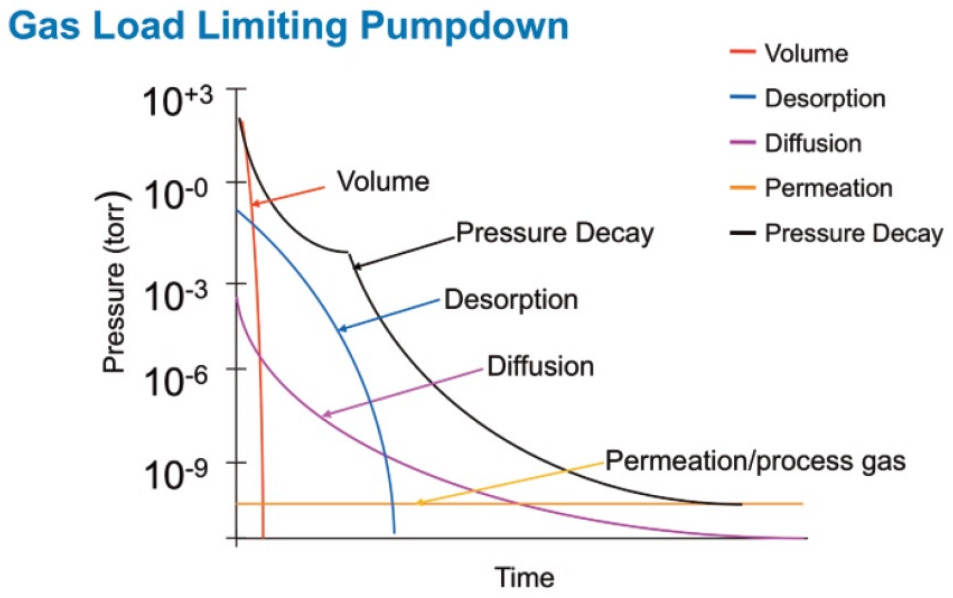

Figure 2.5: Pumpdown process [54]

When looking at the surface area inside the chamber the effective microscopic area greatly determines the magnitude of water adsorption to the surface. The effective area is many orders larger than the geometric surface. Specific surface finishes and coatings can greatly influence the water adsorption and outgassing rate of a surface [37] [45]. A lower roughness generally contributes to reduced water adsorption.

If pressure becomes very low, a transition is made from viscous flow. The Knudsen number is often used to find the state of a flow [34]. The number is calculated with equation (2.9), which uses the mean free path of a particle λ and the characteristic chamber length L. If $Kn > 10$, the system can be considered to be in free-molecular flow. In this regime, the particles are unlikely to interact and will bounce in straight lines from surface to surface if they are unaffected by the electrostatic fields. The geometry of the chamber now has a massive influence on the pressure concentrations inside. Closed off volumes (called virtual leaks) can be a source of particles for a long time and should be avoided. These can be caused by small gaps, clamped surfaces or any other small geometry. Even though the current gun lens takes care of many of these so-called virtual leaks, the design still has quite some possible improvements, indicated in red in Figure 2.6. There are more virtual leaks to be found in the electrical connections up top, which are not indicated.

Simulation of molecular flow is not trivial. The source is from every surface, and their path can not be described in bulk, but only per particle. CERN Molflow (https://molflow.web.cern.ch) uses Monte Carlo simulations to estimate pressure throughout a volume with defined outgassing and pumping. This is used and explained in the next section.

$$Kn = \frac{\lambda}{L} \tag{2.9}$$

2.2.2. 3D Molecular flow analysis

An analysis is done using CERN Molflow. First a quick introduction to the software is given. Then a practical walk through of the build up of the model is provided. This is done such that some familiarity is gained by the reader and perhaps is motivated to use such a program more often.

CERN Molflow concerns itself with solving a Monte Carlo simulation of molecular flow in a vacuum. The flow is created by outgassing and removed through pumping action. Any geometry can be used. The software can build geometry from basic 3D shapes, or you can import an STL-file built in a different CAD program. If the model is complete, surfaces can be given different functions such as outgassing (introduction of particles) or pumping (removal of particles). Polygons can be created or selected to record data such as pressure, particle density, hit rate or numbers of hits. The recording is done through sub-surfaces on the polygon called cells, of which the size can be determined. The polygons can be made translucent, such that particles pass through them. This effectively allows intersection views in any direction that is desired. The pumping and outgassing

Redacted

Figure 2.6: Schematic showing the location of small inclusions where particles have a hard time exiting. These locations were removed for the vacuum simulation.

surfaces can be made simple, by defining a uniform outgassing shape, or more physically accurate such as a cosine or squared cosine law. a sticking factor can be added to the pump to simulate imperfect pumping. The viewport is provided in 2.7. The Monte Carlo simulation is initially very noisy and only becomes smooth after each recorded square has received many hits.

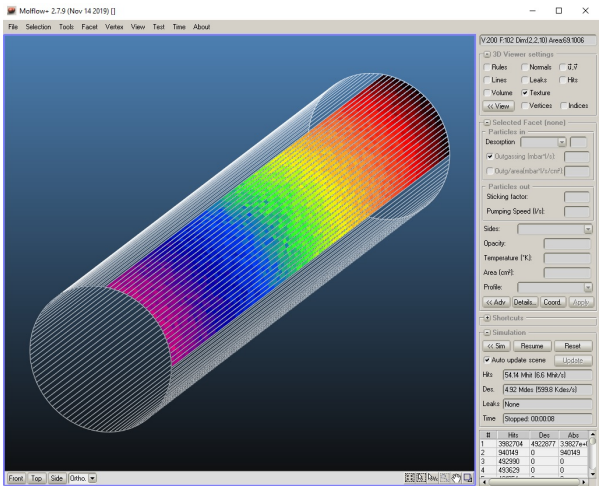

Figure 2.7: Viewport of CERN Molflow with an example tube. A section of the walls has recording enabled so that the results can be visualized. The opening of the tube closest to the viewer has been given some outgassing. The total number of reflections are recorded. Even when almost 5 million particles have been released, the result is still a little noisy. At 100 million particles the results become very smooth.

Creating a working STL file was not trivial in the case of the current gun lens. A rough vacuum chamber

is created as a solid body in a CAD program. With a boolean operation the components can be subtracted from the chamber volume, creating a representation of the vacuum space. However the idealised CAD model will create some small enclosed volumes in the design that should be eliminated before exporting. If this is not done, these volumes have no ability to lose the particles spawned by their surfaces and create locally infinitely large pressures if the simulation is run for long enough. Once this has been done, the geometry can be exported as STL. High geometric detail is not required for accurate results, so a small polygon count is recommended. The electrical connections at the top are also eliminated as they do not add much to the results. The main goal is to find the local vacuum near the emitter tip.

In CERN Molflow, it becomes difficult to select different components as the polygons from touching surfaces overlap. Therefore the estimation was made that all components should have roughly the same outgassing of $10^{-12}\frac{mbarL}{scm^2}$. In reality, the hotter surfaces such as the emitter or the aperture will experience more outgassing. The result is therefore more conservative in terms than the real situation when we look at pressures around the optical axis. The chamber intersection was recorded with a precision of $50\frac{cells}{cm}$. The top ring was assumed to be a pump with $200L/s$ pumping capability. The CPU used for computing was an Intel Core i7-8750H, running at an average 1.7GHz. After 16 hours of run-time, the result was exported. The export is not a picture, but a dataset of the squares that have been hit by at least one particle i.e. the solid regions are not included. The coordinates of these squares are used to form figure 2.8. The results are useful as a relative measure. In other words, the absolute value of the particle density is hard to justify and therefore the results are as a ratio of the chamber vacuum. The particle density inside the bell is often much higher than in the vacuum chamber, up to 27 times. These areas slow down the pumpdown process are a source of contamination. Furthermore, at the tip the vacuum is roughly 8 times worse than vacuum chamber levels. Note that this result excludes mechanical inclusions, which have been removed in the CAD model. Real ratios could therefore reach even higher values.

2.3. Electrostatic field analysis

The gun lens employs strong electrostatic fields (as discussed in section 1.4) to create and control the beam of electrons. Apart from executing this function, the fields are mostly a source of headache. The strength of these fields can only exist in a high vacuum, as the conductivity of air is too high and it would discharge across the air-gap. However, several mechanisms have been found which are activated by the fields themselves that locally increase the pressure. If this is severe enough the consequence is a gas discharge, shutting down the machine. Therefore the fields cannot be made too strong as they tend to annihilate themselves.

The mechanisms by which the pressure increase happens and useful preventive measures are discussed below. The insulators inside the gun lens are also an interesting topic and a separate subsection is dedicated to their behaviour. At the end a numerical model is constructed in COMSOL to demonstrate the ability to analyse the local field.

2.3.1. Gas discharge

When talking about field stability, one term which is used often is the hold-off voltage. This is the maximum potential difference which can exist between two electrodes without a short-circuit/field breakdown. The hold-off voltage is dependent on many factors, but fundamentally it is a function of the material in between the two electrodes. In our case the local insulating properties of the vacuum change drastically with the introduction of particles in the gaps between two electrodes. If the hold-off voltage drops below the required potential difference, breakdown occurs. Several mechanisms exist which introduce particles in the vacuum. A lot of research has gone into HV vacuum insulation [3, 27, 51, 60] but a great source of information bundled together is [33]. They mention two categories of breakdown:

"The main unifying condition to emerge from such studies is that for small gaps (d < 0.5 mm), breakdown tends to be field-dependent, whereas at large gaps (d > 2 mm) it becomes voltage-dependent. In physical terms, the "small-gap" behaviour corresponds to breakdown being initiated by one of the electron emission based mechanisms ..., whilst the "large-gap" behaviour becomes dominated by the [micro-particle] processes..." (p.47).

Electron emission based mechanisms consist of two separate subcategories. Both originate from the idea that micro-protrusions on the cathode act as an electron antenna and start emitting electrons onto the anode. The theory behind it is similar to the physics in a Schottky emitter. First, in cathode initiated breakdown, the joule heating that happens in the tip due to the electrons travelling through it increase the temperature of the electrode significantly and slowly vaporise. Secondly in anode initiated breakdown the bombardment of

Figure 2.8: Particle density ratio across a cross-section of the current gun lens and vacuum chamber. The black areas are solid regions of material. The values are calculated as ratio = particle density pixel/mean particle density chamber

electrons onto the anode can melt the electrode surface. The vaporised material is ionised and start travelling in the vacuum. As a note, a third way of field breakdown is where the emission beam vaporises a particle mid-flight, which is seen as a hybrid between the small- and large-gap breakdown mechanisms.

Micro-particle processes are a summation of the breakdown phenomena caused by micro-particles that are accidentally left on the surface, or de-sorb during operation. If these particles remain on the surface, they can act as an antenna for electron emission. But when they are released from the surface by the electric field, they can accelerate to the other electrode if charged with the right sign. Depending on the impact energy and charge they can bounce, adsorb, damage and/or evaporate on impact. At high energies new particles can be released which can cause their own damage or micro plasmas. The introduction of all these new ionized particles in the vacuum between the electrodes facilitates breakdown. At larger gaps this is dominant compared to emission based breakdown due to the increased voltages, which becomes the limiting factor rather than the local field. For smaller gaps this effect is less noticeable due to the smaller energies the particles can accumulate.

Clearly, the source of problems stems from two things: sharp edges and protrusions on the cathode surface, and particle contamination from the surface or subsurface. subsection 2.3.2 discusses common prevention methods.

2.3.2. Discharge prevention

Measures taken to prevent the events as described in section 2.3.1 are given below. These are again taken from [33].

Micro-protrusions are a major cause of breakdown. During design, edges are rounded to avoid geometrically sharp shapes. During manufacturing, several polishing techniques can be used, such as diamond polishing, electrostatic polishing or other methods [2, 20, 24, 32, 40, 57]. To remove unwanted micro-particles, the component is handled inside a clean-room and cleaned thoroughly before installation with an ultrasonic bath. Furthermore the assembly of the gun lens happens very carefully so as to not create any scratches on the surface.

Then, once installed, several more conditioning steps can be taken such that the full insulating capability is achieved.

- Current conditioning: This method revolves around increasing the applied voltage in steps and letting the leakage current due to the movement of ions and electrons between electrodes stabilise at each step. This method is widely used and is theorized to cause micro-protrusions to become more blunted and remove micro-particles at the cathode. By increasing the voltage in steps the imperfections are allowed to be removed sequentially rather than all at once. If the polarity should be reversed such that the anode is now the cathode the method has to be repeated. In this case micro-particles could become a problem as they are bouncing around between electrodes.

- Glow "discharge" conditioning: This approach uses sputtering of ionised gas at a relatively high pressure with the main goal to remove contaminants from the surfaces. After the treatment the vacuum chamber is re-evacuated to its operational pressure. It typically has considerably better results in terms of hold-off voltage than current conditioning if the right gases are used (Helium and nitrogen are consistently best).

- Vacuum firing: In order to achieve a good vacuum the system is baked, which promotes faster desorption of gas and liquid molecules on the surfaces. This favourably also improves the hold-off voltage as contaminants are energised and removed from the surface.

Other methods are also used frequently but are sensitive to temperature changes above 100K (gas conditioning) or require more complex electrical set-ups (spark conditioning). Therefore these are not suitable for the current column.

There is enough literature which discusses the hold-off voltage as a function of their methods [2, 21]. Fields as high as 10MV/m are conventional, and numbers as high as 20-40MV/m can be reached through careful conditioning of the surfaces and design of the insulator. However, when a gun lens has to be produced many times and a lot of manual labour is used, a small mistake can mean a lot of production delay if the fields are designed on the edge of what is possible. Therefore the fields should be as small as possible, even when all the conditioning steps were to be used.

In the assembly of the current gun lens, it is difficult to prevent small scratches from accumulating near the electrode wires due to how they should be installed. It is desirable to remove these problems in a new design.

2.3.3. Insulator breakdown mechanisms & improvements

The most relevant findings of [33, 38] are summarized:

A typical solid insulator will have a worse hold-off voltage than a vacuum gap of a similar size. This is not due to the bulk of the insulator but thanks to its surface. Various theories exist to explain why this is the case, but they all point to one thing: the cathode triple junction on the insulator. This is the location where the cathode, insulator and vacuum meet. The theories all assume a significant increase in electron emission near this point due to the field emission mechanism. The electrons then travel towards the anode, and many theories branch off what the exact mechanism is which facilitates breakdown. Most involve some sort of release of neutral or ionized particles from the surface, which can cause damage on their own through their impact or electrostatic field. The uncontrolled growth of this avalanche eventually results in breakdown. Clearly, the surface finish and purity of the insulator on the surface is critical.

Combining the causes of breakdown from above a list is constructed with methods to improve the hold-off voltage. Some of these are easy to use, and others require more thought to be put into the design:

- The slow application of DC Voltage on the electrodes has shown to improve the performance. This is largely attributed to the removal of breakdown sites, surface gas, or surface contaminants.

- The angle at which the insulator meets the electrode can significantly improve the behaviour, with sharper angles giving a better performance. Cones with slightly negative angles at the cathode should be avoided. Suitable designs can be made with ceramic balls, although literature on it is limited [36].
- Field reduction at the triple junction can be achieved by recessing the insulator into the electrode.
- Chamfering the cathode end of the insulator is recommended when possible. The idea is that electrons accumulator on the surface of the chamfer and reduce the electric field at the triple junction.
- Increasing the length of the insulator always helps. The hold-off voltage typically follows a relation as $V \propto L^{0.5}$ at large distance (>2mm).
- Adding corrugations in the insulator reduces charge transfer across the surface of the insulator.
- The length of the triple junction should be reduced as much as possible, to reduce the number of potential flashover sites. An insulator with a large diameter performs worse than a small insulator for this reason.
- The material choice is relevant. The homogeneity should be high, and there is an inverse relationship between relative permittivity and its hold-off voltage.
- At the triple junction a small void in the insulator due to a defect can cause a field concentration. An addition of a layer of higher permittivity near the triple junction reduces the local field near the surface. This would also somewhat solve the relationship between relative permittivity and hold-off voltage, as that was thought to be explained by the field concentrations near the base of the insulator.
- surface roughness near the cathode of the insulator appears to be an important factor for hold-off voltage. Interestingly, the roughness of a fired ceramic helps it to improve hold-off voltage. The performance decreases after grinding, and recovers (but not completely) after polishing. Depending on the precision specifications on the ceramic, this could be considered to improve performance.
- removal of potential contaminants through many methods can be used, all of which improve performance. Examples include solvent washing, glow discharge cleaning, chemical etching, vacuum firing.
- Decreasing the temperature of an insulator improves its flashover voltage.
- By sealing the electrode with the insulator through a soft metal such as indium, vacuum gaps near the junction are eliminated [42].

2.3.4. Field strength analysis

Field strength between two flat plates, distance d with a potential difference $|V_1 - V_2|$ can be easily calculated according to (2.10). When geometries become more complex than that, it is quickly beneficial to use some form of numerical simulation. Once again COMSOL is used, this time using the AC/DC package. Compared to the thermal analysis the geometry has to be inverted i.e. the area of interest is now the vacuum instead of the lens elements. A 2D rotational-symmetric model is used to improve computation time. The simulation result is given in 2.9. The field close to the emitter tip is the highest to create the Schottky emission. The second most critical region appears to be the field at the large rounding of the C1 lens.

$$|E| = \frac{|V_1 - V_2|}{d} \tag{2.10}$$

In many locations the surfaces have been rounded to reduce field concentrations. However, it should be clear that improvements can be made. For example, if the outer radius of the C1 lens is increased such as in figure 2.10, the local field concentration is reduced by 25%. This change does not influence much in terms of manufacturability, vacuum or other relevant fields. Further shape optimization has already been performed by [22], which has indicated large improvements in field strength by showing that using complex shapes is beneficial over using simple geometries with fillets.

Figure 2.9: Result of 2D electrostatic field strength simulation. Insulators are left out.

Figure 2.10: Simple improvement suggestion on the radius of the C1 lens.

3

Design requirements and environment conditions

As discussed in section 1.4, the main function for the gun lens is to provide a stable beam with high beam quality. These functions are reflected in the requirements, among others describing weight, cost and compatibility. The first section provides the requirements. Some details or clarifications of these requirements are discussed further. After, environment conditions and mechanical constraints are given.

The gun lens consists of multiple optical components. The unwanted movement of these parts is the most interesting part to a mechanical designer. However, the restriction on these movement are not explicitly stated in the module requirements, but rather should be derived from the requirements and environment conditions. The derivation and results can be found in chapter 4.

3.1. Module requirements

Requirements are given in Table 3.1. Some of them are indicated for a specific current, or have a current upper or lower limit. This is done because both the requirement as well as the sensitivities to imperfections across the current range (5×10^{-11} A to 3.5×10^{-7} A) fluctuate. The magnification of the column is predictable as a function of current. The requirements could be translated to a different point on the current range.

Table 3.1: Module requirements

Requirement name	Value	Remarks
Module exit current	[redacted]	
Probe location stability	[redacted]	Short and long term
Probe size stability	[redacted]	
Probe current stability	[redacted]	
Conjugate blanking line	[redacted]	
Thermal settling time	[redacted]	
Cost of module	Equal or reduced	
Weight	[redacted]	
Vacuum at tip	[redacted]	
Adjustable Optics	Axis symmetric surface changes	Only within gun lens
Forbidden materials	Gold, magnetic materials, non-UHV materials	
Field stability	Relative reduced risk of breakdown	
Achievable chamber pressure	[redacted]	

Stability requirements

Table 3.1 mentions three stability requirements regarding the current, probe size and probe location. All of these variations result in errors in the optical column which propagate down to the probe. Not all of these requirement are as strict for every operation used by the various customers. However, as there are many use

cases and the machine should work correctly for each of these, it creates a 'do-everything' requirement list. Unfortunately there are not many ways around this. The implications of the three stabilities to the gun lens are given discussed below and visualized by Figure 3.1.

- **Probe location:** The gun lens can create a variation in the probe location Δr_i by an off-axis shift of the first crossover Δr_o, see Figure 3.1a) and equation (3.1) [30]. This error propagates down to the probe by multiplying with the magnification M, which varies across the different probe size settings. The requirement becomes more difficult at higher magnification/current, as the allowed error in the object plane is less. After discussion the required stability was only required up to 100nA, slightly easing the requirement. The object location shift is especially sensitive to the position of the C1 lens and aperture seat, see section 4.2 and 4.5.
- **Probe size:** Defocus of the first crossover Δz_o propagates through to the probe as de-focus Δz_i, manifesting in a change in probe size Δd_p, see Figure 3.1b). Using the final aperture angle α_p, the change in probe size can be calculated, see equations (3.2) (3.3) [30]. There are many causes for defocus, see chapter 4.
- **Current stability:** When the system is not emitting the maximum current to the probe, some of it will be blocked by apertures along the way. The aperture inside the gun lens is then not limiting, and as such will not change the current when its position changes (it does influence probe size, in a limited way, see section 4.4). However, something which does influence the probe current is the brightness of the source. If it is reduced, less current will propagate through to the probe for an equivalent probe size. The brightness is determined by the geometry around the emitter, more specifically the extractor position. This is worked out in section 4.3.

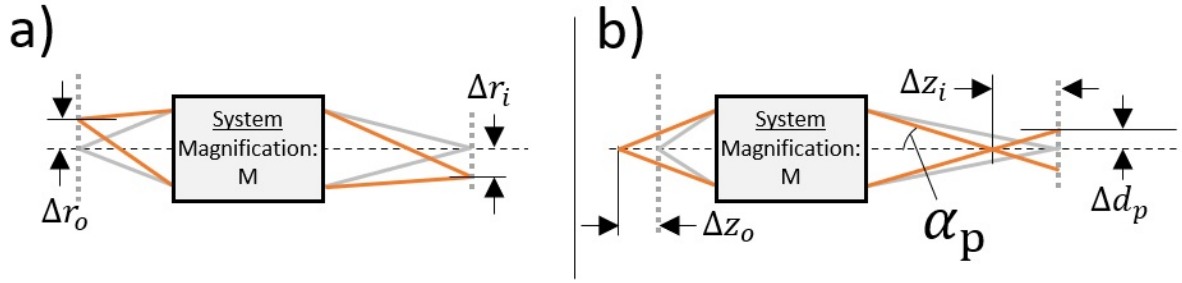

Figure 3.1: a) off-axis deviation of the object Δr_o, resulting in a change in the image plane Δr_i. b) defocus of the object Δz_o resulting in a spot size change Δd_p in the image plane.

$$\Delta r_i = \Delta r_o M \tag{3.1}$$

$$\Delta z_i = -\Delta z_o M^2 \tag{3.2}$$

$$\Delta d_p = \alpha_p \Delta z_i \tag{3.3}$$

Thermal settling time

The gun lens experiences a thermal transient when the tip is turned: from the 1800K tip, and the current blocked by aperture which functions as a joule heating on the surface. From analysis of the current system (given in 2.1) it was found that the heating transient takes up at least 24 hours until the temperature stability is reached. This time detracts from possible production time. As a challenge, the requirement of the heating transient was lowered to improve the start up time. Lower than 6 hours is not useful, as the emitter tip experiences start-up transients which cannot be avoided.

Conjugate blanking error

The beam blanker should have the conjugate object plane in its centre at all times. If it fails to do so, the object at the blanker from the perspective of the probe will deviate from the optical axis [61]. As the voltage from the beam blanker is ramped up, the probe location as a result from the moving object makes a line across the surface of the wafer. The maximum length of the line has been specified by Raith, and is verified at 1nA. At

every current above 1nA, the requirements should also be satisfied. As a note, this requirement is obviously an upper limit. It was explicitly mentioned for this requirement by Raith that further reduction of the beam blank line is desired.

Vacuum at tip

The pressure at the tip is relevant for several mechanisms as discussed in chapter 1 and subsection 2.3.1: the rate of plane collapse and impacts from oxygen, hydrogen and other hydrocarbons in the contaminated vacuum have a large impact on the degradation of the emitter. To limit these effects as much as possible the pressure at the tip should be very low. The vacuum chamber pressure is measured and is regulated to stay below 1×10^{-9} mbar. However, pressure at the tip can be much higher (up to 10 times) higher due to a combination of ultra high vacuum effects, see section 2.2. Therefore a special requirement is set at the tip such that long time performance can be guaranteed.

Adjustable optics

One of the subjects outside the scope of this thesis is the optical geometry. The system could perhaps be improved by making changes. However, this is not the point of the thesis, which focuses around the practical requirements based on a specific optical design. To allow for these changes to happen in the future on the new design, the geometry should be such that this is relatively easy to implement. The exact implications of this is hard to quantify, but it can be verified in a new design whether changes can be made without changing other mechanical geometry which are not related to the optical path of the beam.

3.2. Environment conditions

The machine can be considered to exist in two environments: the transport environment, and the operation environment. They consist of very different conditions, which both have to be endured. They can be found in Table 3.2 and Table 3.3. Transportation of the module only happens when it is installed in the EBPG column.

Table 3.2: Transport environment conditions

Condition	Value	Remarks
Shock load	$\leq 30g$	
Temperature	253K to 323K	
Vibration loads	Various	dependent on surroundings

Table 3.3: Cleanroom & Operation environment conditions

Condition	Value	Remarks
Temperature cleanroom	[redacted]	Preferred temperature
Temperature gradient chamber	[redacted]	
Relative humidity	[redacted]	Only when machine is opened
Acoustic noise	[redacted]	
Magnetic field deviation (DC)	[redacted]	[redacted] over 2 hours
Magnetic stray-field	[redacted]	Peak-peak for both vertical and horizontal plane
Ground vibrations	[redacted]	for all frequencies
Pressure	[redacted]	
Turbo pumps	[redacted]	
Chamber temperature	[redacted]	Ambient to baking, not for operation
Pumping volume speed	[redacted]	

3.3. Mechanical constraints

Some constraints are given by the current iteration of the machine, such as surrounding mechanical devices and the chosen optical geometry, summarized in table Table 3.4. For this project the mechanical constraints are kept relatively open, as it is the goal of this thesis to look at feasible performance levels in general and not only in the EBPG column of Raith.

Table 3.4: Mechanical Constraints

Constraint	Value	Remarks
Lens geometry	Identical	Only optically active surfaces have to be considered
Build volume	A cylinder of ⌀164 x 124 mm	Everything below the high voltage insulator
Electrode connections	Inside the high voltage insulator	

These requirements are the driver for the concepts and eventually the design. To know whether a viable mechanical design can be made it should become clear what the required tolerances and stabilities are for the system. As they are completely missing (only optical requirements are given), they have to be procured by the designer. This is done in chapter 4 using ray-tracing of the current gun lens and looking at the effect of perturbations.

4

Error sources

The gun lens is not simply a perfect object. Manufacturing errors are always introduced in the dimensions of the parts. Vibrations shake parts around, and temperature variations change the size of parts. These imperfections have to be limited to be able to reach the requirements from the previous chapter. The translation between optical to mechanical requirements is performed here. At the end, every optical element in the gun lens has defined limits: both in initial alignment as well as short and long term drift. The results are summarized in table **??**. Effects due to electrode potential uncertainties are not considered.

For each optical components in the gun lens (Extractor, Aperture, Aperture seat, C1 lens) the movement along the principle directions (X,Y,Z,Rx,Ry,Rz) is considered with respect to the tip and the allowed effects are quantified if deemed significant. The movement of the gun lens as a whole is also included. Before starting some simplifications can already be used. As this is a simple rotationally symmetric system, all parts are independent of rotation around the optical axis Rz. Other effects due to rotations (Rx, Ry) are small and thus ignored. The radial directions X and Y are equivalent and grouped as X|Y. Movement is separated into alignment and drift. Alignment is the initial placement tolerance, and drift the movement of parts during operation. At the end of the chapter the roundness of components is discussed which is a special requirement to consider the effects of astigmatism, along with geometry stability.

Looking at the module requirements, the following have an effect on the gun lens design. In other words, if some mechanical part of the gun lens is off of spec, the requirements mentioned here may not be met:

1 Current stability: [redacted]

2 Conjugate blanking error @ Probe:[redacted]

3 Probe size stability: [redacted]

4 Probe location stability: [redacted]

Short term stability is in general dominated by dynamics, while long term stability can be attributed to heating effects. These are given as follows from the operation conditions:

- Temperature variation: [redacted]
- Dynamic frequencies: turbo pumps generate vibrations between [redacted]

To quantify the optical effects from mechanical deviations, ray-tracing has to be performed with the specific geometry variation. The ray-tracing is performed using SIMion [47]. Different information is extracted from the ray-traces dependent on what kind of error we are after. However, they are always compared with a base level, which is the lens in the 'perfect' state. A method to compute information in the reference is given in the following section. Afterwards different components are analysed. Details on how to run SIMion to perform these simulations is given in Appendix A.

As the simulations provide results for the first crossover, and the requirements are related to the probe, a translation has to be done to relate the two. The choice has been made to compare everything in the first crossover. Requirement that stem from the probe are back-propagated through the column with the magnification as in Figure 3.1 to find their corresponding values for that crossover. The magnification is found by using data such as provided in Figure 1.6.

4.1. Perfect gun lens

Here the algebra required to find relevant beam data from SIMion ray-tracing is provided. It should be noted at this point that SIMion is a finite difference program. This inherently limits the ability to improve precision. SIMion allows for both 2D and 3D modelling. The latter is useful when axis-symmetry is broken. From moving to a 3D model, it was found that the model behaved differently and non-symmetrical compared to an identical 2D model. However, it is accurate enough for a first analysis of the system.

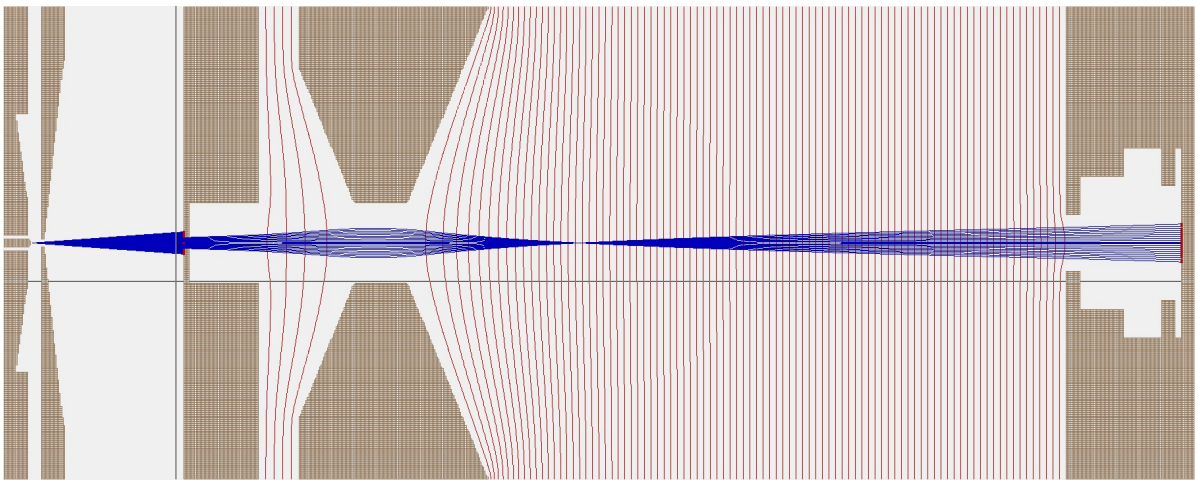

Figure 4.1: Display screen in SIMion of the geometry used by the gun lens. It is stretched vertically to better show the beam shape. The red lines indicate the equipotential lines of the acceleration lens with constant potential spacing. The field at the extractor is not present, as the simulation performs better without it. The electron emission is not simulated and a point source is assumed at the tip with electron energies equal to the exiting speed from the extractor.

An image of the SIMion interface is given in Figure 4.1. From the aperture up to the anode and even inside it a field is present to manipulate the electrons. The rays exit the anode at the right side and 'splat' against a wall, ending the simulation. Information about the direction and velocity of the rays is obtained at the creation and splat of the ray. The crossover location of the ray with the optical axis is computed from the splat ray, and cannot be logged mid-flight. After the ray crosses the axis, it has not exited the acceleration lens yet (which lasts up to the anode as seen by the field lines) and is further deflected afterwards. This deflection creates a virtual crossover location, which is the one we are actually interested in, as that is the one seen by the remainder of the column. So, the ray properties (position $\vec{s}_e$ and velocity $\vec{v}_e$) are logged at the recording wall, which is in a field free region. In the following steps, the virtual crossover is found. Even though the lens is quite thick, the thin lens approximation is used to estimate beam parameters. As a visual support Figure 4.2 is included.

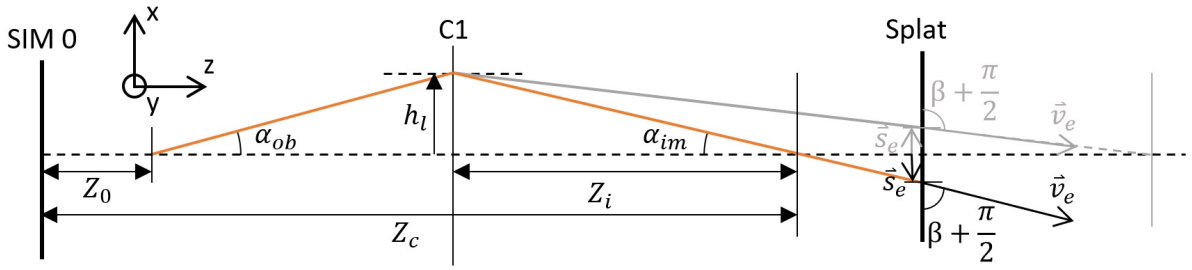

Figure 4.2: Schematic showing the definitions of the variables used in section 4.1. Hollow arrows indicate vectors.

Using the velocity vector of the exiting ray $\vec{v}_e$, the angle between it and the axis α_{im} can be found by equation (4.1). An equivalent equation is needed for the starting angle α_{ob} of the ray. As a note, the standard axis orientation for EO is to put z along the optical axis, which will be used throughout the thesis. SIMion uses

x as the optical axis.

$$\alpha_{im} = arccos(\begin{bmatrix}0\\0\\1\end{bmatrix} \cdot \frac{\vec{v}_e}{\|\vec{v}_e\|}) \tag{4.1}$$

This equation will always give a positive angle. Unfortunately the exit ray can arrive on the recording plane while heading to ór leaving the optical axis, both requiring a different sign for future calculations. The proper value called β can be found using equation (4.2). $\vec{s}_{e,z=0}$ Is $\vec{s}_e$ with the Z component set to 0. The norm of this vector is the distance from the optical axis.

$$\beta = arccos(\frac{\vec{s}_{e,z=0}}{\|\vec{s}_{e,z=0}\|} \cdot \frac{\vec{v}_e}{\|\vec{v}_e\|}) - \frac{\pi}{2} \tag{4.2}$$

The crossover location along the axis z_c can be found using equation (4.3), where $s_{e,z}$ is the z-component of $\vec{s}_e$.

$$z_c = s_{e,z} + \frac{\|\vec{s}_{e,z=0}\|}{tan(\beta)} \tag{4.3}$$

When the distance from the tip to the simulation coordinate origin z_o is found, it can be used to determine the height of the ray at the lens h_l, see equation (4.4).

$$h_l = (z_c - z_0)\frac{tan(\alpha_{ob})}{1 + \frac{tan(\alpha_{ob})}{tan(\alpha_{im})}} \tag{4.4}$$

Finally, the image distance z_i is determined by subtracting the crossover location by the lens location in equation (4.5).

$$z_i = (z_c - z_0) - \frac{h_l}{tan(\alpha_{ob})} \tag{4.5}$$

The data from this simulation is used as a reference point for the simulations below. These all calculate the position of the first crossover and compare it to the reference to find the sensitivities of the perturbations.

4.2. C1 lens

Alignment

Z: Alignment with respect to the emitter causes a de-focus effect. This can be corrected for during calibration, and thus a tolerance on this distance is not necessary. The part should not get close to other electrostatic surfaces though to avoid an increase in the fields in between them. Therefore a simple $100\mu m$ tolerance is applied.

X|Y: The radial shift of the lens deflects the beam with it. The radial shift of the crossover translates to a probe shift at the bottom. The beam alignment coils can correct this effect such that the probe is aligned to the optical axis. However, the crossover will also move along the optical axis, but only in the shifted direction. This cannot be corrected in the current column. The misalignment of the image in two directions is called astigmatism, and is visualized in 4.3. This aberration causes problems at the beam blanker. As mentioned before, the beam blanker requires the conjugate image to be in an exact location. This is not possible if the images in x and y are misaligned.

A second source of astigmatism in the gun lens is the roundness of the lenses. Small local radius changes causes differential focusing and adds to the astigmatism caused by the alignment. The sum of these effects should stay low enough such that the beam blank line remains below the requirement. The allowed astigmatism is discussed first, followed by the lens shift and the roundness. For simplification the astigmatism of the C2 lens is ignored.

To calculate the allowed astigmatism at the C1 crossover, we have to start at the beam blanker. The beam blanker can simply be considered as two parallel plates holding a potential difference, where the intermediate image plane is designed to lie in the middle of the plates. By using theory from [61] the probe displacement (which they call x_{SDi}, but can also be called beam motion error) as a function of the image plane displacement Δf_b can be found (4.6). The equation uses the length of the plate L_b, distance between plates d_b, beam potential V_{SYS}, magnification of the C3 lens M_{C3}, mass of an electron m_0, charge of an electron e and the applied potential difference between the plate $V(t)$. The equation assumes a changing potential, and therefore the entrance time t_{en} and the time of flight through the blanker t_f are included.

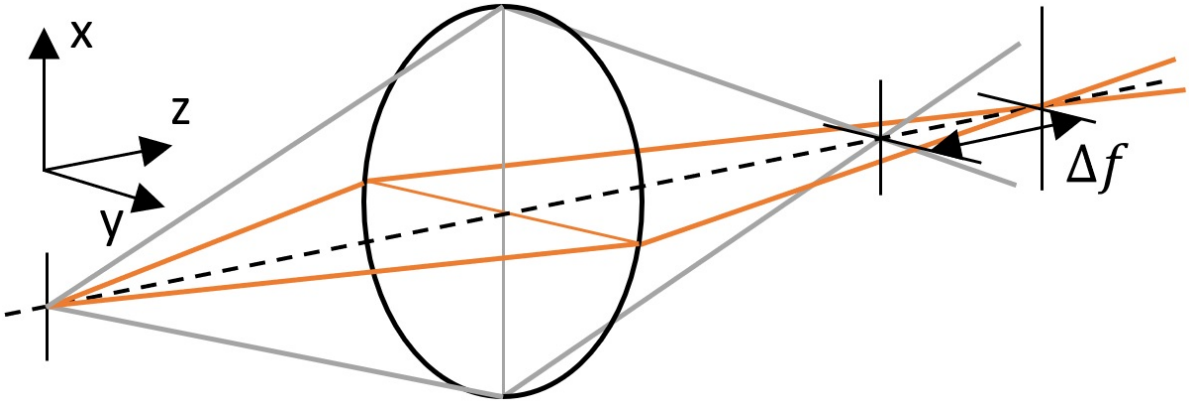

Figure 4.3: Visualization of rays propagating through a lens with astigmatism. The rays travelling through different planes get shifted from each other with a distance Δf.

$$x_{SDi} = \frac{(0.5L_b - \Delta f_b)\sqrt{e}M_{C3}}{d_b\sqrt{2V_{SYS}m_0}} \int_{t_{en}}^{t_{en}+t_f} V(t)dt - \frac{eM_{C3}}{m_0 d_b} \int_{t_{en}}^{t_{en}+t_f} \int_{t_{en}}^{t} V(t)dtdt \tag{4.6}$$

From bending the beam, the perceived crossover location from the perspective of the C3 lens shifts if the intermediate image is not exactly in the middle of the plates, see Figure 4.4. By removing the time dependent component of the beam blanker (as it is not relevant for this application) $V(t) = V_b$ and $t_{en} = 0$, a simple equation is found (4.8) for the allowed vertical image plane shift as a function of the beam blanker probe shift requirement, using (4.7).

$$t_f = L_b\sqrt{\frac{m_0}{2eV_{SYS}}} \tag{4.7}$$

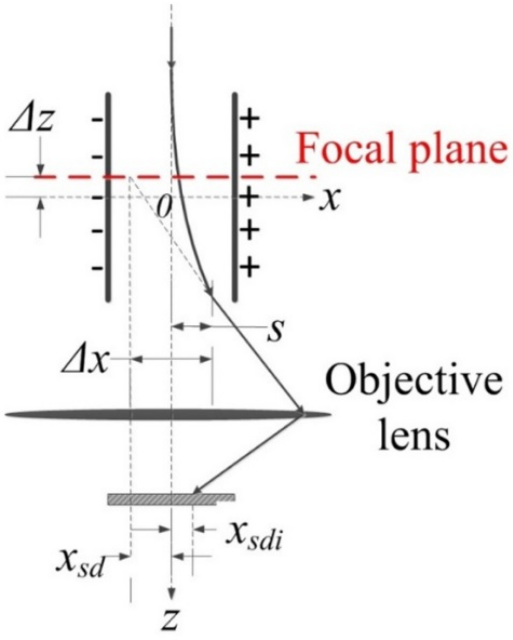

Figure 4.4: [61] Schematic showing the origin of the beam blank error and the parameters for calculating the magnitude.

$$\Delta f_b = \frac{2x_{SDi}d_bV_{SYS}}{V_bL_bM_{C3}} \tag{4.8}$$

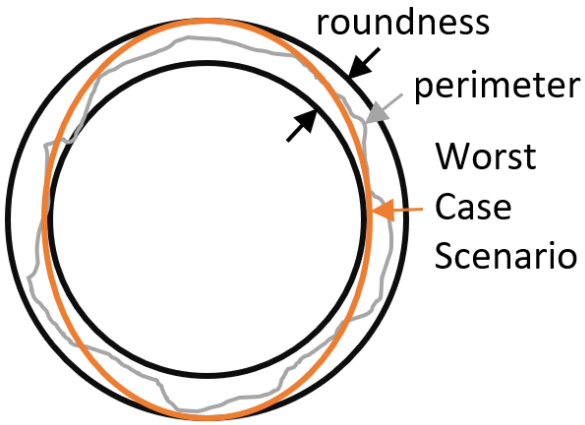

Figure 4.5: Schematic representation of real holes after manufacturing. The roundness is found by fitting the real perimeter inside two concentric circles with a difference in radius d. The worst case scenario is the orange line; If the hole is an oval such that both the inner radius and outer radius are touched 90 degrees from each other, the partial defocus will be the largest.

The current parameters for the beam blanker and the requirement are: [redacted]. As a result, the allowed Δf_b at the blanker is 0.6mm. This should still be translated to the C1 crossover requirement Δf_{C1}, using the magnification of the C2 lens M_{C2}. As the Δf_b is describing two points along the optical axis, the tolerance at the C1 crossover is found by (4.9). The result is displayed in Figure 4.6c) as the green line, and is the upper limit for this requirement. Note that the requirement becomes more strict towards higher currents due to the variability of the C2 lens magnification.

$$\Delta f_{C1} = \Delta f_b \frac{1}{M_{C2}^2} \tag{4.9}$$

Next the actual astigmatism due to alignment is found. A shifted model is created in SIMion. Previous astigmatism due to lens shift has been investigated by [6], which used a parallel beam as input. Equation (4.10) is used to find the astigmatism due to lens shift Δf_{C1s} and is a modified version when ray-tracing is done from a point source. Almost everything in this equation can be determined using the baseline from the previous section. The characteristics taken from the shifted model have an additional subscript s. h_{is}, the off-axis shift can be determined by using (4.11), where the shifted rays are back-propagated to the original crossover location in z, such that the crossover shift in x and y can be found.

$$\Delta f_{C1s} = \frac{h_l}{z_i} h_{is} \tag{4.10}$$

$$h_{is} = \|\vec{s}_{es,z=0}\| + (s_{es,z} - z_c) tan(\beta_s) \tag{4.11}$$

The results are shown in Figure 4.6 b). The model perturbation is linearly increased with a resolution of [redacted]. Deviations above [redacted] are unfeasible, as the beam at that point will not reach the C2 aperture. Shown in Figure 4.6 is the [redacted] line. It shows that even with a large displacement (current system has about [redacted] displacement, see section 2.1) the astigmatism stays within limits.

To finalise the analysis the roundness induced astigmatism is calculated. A typical measure of roundness in mechanical engineering is the difference in radius of two concentric circles in between which the real hole perimeter can be found, see figure 4.5. Finite roundness causes the lens to focus stronger or weaker in one direction than another. To calculate a worst case scenario, the magnitude of this partial defocus (= astigmatism!) can be determined by simulating both the outer and inner radius of the roundness specification and finding the distance between the two image planes Δf_{C1r} as in equation (4.12). Results from the roundness simulations have an additional subscript r. The results of [redacted] roundness on the C1 lens is shown in Figure 4.6c).

$$\Delta f_{C1r} = |z_c - z_{cr}| \tag{4.12}$$

Even when a large lens shift is present such as[redacted], the astigmatism caused by the roundness specification dominates overall. Therefore, when astigmatism should be made 'as good as possible' to minimize the

beam blanking error, it makes more sense to put effort into increasing roundness of the C1 hole rather than improving on placement accuracy. Of course, this statement has its limits once the roundness effects diminish. This balance should be managed carefully during the design, such that the time spent in manufacturing goes towards creating the lowest overall astigmatism effect. From conversations with the column manufacturer it has become clear that the highest roundness they can achieve with their equipment is [redacted]. The consequence is an increase in cost, estimated as roughly 3x for the hole. There is a chance that the hole roundness tolerance is loosened in the future because of this. For now the assumption is made that this is not the case. Following this, improvement of the X|Y alignment to up to [redacted] is found to be useful. Further improvements will not improve the astigmatism of the system as it will be limited by the 0.001 roundness. The X|Y alignment effect is 10x less than roundness astigmatism using the numbers mentioned.

Drift

Z: drift will result in a defocus of the first crossover. The probe size stability Δd_p] is [redacted] at 1nA and below. The probe size stability can be translated to a defocus stability by using the aperture angle α_p and imaging to the first crossover $\Delta z_{c,spec}$ with both the magnification of C3 (M_{C3}) and C2 (M_{C2}) using the schematic of Figure 3.1b) and equation (4.13).

$$\Delta z_{c,spec} = \frac{\Delta d_p}{\alpha_p} M_{probe->C1} = \frac{0.1}{2\frac{0.00015}{0.04}} \frac{1}{M_{C3}^2 M_{C2}^2} [nm] \tag{4.13}$$

To find the relation between lens shift and defocus, a new 2D model is used. Again the perturbations are linearly ramped, with 0.1mm increments between -0.2mm and +0.2mm. The approach taken here was different. The requirement was interpolated for each current setting between the different perturbation lines. The result is Figure 4.7a), with 4.7b) showing the individual simulation results. A local peak is observed near 60pA. This is a result of the image plane crossing going from a negative to a positive deviation as shown in 4.7b), crossing the zero line in the process. The system is insensitive to C1 Z drift at that current. Simulations were done with smaller steps (down to 0.02mm) but the limited accuracy of the program appeared to create too many artefacts in the data to produce reliable results. Therefore this relatively large step size is chosen. At 1nA and below, the requirement for the C1 lens Z drift is $2\mu m/h$.

X|Y: drift for the C1 lens will move the crossover location, and in turn move the probe around. From the simulation done in the alignment section the C1 crossover movement h_i as a function of lens shift was recorded, see Figure 4.8c). 4.8b) shows the drift requirements at the C1 crossover Δx_{C1s}, as calculated with (4.14), which uses the probe location drift requirement Δx_p. With interpolation the allowed C1 lens X|Y drift is found, shown in Figure 4.8a). At high currents the requirements is the most strict. The requirement counts for 100nA and less, so the short and long term drift is [redacted]

$$\Delta x_{C1s} = \Delta x_p \frac{1}{M_{C2} M_{C3}} \tag{4.14}$$

4.3. Extractor

The movement of the extractor mostly influences the current stability, as will be shown below.

Alignment

Z: The source brightness is highly dependent on the geometry and potentials near the tip (source) and thus also the Z position of the extractor. This is a curse and a gift; any small misalignment is deadly, but can be corrected with the electrode potential. Therefore the tolerance on this part can be pretty loose. However, to create an equal field with an extractor that has moved further away from the tip, its potential should be increased. The increase in potential difference can cause problems in field breakdown, see subsection 2.3.1, while a reduction in potential difference does not suffer from these problems. Therefore, when considering this tolerance, it is better to only allow movement *towards* the tip. The standard distance is [redacted]. It was discussed with Raith that a [redacted] tolerance is acceptable. So when shifting that to only include negative perturbations the total requirement becomes [redacted] mm.

X|Y: Alignment of the extractor in X|Y does not influence emission properties significantly, as the hole has a minor effect on the perceived field at the tip. The standard radius of the extractor hole is 0.19mm. The

Redacted

Figure 4.6: Results of simulations for astigmatism. a) displays the variability of the system across different settings. b) Shows the result from the lens shift simulation for several perturbations. c) Shows the astigmatism requirement in C1 with respect to the lens shift and roundness.

effects were verified by using the mirror-symmetric model from SIMion. The artefacts in the data were too large to extract a coherent result, suggesting the effect is very small. Therefore a relatively loose limit of $50\mu m$ is set, which is 25% of the extractor hole radius.

Figure 4.7: Simulation results for defocus as a result of Z C1 lens shift. a) Shows the interpolated requirement of 0.1nm/h probe size change. b) Shows the result of the SIMion simulation. It shows asymmetric behaviour, which is explained with the limited accuracy of SIMion.

Figure 4.8: Results of C1 X|Y Drift analysis. Long term requirement is 12.8nm/h, short term is 4.6nm/s.

Drift

Z: The extractor geometry in Z is strictly defined, as drift causes a significant change in emission properties, which cannot be corrected for during the writing process. This effect can be quantified by using Schottky emission theory. If the assumption is made that the brightness is conserved down to the probe (so no coulomb interactions), the current at the probe is proportional to the current density at the emitter I' according to equation (4.15) [42], which relates it using the radius of the emitter tip r_T and the angular magnification up to the extractor exit M_T. The probe current stability requirement is 0.2%/h.

[42] Provides all the equation below to calculate the tolerance. The Schottky equation (4.16) can be used to relate the macroscopic field to the current density of the source by using the typical physical constants m_0, h, e, k, the emitter temperature T_T, the microscopic field near the tip F and the work function ϕ. If the Schottky emission is too high for the standard equation (the test is equation (4.17)), an additional correction factor for quantum tunnelling effects is added to provide accurate prediction of the new current density J_{es} up to q = 0.7, (4.18). This regime is called extended Schottky emission. The microscopic field is found with (4.19) using the macroscopic field V_e and the field enhancement factor due to the tip geometry β_T. This factor is found with (4.20) using the distance between suppressor and extractor L_SA, the potentials of the suppressor and extractor, V_s and V_e respectively, and the distance between emitter tip and extractor L_{SA}. The angular magnification is found with (4.21). As a note, the equations use cm as their unit of length. Maximum variation in probe current can now be related to the maximum variation of the extractor distance from tip, which can be calculated to be roughly 0.025%/h. With a standard distance of 508μm the allowed variation is 127nm/h.

$$I' = J_s(\frac{r_T}{M_T})^2 \tag{4.15}$$

$$J_s = \frac{4\pi m_0 (kT_T)^2}{h^3} exp(\frac{e^{3/2}F^{1/2} - \phi}{kT_T}) \tag{4.16}$$

$$q = 3.72 \times 10^{-3} \frac{F^{3/4}}{T_T} < 0.15 \tag{4.17}$$

$$J_{es} = J_s \frac{\pi q}{sin(\pi q)} \tag{4.18}$$

$$F = \beta_T V_e \tag{4.19}$$

$$\beta_T = \frac{L_{SA} - (1 - V_s/V_e)(L_{TA} - 0.0068)}{0.366 L_{SA} r_T^{0.758}} [cm^{-1}] \tag{4.20}$$

$$M_T = 0.525(\beta_T r_T)^{0.42} \tag{4.21}$$

X|Y: The system is relatively insensitive for drift in X|Y, as long as it is within an acceptable range as given in the alignment section.

4.4. Aperture

Alignment

Z: The position of the aperture determines the current which can pass. It also defines the start of the acceleration lens. From SIM-ion simulations it can be shown that the optical effects are very small, and the current effects only affect the coulomb interactions down the line. The magnitude of this is very small, and also not very interesting; the current can vary from machine to machine, as long as it is extremely predictable within operation. Each machine receives its own probe vs current graph, and uses that to write with the proper settings (with minimum performance requirements regarding spot sizes and currents that are achievable). Therefore this effect is considered for drift only, where it cannot be corrected.

X|Y: Alignment of the 0.4mm aperture is not critical. When misaligned, the beam will exit towards the C1 lens at a slight angle. As long as the aperture angle at the probe is conserved, aberrations remain within limits, just like the position and current. This is ensured by the settings of the tilt-shift correctors, which align the beam to the optical axis after the anode. However, the excitation of the correctors should remain limited to minimize astigmatism. A decenter tolerance of 50μm ought to be enough.

Drift

Z: This error causes an change in blocked current. Less current means less coulomb interactions up to the C3 lens, increasing the brightness at the probe and vice versa. Unless a very high current is used, this effect is not significant for the probe size and can be neglected. A back of the envelope calculation can be done for high currents. At high currents, the coulomb interactions can contribute to as much as 50% of the probe size (see Appendix A, chapter 5). To give an indication for the sensitivity, a simple estimation is done based on the given probe size d_p stability of < 0.1nm/h or < 0.1%/h for a 100nm probe. The worst case assumption is made that the probe size is dominated by the blur caused by coulomb interactions. The dependency of coulomb interactions on current is dependent on the relevant regime, and will change throughout the column. To again pick the worst case, the most extreme dependency is $d_p \propto I^3$ (see Appendix A, equation 5-22). In other words, the current can vary by $0.1^{1/3} = 0.03\%$/h. At the gun lens, The current that passes is proportional to the solid angle Ω. The beam solid angle is roughly dependent on the distance from tip to aperture d as $\Omega \propto d^{-2}$. Therefore the aperture distance can vary by $0.03^{1/2} = 0.016\%$/h. As the distance is roughly 12mm, a variation of 2.0μ m/h is allowed, which is quite a loose tolerance given only 0.1K of temperature change across the hour.

X|Y: The radial drift only becomes critical at high current; When only a small amount of current is blocked, the C3 aperture imaged to the gun lens aperture is almost the same size. At 350nA (maximum current of the EBPG), current from a circle in the aperture with a radius of 0.188mm is required. At the limit, a 12μm maximum decenter drift over the course of production should cover even this current. This is a very loose limit for drift. To ensure the machine can produce a long time without current problems, several drift periods should be accounted for within reasonable limits. Stability is set to 600nm/h.

4.5. Aperture seat

In many ways the aperture seat is similar to the C1 lens. However, the beam is much less sensitive to its movements, as will be shown below. This is caused by the fact that the C1 lens is responsible for shaping the field that defines the majority of the outgoing beam shape, whereas the aperture seat intends to minimize its

Figure 4.9: Results of astigmatism analysis for the aperture seat

influence. Furthermore, the C1 lens and accelerating field 'straighten out' the beam coming from the aperture seat, reducing any asymmetric effects.

Alignment

X|Y and Z: In the same vein as for the C1 lens, most deviations in X|Y and Z can be corrected by the tilt-shift correctors (up to a limit), but the induced astigmatism thanks to X|Y movement is conserved up to the beam blanker. An identical simulation as for the C1 lens in section 4.2 is performed with the aperture seat and the results are shown in 4.9. Sensitivity is roughly an order of magnitude lower compared with the C1 lens shift 4.6. Because these effects are much smaller, the artefacts of the program start to heavily influence the results. Regardless, it seems as though some information can be extracted from the results. The alignment requirement on X|Y is therefore very loose, at [redacted]

Drift

X|Y: Again, the same procedure is used as for the C1 lens, where the requirement for defocus and X|Y drift is identical. Figure 4.10 shows the results. The X|Y allowed drift is determined at [redacted], and is[redacted]

Z:The simulations of Z drift did not produce much useful to display, presumably due to the precision limit

Redacted

Figure 4.10: X|Y Drift simulation results for the aperture seat. Identical to the analysis performed for C1 in Figure 4.8.

imposed by the program. For an equal shift, the image plane changed at least one order of magnitude less compared with the C1 lens Z shift. The stability is set to [redacted], which is the 10x compared to the C1 lens Z drift.

4.6. Gun lens

Movement of the gun lens within the vacuum chamber misaligns the beam with respect to the anode aperture lens. Although effects are limited, they are explored briefly.

Alignment

X|Y: Even if the gun lens is connected to the insulating ceramic perfectly, the tolerances on the ceramic and other parts up to the anode will cause some misalignment, which amount to [redacted]. However, this misalignment does not cause astigmatism in the beam. The displacement relative to the rest of the column can be corrected for behind the anode. The beam alignment coils introduce only a minor amount of astigmatism, and can be neglected compared to the other astigmatism effects as described with the C1 lens. The alignment of the gun lens should not increase this significantly, such as to not increase the tilt-shift astigmatism effects, which are not calculated in this thesis. The alignment tolerance is set to [redacted].

Z: Movement of the entire gun causes a de-focus compared to nominal. De-focus can be corrected for ahead of production and is thus not relevant. Changes in optical performance are insignificant.

Drift

X|Y: Figure 4.8b) also display what the gun lens stability is, as the drift of the gun lens translates one to one with the observed crossover drift. Therefore the short term and long term drift requirement is 45nm/s and 130nm/h respectively.

Z: Movement of the gun lens with respect to the ceramic will cause a defocus effect. The allowed movement is once again extracted from a SIMion simulation, the results are given in Figure 4.11. The analysis is similar as for the C1 lens; the maximum movement to comply with the requirement below 1nA is [redacted]. Movement from the high voltage insulator and stainless steel vacuum chamber due to temperature changes will contribute to this displacement. at 0.1K, the change in gun lens height is found by subtracting the ceramic expansion from the steel chamber expansion, which is around [redacted], which means [redacted] remains for the gun lens.

4.7. Geometric stability

Finally, a small analysis is done regarding the thermal expansion of the C1 lens. Temperature drift of [redacted] changes the diameter of the C1 hole and consequently causes a de-focus. Using a thermal expansion coefficient of [redacted], the stainless steel diameter changes by [redacted] for the given temperature drift, for which the corresponding defocus is given in Figure 4.12. It also shows that the de-focus specification as a C1 crossover drift requirement. The specification is only violated at currents above 37nA, complying with the requirement. Only when the temperature drift increases to many times the current spec the defocus becomes a problem. The thermal stability of other holes are not considered, as the system has proven to be much less

Figure 4.11: text

Figure 4.12: Results of analysis on the geometric stability of the C1 lens as a results of temperature fluctuations.

sensitive to them (verified by the roundness simulations).

4.8. Final tolerance table

The final results as calculated in this chapter are given in **??**. As mentioned at the start of the chapter the rotation around the optical axis does not influence the optical performance and is therefore not included. From the analyses it has become clear that the alignment tolerance (static positioning) is not as critical, as the system is able to correct for the errors through the use of the tilt-shift correctors and lens strength changes. However, drift cannot be corrected for during operation, and therefore the most strict tolerances are found there, particularly on the X|Y drift for the C1 lens and the gun lens as a whole. Z drift is much less important, except for the extractor. These requirements can now be used as a guideline to steer the concept generation as will be shown in chapter 5.

[redacted]

5

Concept generation & Selection

The requirements of the gun lens redesign indicate several focus areas for the concepts to comply with the requirements:

- Provide high stability of the emitter, extractor, aperture and C1 lens with respect to each other up to [redacted].
- Create an open design which allows much more particles to escape from the emitter tip than the current design. Decrease component temperatures to limit outgassing.
- Reduce the risk of gas discharge caused by electrostatic fields. Practically this means improving surface quality by having a better installation procedure and reducing emission from the triple junction.

redacted

- Keep the design relatively cheap and easy to manufacture which means having a replaceable aperture, extractor and FEG emitter.

Possible improvements on gas discharge, thermal settling time and thermal sensitivity are given in chapter 2 and from these ideas the basic concepts are derived. Designs which comply with the vacuum requirement are difficult to evaluate precisely, and will have to be simulated for a somewhat accurate result.

The concepts are concerned with realising the positioning between lens elements while complying with the other requirements. Some aspects of the design can be mostly separated from this problem such as the connection of the gun lens to the high voltage insulator, or the vacuum holes in the C1 lens. These are discussed in the first section together with material options for the electrodes and insulators. Three concepts are provided afterwards. A choice is made at the end.

5.1. Considerations outside main concept

5.1.1. Material selection

As part of looking into available concepts the materials used are considered. They are relevant to several requirements. First of all, as the vacuum level inside the concept should be very high the outgassing should be minimal. This is mostly determined by the local vapour pressure of the material, but can also vary due to the handling environment before operation and the surface finish. Secondly, the materials should be able to withstand the electrostatic fields. For the electrodes this means being electrically conductive, able to have a very smooth surface and preferably with a low risk of damage caused by handling. The insulators should have very high dielectric strength. The electrical resistivity is important to remain high, such that the current leakage through it is minimal. Finally, thermal properties like thermal expansion coefficient and thermal conductivity are relevant for the flow of heat and stability issues on the long term. In this section, all material data is extracted from the CES Edupack 2019 database (https://grantadesign.com).

Table 5.1 has several materials potentially suitable for the electrode. [33] Provides a good background on what is important: Almost all these materials are quite hard with high numbers on the Vickers Scale. Their resistance to corrosion effects through a strong oxide film is thought to be the largest reason for their success

Material	304L	316L	Ti-6Al-4V	Mb	Pt
Density [kg/m3]	7800-8010	8000	4410-4450	10100-10300	21500
Thermal conductivity [W/mK]	14-16	14.4-15.6	7.1-7.3	129-147	70-72
Thermal exp. coefficient [μm/mK]	16-18	15-18	8.7-9.1	4.8-5.5	9-9.2
Young's modulus [GPa]	191-205	195-205	110-119	315-335	168-172
Yield strength [MPa]	190-310	280-300	786-970	450-795	14-35
Price [GBP/kg]	2.04-2.28	2.76-3.09	15.1-18.1	12.2-19.7	22450
Coarse machining energy [MJ/kg]	0.77-0.85	0.75-0.83	2.53-2.79	0.94-1.04	0.49-0.54

Table 5.1: Material table for the electrodes.

Material	Macor	Al2O3, 99.8	Sapphire/ Ruby	ZrO2 TZP	AlN
Density [kg/m^3]	2490-2540	3840-3920	3940-4020	6000-6130	3210-3280
Thermal conductivity [W/mK]	1.4-1.56	28.5-29.4	40.2-43.5	2.8-3.1	180
Thermal exp. coefficient [μm/mK]	12.7-13.2	7-10	5.3-6.9	9.8-10.2	4.9-5.6
Young's modulus [GPa]	66.9	380	430	200	310
Yield strength [MPa]	94	350	400	1000	300
Price [GBP/kg]	6.8-10.5	24.2-36.5	2360-14200	14.2-20.5	78.7-126
relative permittivity	5.6-6.1	8-10	7.5-11.5	20-22	8.6-9.3
Electrical resistivity [uohm.cm]	1e22-1e24	1e20-1e22	1e22-1e24	1e17-3e18	1e17-1e19
Fracture toughness [MPa root(m)]	1.46-1.6	3.8-4.2	1-1.5	5.5-6.7	2.5-3.1

Table 5.2: Material table for the insulators.

as electrode material choice. Other materials such as copper also create an oxide film, but is semiconducting rather than insulating. The distribution and composition of surface impurities is another indicator for their behaviour as high voltage electrodes. All materials provided here also comply with ultra high vacuum (UHV) requirements such as outgassing and hydrogen content. The presence of hydrogen, oxygen and water inside the system functions as a toxin for the tip, where it displaces the mono-layer (C. Zonnevylle, personal communication, May, 2020). Materials which have a reduced oxygen/hydrogen outgassing content would help in this aspect.

Molybdenum appears to have some good properties: high strength, low expansion coefficient and great thermal conductivity. However, molybdenum has a tendency to collect impurities on its surface. Because of this it is difficult to keep clean while installing. It also a higher manufacturing competence compared to the other materials in the list.

Overall, the two stainless steels come out great. The versions with increased nitrogen content 304LN and 316LN have very similar properties, but have an even better magnetic permeability. This is extremely important, as magnetic fields apply a force on moving electrons and will deteriorate the quality of the beam. Titanium works too, but the base material is costly and more difficult to machine, resulting in expensive parts. Platinum has some good properties but due to it massive price (second only to Rhodium) its use should probably stay limited to small components inside the gun lens.

As a side-note, aluminium is close to being a great material for this application. It has a great thermal conductivity, its expansion coefficient would allow tricks to be used such as expansion compensation, and the UHV properties are good. However, aluminium and aluminium alloys cannot create stable fields the way the previously mentioned materials can, and are therefore rarely used in these applications. Moreover, aluminium alloys often contain zinc which is a no-go for UHV. Its vapour pressure is simply too high.

For the concepts stainless steel 304L (SS304L) is used, as it has great properties and is slightly easier to manipulate in manufacturing than SS316L.

Table 5.2 Shows some interesting insulator materials with their relevant properties. Some properties are taken from ceratec®(ceratec.nl). Macor (developed by Corning (corning.com)) is the material currently used for the gun lens insulators. Other materials considered in the table are well-known electrical insulators. Their electrical resistivities are all very high.They are also considered UHV compliant [10]. Their outgassing rate can still differ by orders of magnitude and with very different outgassing particles [41, 44], so more research should be done to find whether the properties are satisfactory. These properties are also dependent on handling environment and cleaning procedures.

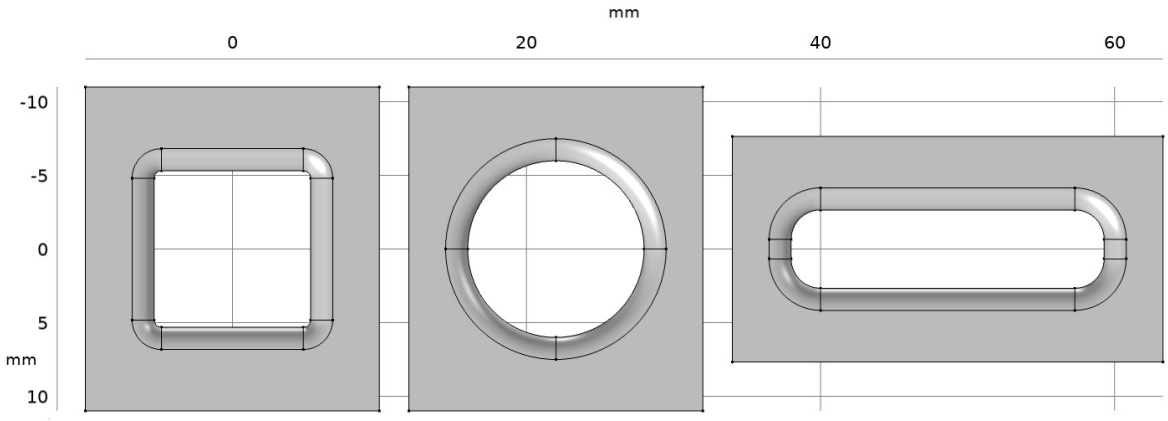

Figure 5.1: The lens holes used for electrostatic field computation. The rectangle has a length to height ratio of 4.

As will be shown in the concepts, in most situations the insulator needs to provide low stiffness in certain directions. The strain an insulator can provide is dependent on its Young's modulus and yield strength, which should be low and high respectively. ZrO_2 TZP provides the highest capabilities here, with a ratio (yield strength in MPa divided by Young's modulus in GPa) of 5. This is five times better than other insulators in the table. This does not tell the entire story however, as the lower thermal conductivity could pose problems. Furthermore, its high relative permittivity could create a worse triple junction with high sensitivity to local imperfections.

Macor is a machinable ceramic, such that easier manufacturing is achieved. However, the material tends to shed small dust particles during handling and inside the current design. This is presumably due to the friction contacts. Except for thermal conductivity, it has great properties; high expansion coefficient (near steel), low relative permittivity and a relatively easy to manipulate.

Another potentially interesting material is Aluminium Nitride. Due to its very high thermal conductivity low temperatures could be expected if used properly. It does have a higher price, so it remains to be seen whether the improvements are worth it.

Material selection will not be made here. It is completely dependent on the concept and what combination of properties turns out to be the best.

5.1.2. C1 Lens vacuum holes

When the concepts consider vacuum performance, they do not take into account the fact that the C1 lens also should allow more particles to fly out into the vacuum chamber. To comply with the vacuum requirement though this area of the gun lens should be considered. The current design has 6 holes spaced equally along the outside of the lens, with a diameter of around 15mm. To find improvements a small study was performed on the lens vacuum holes. To start, the hole geometry determines what field factor can be found near the filleted edges. The field factor β is defined as the ratio between the local maximum field and the macroscopic field, and indicates what amplification of the field can be expected locally. The field factor should remain as low as possible to create a robust design and is the limiting constraint when increasing the hole size/frequency for vacuum sake. Three simple shapes are considered: a circle, a rounded square, and a rounded rectangle with and arbitrary length/width ratio, see Figure 5.1. The cross-section is kept equal, as this determines the orifices' conductance. The field factors are roughly equal between all of them regardless of the rectangle dimension ratio, see Figure 5.2. The exact field factor is quite noisy, due to the high sensitivity to the local geometry and because it is a derivative of the solved variable. When the cross-section is increased, the field factor near the fillets increase.

From these findings, a simple strategy can be built. As the aspect ratio does not seem to matter too much, using long rectangles is the most efficient use of the side of the C1 lens without introducing large field concentrations.

Inspired by [22], a small analysis was done on the specific fillet shape of the holes. Once again, similar but not identical geometry and parameters were used to the design. The round shape is not optimal for reducing the field factor. Figure 5.3 shows improvements as a result of edge shape optimization in 2D. By using a quadratic Bézier shape, the fillet shape can be changed. In the regular case, $\beta = 1.39$. After optimization, the

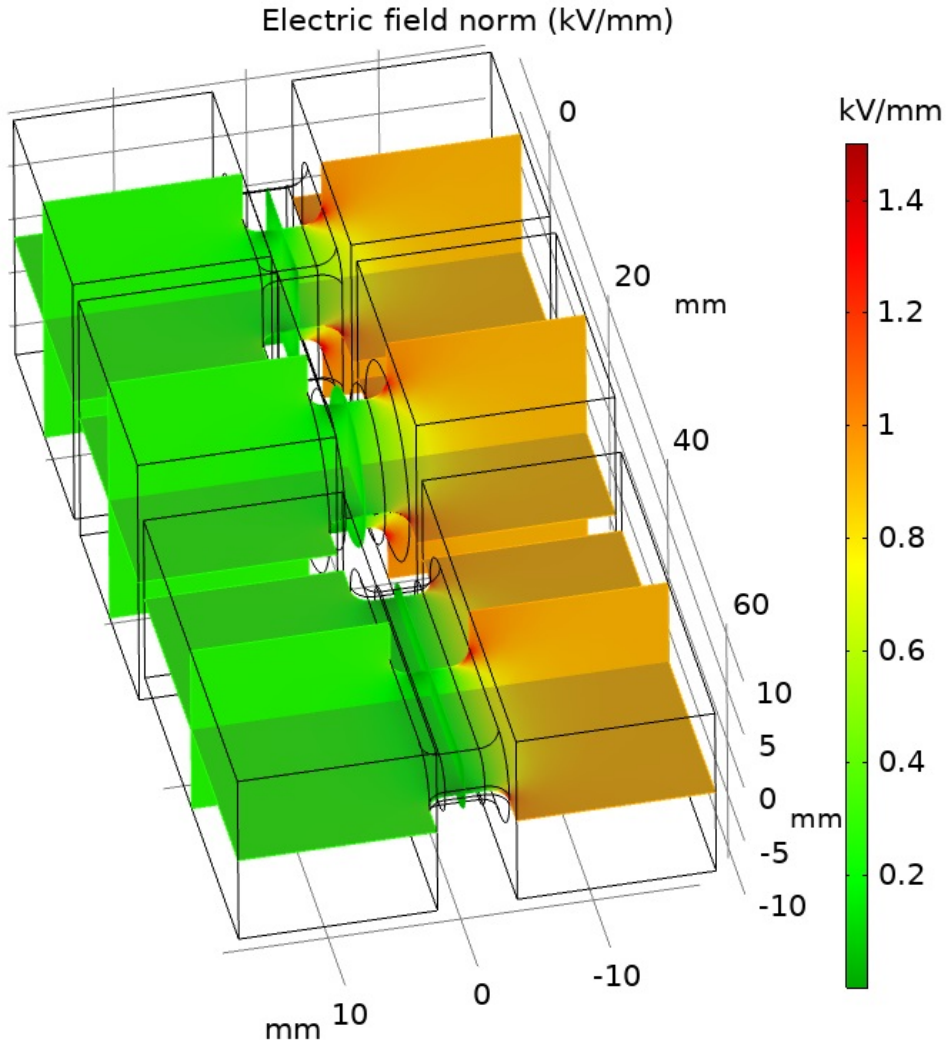

Figure 5.2: A result from the lens hole investigation. The geometry and electrode potentials are an approximation from what can be found in the vacuum chamber. The field concentrations (red regions) can be seen to be roughly similar across all shape types. The rectangle has a smaller field concentration along its short edge.

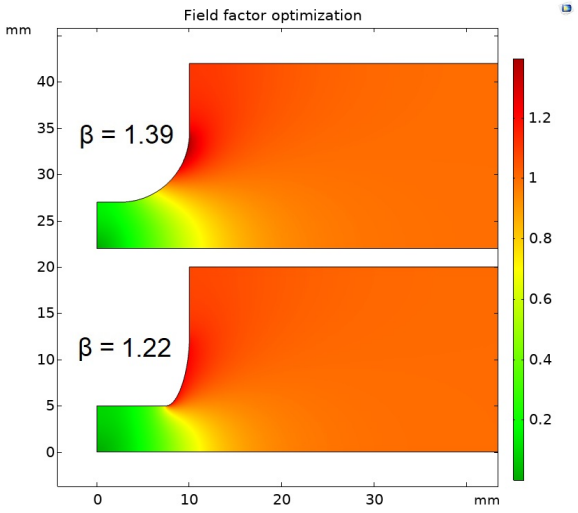

Figure 5.3: Result from fillet shape optimization to reduce the field factor at the edges of the holes. An improvement of 44% is achieved by using simple optimization rules.

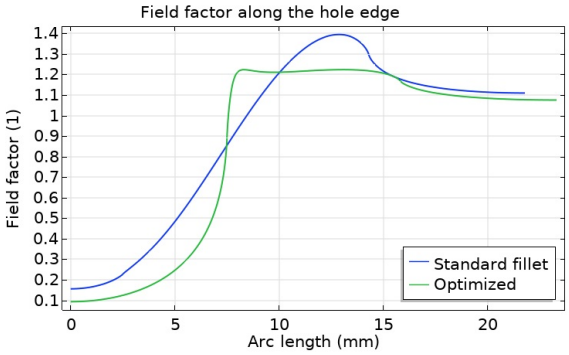

Figure 5.4: By reduction of the field factor the shape optimization has created a flat profile of the field along a large portion of the hole edge. It sharply falls after entering the hole.

new shape gives $\beta = 1.22$, an improvement of 44%. Figure 5.4 shows the field factor along the edge profile.

Practically, this shape is more difficult to manufacture as a complex corner rounding end mill has to be made. The final design of the edge profile should be created in conjunction with the manufacturing team to ensure an optimal design with trade-offs in manufacturing and performance.

An idea for a working design is shown in Figure 5.5. It takes into account most manufacturing limitations: The holes are in a flat surface such that it can be easily milled using a corner rounding end mill. These can be given the aforementioned optimal shape. The bottom remains round, such that the influence on the beam is minimal. The flat surfaces have to meet with the round bottom of the lens. By choosing for a 12 sided regular polygon the transition is only small compared to a lower edge count polygon. The resulting surface defined by three dimensional curves is easier to manufacture than filleted holes on a curved surface would be. The fillets on the inside of the lens at the polygon edge transitions are unnecessary but inevitable due to the milling process. This radius should be tweaked such that an end mill can be found which can reach the necessary depth, about 60mm. The radius in this design is 6mm, which should be enough to reach. Overall the total orifice area is increased by 2.5 times. The field concentrations are most likely better compared to the original design due to the implemented solutions, but this has not been verified. The orifices can be made larger/smaller depending on what is found in a detailed electrostatic field analysis.

5.1.3. Gun lens - HV insulator interfacing

The stability of the connection of the gun lens to the HV insulator has been shown to be quite strict as part of the requirements, see section 4.6. At 130nm/h thermal effects can be substantial enough to cause problems. The current design uses a kovar ring to connect to the C1 lens, see figure Figure 1.10. The connection is shielded with a titanium ring. The ring also presses the two parts together when it is screwed into the kovar thread. This design is unpredictable when significant swings in temperature are expected. At 0.1K/h temperature swing, the expected expansion difference across the diameter is 81nm, which complies with the requirement. However, the thermal settling time of 6 hours will not be reached if all parts should heat to within 0.1K of their equilibrium. Therefore a lower sensitivity to thermal changes is beneficial for reaching this requirement.

The main focus of this chapter is not on the connection between the HV insulator and the gun lens. Still, one feasible solution is illustrated here. It does not require major design changes on the HV insulator, see Figure 5.6. The design uses radial springs milled into the kovar ring (green). It allows radial compliance for large temperature changes [49]. The stability is theoretically perfect, but is limited by material and manufacturing imperfections. However one can expect this system to allow for much larger temperature changes such that the 6 hour stability time can be reached. This is discussed more in depth in the third concept in section 5.2. The lens (grey) has a small steep chamfer to allow easy mounting, and the same titanium ring (light yellow) is used as a gravity compensator. By pressing three hard and UHV compliant balls (blue) into the titanium ring

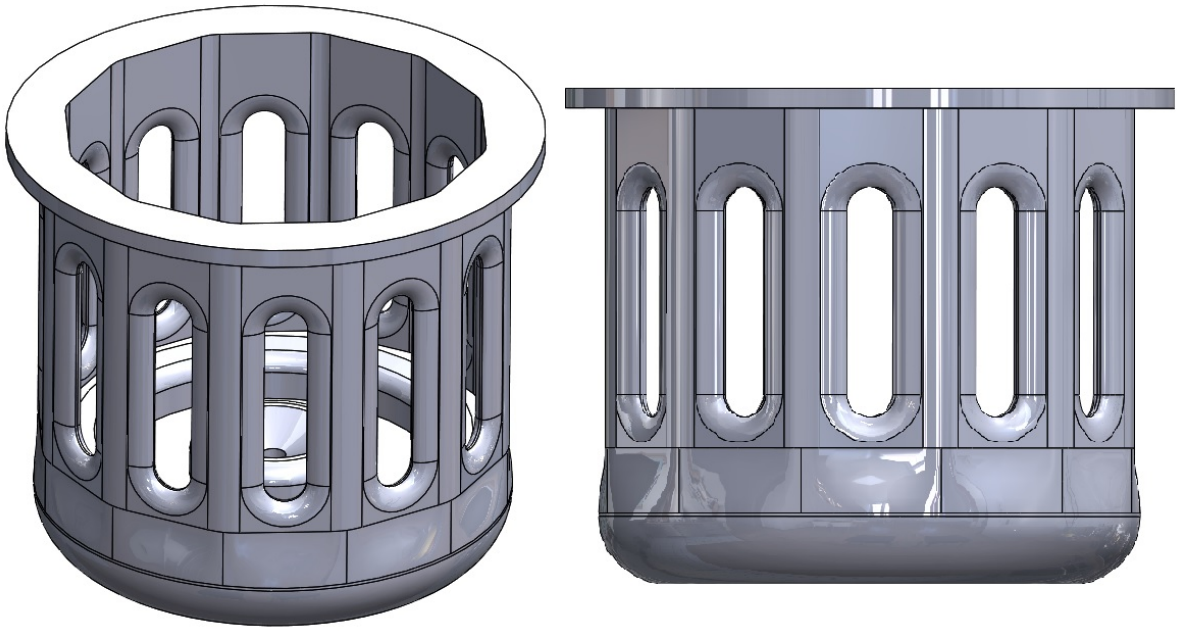

Figure 5.5: A suggestion for the C1 lens vacuum hole design. It uses both the slots and the custom fillet design. There are total of 12 vacuum slots on the side. in between the slots and the bottom is the transitional geometry to connect them smoothly and without creating large field concentrations.

and using those as the contact points, the lens is constrained by three degrees of freedom (z, Rx, Ry)(DoF). The radial springs supply two more (x, y) albeit not as stiff, and the final one (Rz) can be ignored as it does not influence the performance of the system. The ball mounts are pre-stressed by springs (purple) which are engaged when the lens is installed, see Figure 5.7. The sharpness of the edges on the radial and pre-stress springs are not critical, as they are placed in a field-free area and as such gas discharge is not expected. The titanium ring can be screwed up to a limit so that the springs are engaged but cannot be fully flattened by accident.

5.1.4. Extractor geometry

A large limitation on the tip's ability to lose particles is the local geometry. The suppressor and tip are fixed, but the extractor is produced by Raith and can be altered, as further improvement to comply with the vacuum requirement. The field near the tip should not be disturbed by a new geometry, and thus an analysis was done to look at the possibilities. A 2D rotational-symmetric geometry was created in COMSOL. The extractor distance from the suppressor remains the same at the centre, but the geometry now sweeps back the further out it goes. The exact shape is determined by the vacuum requirement: Ideally particles fly straight out from the tip. Because of this a line is drawn from the base of the tip. This line determines the starting position and the angle the extractor takes θ, see Figure 5.8. The line determines the optimal geometry; a similar starting point but with a steeper angle will not accomplish much more, as the particle do not 'see' this additional freedom when flying out anyway. The angle of the line is varied and the variation of the field near the tip is observed. The result is shown in Figure 5.9. The change in field is not very drastic, even at sharp angles. At a 40 degree angle, shown in Figure 5.8, the maximum field is only 1% less than nominal. The 1% loss in field can be retrieved by moving the extractor closer or increasing the extractor potential. The angle can be increased even further, but the design should still be manufacturable and a much larger angle has diminishing returns if the particles start bumping into the aperture seat or C1 lens before exiting the gun lens.

5.1.5. Electrode wire connections

There are several approaches that could be used to route the wires to provide the lenses with their required potential. The current method uses thin wires of 0.5mm to make the HV connections at the HV insulator to the lenses. The method of clamping means the wires cannot be wired directly through to the HV insulator, but require additional interface parts. These interface parts introduce additional surface area from which continuous outgassing can be expected. Furthermore, some of these parts are sharp, reducing the field stability on

Figure 5.6: Execution of radial spring concept. The lens (grey) is stabilised radially with springs (green) and supported vertically with three ball-on-flat contacts around the perimeter (blue). The balls are pressed into the titanium ring (light yellow). This is screwed into the kovar spring component, up to the maximum distance. The springs (purple) provide a pre-stress to the triple ball contacts.

Figure 5.7: side view (watching through the titanium ring) of the spring required for the ball-on-flat connection. The spring (purple) provides a force in between the kovar ring (green) and the lens (grey). As the ball (blue) is rigidly connected to the kovar ring, the lens is pushed onto the ball. This is repeated two more times in equal spacing around the perimeter.

Figure 5.8: The geometry of a swept back extractor. In this figure, the angle θ is 40^o.

Figure 5.9: Maximum field enhancement as a function of the extractor angle. The result should and cannot be used for accurate emission field calculations, but simply gives an indication of the change at the tip due to the macroscopic field.

the top. The method of attachment to the electrode creates risks of surface damage, as the wire and electrode have to be pushed against each other during installations. These problems all clash with the vacuum and field stability requirements as given in chapter 3. Suggestions are given below to improve the wires. These suggestions are also included in the CAD model of the final design to prove their viability, see chapter 6.

The extractor/aperture combination needs it potential supplied by a metal wire, as well as the C1 Lens. The emitter needs three; power through the wire and the suppressor are to be connected. These are already close to the HV insulator, and so work a little differently. One way to simplify the longer wires is improving the stiffness of the wire. If the position can be defined by its mounting point on the lens, the other endpoint is predictable. An example is given in Figure 5.10 where the diameter is increased to 1mm and a flat spot is milled on the wire to provide rotational stiffness. As the bending stiffness scales with the fourth power of the radius, the wire has become $2^4 = 16$ times as stiff. The wire can still move along its axis inside the lens hole if the connection is not tight, but as soon as the connection is made up top this direction is also defined, see Figure 5.11.

The wires from the emitter are simpler as they are already oriented upwards. They only require a connection between the HV insulator and itself. This can be done by using off-the-shelf wire connectors such as the ones shown in figure 5.12. This connector is attached to the HV insulator and connects to the emitter once the gun lens is installed.

Figure 5.10: The wire connected to the C1 lens or extractor/aperture. It is installed with a milled flat spot such that rotational stiffness is provided.

Figure 5.11: An example of a wire connection at the HV insulator. To have better contact between the two parts a inwards deflected slot is included which gives some tension. A catching cone could be included if the alignment of the wire is too inaccurate.

5.1.6. Aperture clamp

At operation, the aperture lies in the space reserved for it in the aperture seat. It does not require vertical clamping to remain in place. Still additional fixation is required to ensure survival during transportation. This fixation does not need to be active; the current design has a passive vertical ring inserted which is not able to provide pre-tension to the aperture but only limits the vertical movement. It also should use as little surface area as possible. The current fixation ring has a surface area of about $980mm^2$, some of which is a clamping surface. These clamping surfaces are minor sources of outgassing and slow down the pumping process. This is an obvious clash with the vacuum requirement and a good reason to look into a simple solution.

The idea that will be used for the concepts utilizes the connection between the extractor and aperture seat as a means to create the movement restriction. First the aperture is placed into the aperture seat. When the

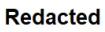

Figure 5.12: [23] An example of off-the-shelf UHV wire connectors. These are made from beryllium copper. It is a great material for conductive UHV applications. However the material is toxic for the operator during manufacturing and is such not considered for the electrodes in the gun lens.

Figure 5.13: Visualization of the aperture movement restriction ideas. On the left an overhanging extractor is used, and on the right a hole and dowel pin is used.

extractor is placed on top, it includes some additional geometry that hangs over the aperture. This geometry ensures that the aperture can not leave its seat unless the extractor moves too. Furthermore, if the gun lens is positioned in the correct orientation (right side up), the aperture always falls into the correct position as the aperture can not create strong enough friction contacts to remain in any angled position. By using this principle the design is greatly simplified. If manufacturing limitations make it difficult to hover material above the aperture, a hole and dowel pin could be used, see Figure 5.13.

5.2. Concepts

The concept generation is mostly concerned with creating the positional stability combined with a satisfactory thermal settling time as obtained through chapter 4. These challenges are the most strict, and seem to define the concept the most compared to the other requirements. The requirements should be met between the three major lens elements: C1 lens, aperture/extractor combination and the emitter. These parts can not touch each other and require an insulator between them. Additionally the system will have to do so while complying with the other requirements as mentioned in Table 3.1.

Radial stability is both dependent on the vibrations in the system (short term) as well as temperature changes (long term). During concept generation it became clear that any stick-slip behaviour would be deadly for the stability and that a thermal centre or expansion compensation would be necessary to provide the thermal insensitivity. The 'Expansion compensation' method mentioned in subsection 2.1.4 would be hard to achieve as the material freedom and space is quite limited. Material options are discussed in subsection 5.1.1. Three different concepts are presented which use the thermal centre concept.

The mechanical stability and 'Thermal settling time' requirements will be judged based on whether the concept complies or not ($\checkmark / x$). The 'Vacuum at tip', 'Field stability' and 'Cost of Module' performance is judged on how well it performs, using an ordinal scale ranging from very poor (- -) to excellent (++). Other requirements from Table 3.1 and **??** which are not mentioned here are 'Adjustable Optics', 'Forbidden materials' and 'Achievable chamber pressure' as well as the mechanical stabilities which are much less strict. Although these requirements are taken into account when creating the concept, they are not covered for each one. The full list of requirements is verified in chapter 6 at the detailing of the final concept.

5.2.1. Concept 1: Ceramic balls

The combination of a ceramic ball and V-groove constrains the ball and body in two DoF. By doing this three times around a central point with 120^o between them, six DoF are constrained. The central point is a-thermal; if the system heats up, we can expect zero movement at that location. In fact, the entire axis coincident with that point and normal to the plane of the v-grooves won't move radially. This idea is used in the first concept as shown in the sketches in Figure 5.14. Both the emitter seat and extractor/aperture have v-grooves installed, in which the ceramic balls can sit. The balls are pressed into the C1 lens by using a cylinder extension. By implementing a small leaf flexure below the ball, the system is allowed to expand without slipping at the v-groove interface [50].

Stability (✓)

In the long term the flexures bend to account for temperature changes. Due to the poor contact high temper-

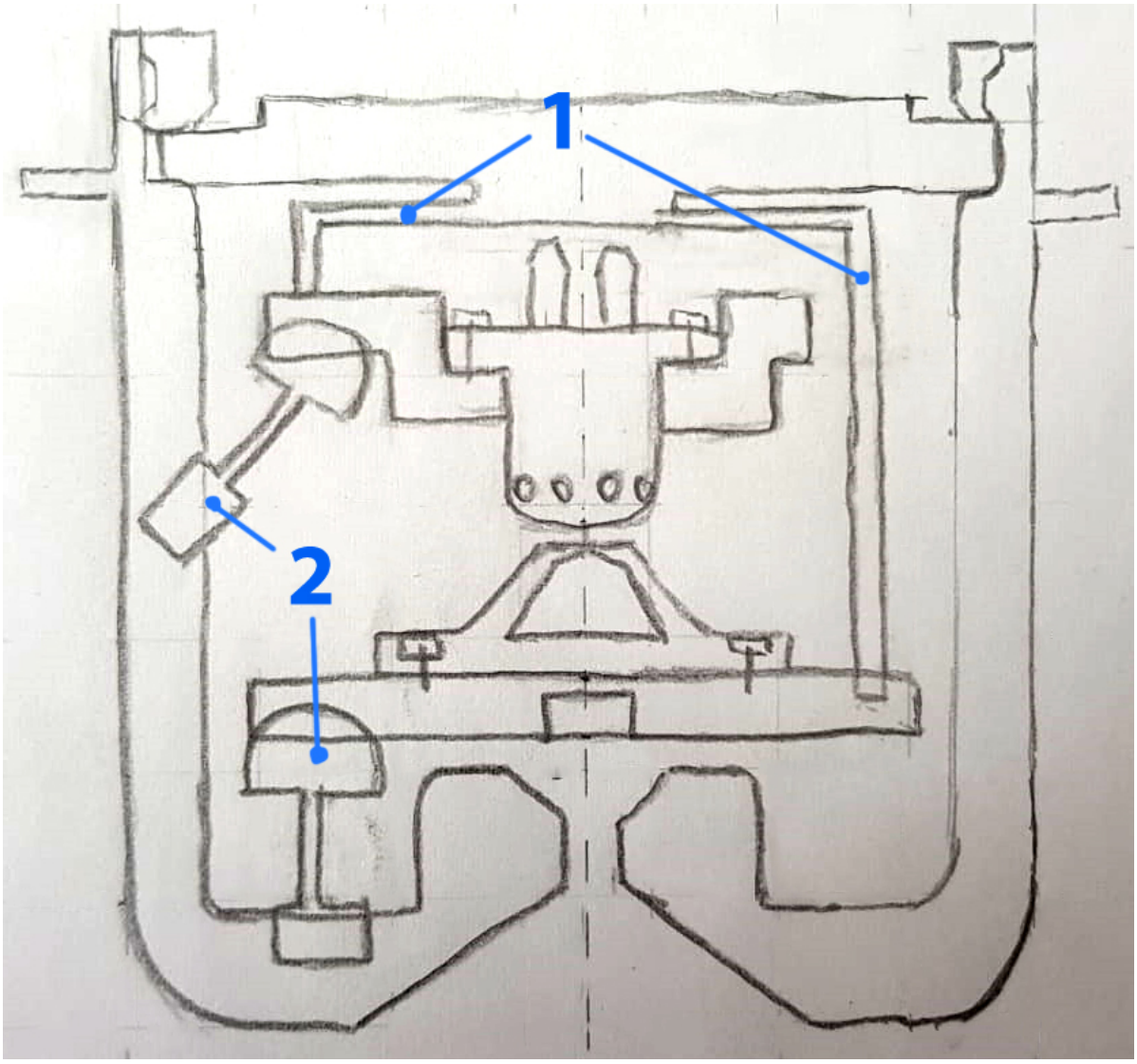

Figure 5.14: Sketched cross-section of the first concept. 1) springs providing a force to hold the lenses in place. 2) Ceramic balls pressed into the C1 lens, and in the v-groove on the other lens elements. There are three per element equally spaced around the perimeter.

ature differences can be expected between lenses in the system. By using the thermal model from the current design and turning off contact conductance, we find that a representative temperature difference between emitter and C1 Lens is below 300^{o}C. Using simple equations for a leaf flexure made from ZrO_2 TZP, it is clear that the thermal expansion (240 μm) can be corrected by a leaf flexure with very normal dimensions: length and width of 10mm and 6mm respectively, and a thickness of 1mm. By optimization the friction forces can be reduced even further such that the pre-stress can also become sufficiently low (pre-stress is responsible for the available friction force in between ball and v-groove. High pre-stress also crushes the local surface at the contact, so it should be balanced). The radial stability of the extractor/aperture is easier to achieve as the temperatures are less extreme. The total axial thermal expansion from the thermal loop (emitter -> emitter seat -> insulator -> C1 Lens -> insulator -> aperture seat -> extractor) is used to find the movement between the tip and extractor. By doing so it is found that the extractor axial stability is easily achieved with a safety factor of about 50.

The short term stability is limited by the flexures implemented in the ceramic to provide the long term stability. The eigenfrequency of the system should be above 1200Hz to avoid resonance in the system. Because of the small size of the flexure, this is easily achieved and verified in a simple COMSOL eigenfrequency analysis which is not shown. The weight of the emitter seat can be optimized to further improve the first mode frequency.

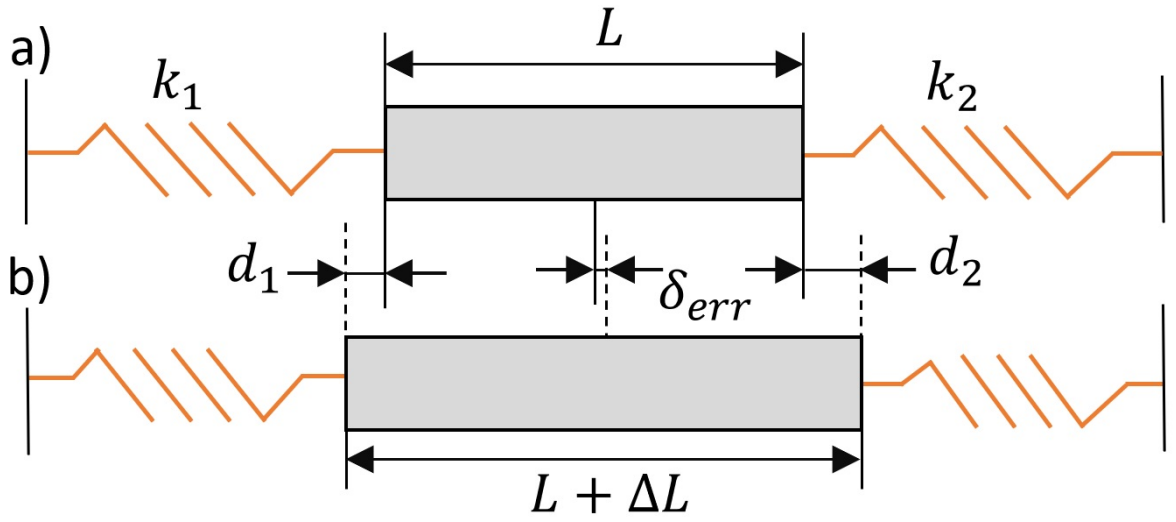

Figure 5.15: The positioning error in an a-thermal design due to a variation in spring stiffness. a) Before thermal expansion, the system is centred. b) After thermal expansion ΔL, the system is displaced by δ_{err}

Thermal settling time (✓)
As long as the design remains a-thermal for large temperature changes, radial stability is ensured and the thermal settling time is depending on this movement. Imperfections in material choices or flexure manufacturing introduce small shifts in the flexure stiffness and make the location of the thermal centre a function of temperature. This can be expressed analytically with help of the schematic in Figure 5.15. A 2D setup is assumed with two springs with a differential stiffness (5.1). When the centre block is expanding ΔL, the block moves δ_{err}. The sum of the compression of the springs is the total block expansion (5.2):

$$k_1 = c k_2 \tag{5.1}$$

$$d_2 + d_1 = \Delta L \tag{5.2}$$

The movement of the block is the difference between the compression of one spring and half the expansion (5.3):

$$\delta_{err} = d_2 - \frac{\Delta L}{2} \tag{5.3}$$

Using Newton's first law the force F from both springs is equal (5.4):

$$k_1 d_1 = k_2 d_2 \tag{5.4}$$

Combining these four equations results in an expression of the required homogeneity of the springs as a function of the expansion and required stability, see equation (5.5). Using δ_{err} = 12.8 nm and $\Delta L = 240\mu$m (corresponding to 300^{o}C temperature difference), c = 100.02%. Clearly the concept will not work for the entire temperature range, as the homogeneity would have to be extremely high. However, in the current design the temperature has converged to within a 25^{o}C temperature difference after six hours when omitting contact conductance. The new homogeneity requirement is 100.26%, which is still quite strict, but doable. The stiffness can be balanced by grinding the surface of the spring. Balancing of the temperature difference time-scale could be possible, but the main constraining factor is the overall high temperatures as equilibrium.

$$c = \frac{\frac{\Delta L}{2} + \delta_{err}}{\frac{\Delta L}{2} - \delta_{err}} \tag{5.5}$$

Vacuum at tip: (+)
The design is very open. The balls are small and installed far away from the tip, which has a full view to all the holes installed in the C1 lens. The vacuum is most likely limited by the C1 lens.

The equilibrium temperatures in this design will be high. There is only 6 points of contact between parts, and the extractor and emitter are very far away from each other thermally. Most of the heat transfer happens through radiation and outgassing can be expected to be higher because of this. Because of the very open design the requirements is still rated positive, but it is an additional risk to consider.

Field stability: (-)
Even though the overall length of the triple junction is very small, The field near the v-groove is considerable. Burying the triple junction is difficult without bringing the electrodes close to each other. Furthermore, in literature only one example was found of using an insulator point contact inside an electrostatic field [42], further creating question marks. Since there are no clear advantages to this design, it receives a slightly negative score.

Cost: (+)
The ceramic balls are custom made. The geometry is quite complex when the flexure is included, and the pre-stress would have to be provided by some kind of insulator spring. The insulator on top required for the pre-stress is also custom made. In this design the material of choice is not as much concerned with thermal conductance, but the permittivity at the surface as the triple junction is exposed. ZrO_2 TZP provides the flexibility but with a poor relative permittivity. Macor may be too prone to cracking to risk making it into a flexure but has great relative permittivity. In any case the material chosen does not have to be incredibly expensive to make the design work, see Table 5.2. As some custom insulators are expected in every design and the 6 ceramic balls are copies from each other, the cost is rated positively.

5.2.2. Concept 2: Fused insulators

Concept 2 focusses on thermal conduction between parts, with reduced thermal expansion sensitivity. It does this by using three thick rectangular pillars placed in between the emitter seat and extractor, and between the C1 lens and aperture seat, see Figure 5.16. The system is overconstrained, and therefore manufacturing precision is extremely important. A softer material with a decent yield strength could be used in between the insulator and lens if the stresses are found to be too high. UHV compliant aluminium foil could be a good candidate for this. It does tend to be a worse electrode material. The insulator is bonded onto the electrodes using a process called vacuum diffusion bonding. The result is a fully cross-sectional 'weld' without any of the components entering liquid phase [18]. This also removes any thermal contact resistance. As this process happens in a heated vacuum, the bond created has very little porosity compared to normal surface to contacts. However, more research will have to be done to find all the fine intricacies involved in this process. The thermal insensitivity is created by placing the pillars around the optical axis with equal spacing. The insulators' cross-section is rectangular, with the long side facing the optical axis. This created a lower stiffness in radial direction, and ensures the optical axis stays in place for temperature changes. In other words, the system is a-thermal.

Stability (✓) Long term stability between the emitter tip, extractor/aperture and C1 lens is achieved by utilizing the a-thermal feature of this set-up. The diffusion bonding process result in a virtually perfect thermal contact and thus the heat flow through the flexures is allowed to be much greater. The temperatures can be expected to be much smaller. The very low deflection combined with a smaller radial stiffness ensures low stresses near the base of the insulators. There is no risk of stick slip behaviour as the parts are bonded together, removing the need for pre-stress the lens stack. The axial stability at the extractor follows a smaller thermal loop (emitter -> emitter seat -> insulator -> extractor) and the temperatures are lower, so the movement will easily fall within limits.

Short term stability is limited by the stacked pillars acting as a spring in series. The stresses created by bending the pillars has to be balanced against the eigenfrequency of the system. The setup is quite stiff in all direction. In a simple 3D COMSOL model the thermal expansion of this concept was tested and the eigenfrequency was analysed for the same geometry. It was easy to reach a sufficiently high eigenfrequency [redacted] while keeping the stresses quite low (<10MPa).

Thermal settling time (✓) Because the design is a-thermal, the thermal settling time is largely determined by finding how much parasitic movement can be expected due to variations in the geometry or material properties. In the first concept an equation is derived for the required homogeneity between the leaf springs which are installed (5.5). By having lower overall temperatures in the equilibrium and thus also lower temperature differences, the temperature will converge faster compared to concept 1. For reference, the current design with modelled imperfect contact is only 7K from equilibrium at [redacted]. The 25K temperature window mentioned in concept 1 is already reached at only 1 hour. Using the 7K for expansion, the required homogeneity is 101.15%. By precision grinding the width and thickness of the pillar, the stiffness can be accurately

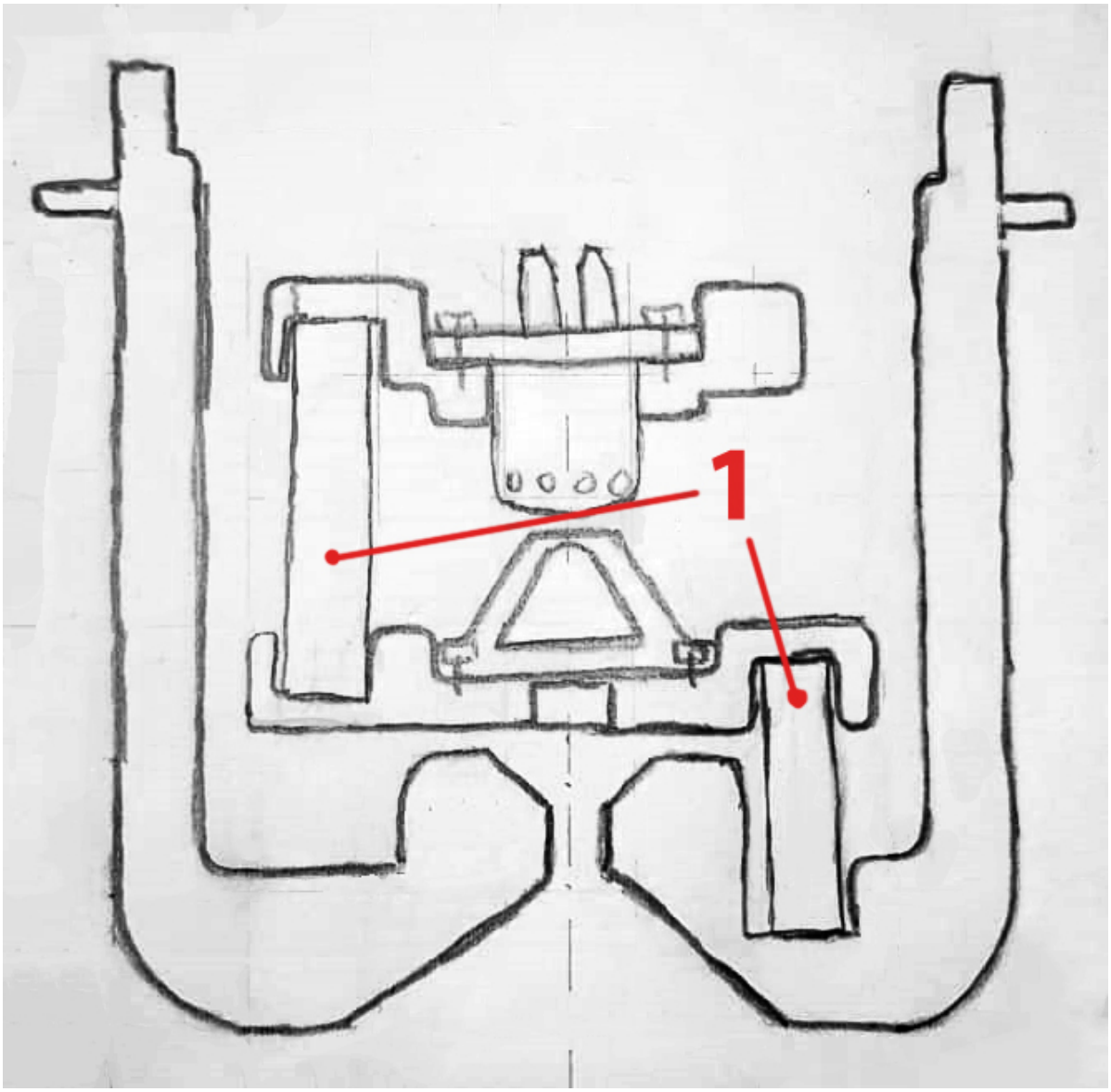

Figure 5.16: Cross-section of the second concept. 1) One of the pillar connecting the lens elements. By having a great thermal conductance, the expansion is limited, and stresses can be absorbed at the connection

balanced.

Vacuum at tip: (++)

Compared to the first concept, the insulators take up field of view between the tip and the C1 lens. The significance is most likely small for the pressure at the tip if placement in front of a C1 lens hole can be avoided. Thanks to the direct and good connection between electrodes without much contact resistance, the thermal conductance is improved. Overall, lower temperatures can be expected which will reduce outgassing. The concept gets an excellent rating.

Field stability: (o)

The insulators are long, and by using a buried triple junction the emission can remain low. However, there is risk involved in the new process. If the diffusion bonding introduces porosity in the bond or created a sharp metal transition near the triple junction the field stability could be very poor. Research on these topics is performed but generally behind closed doors (C. Zonnevylle, personal communication, June, 2020). Therefore it is difficult to ascertain whether this will work based on literature. The upside is that there is more also more possibility in creating a great and stable triple junction. The concept receives a neutral rating.

Cost: (- -)

The shape of insulators and electrodes are relatively easy to manufacture using common manufacturing techniques, but require very high tolerances. The fusion of the two with a possible additional metal layer in between is much more complex. There is no expertise on this area in the company. As the triple junction should be managed carefully, research should be done to find out how the fusion process should be performed. This development cost is unique to this design. On top of that, manufacturing and assembly is difficult as the design is statically over constrained and the components all have a high Young's modulus. The concept receives a very poor rating.

5.2.3. Concept 3: Buried insulators

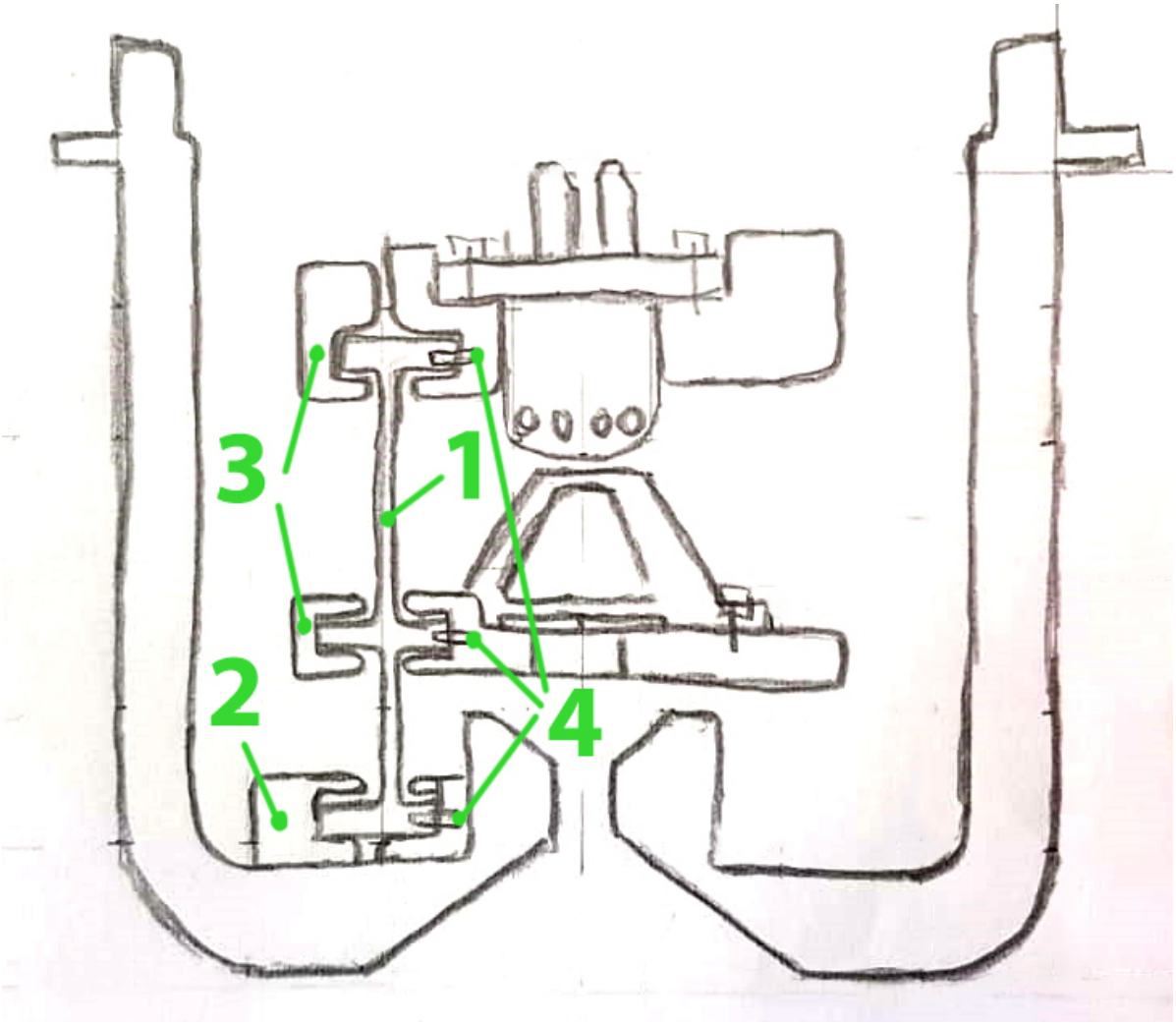

Figure 5.17: Cross-section of concept 3. 1) Monolithic flexure with thick ends. 2) New bottom electrode which is bolted on. 3) Insulator clamps with overhang. 4) Dowel pins for alignment and preventing creep.

The third and final concept utilizes leaf flexures, see Figure 5.17. They are placed in between electrodes, made from insulating material. The mounting is simply the clamping of the insulator at the electrode. This allows the insulators to be made from three parts instead of six. It improves thermal conductance and simplifies the construction. For ideal thermal conductance, the leaf spring has a constant cross-section along its length, without tapering or a notch to relieve one DoF. The mount includes one dowel pin at the emitter seat and aperture seat. When assembling, the insulator can be placed onto the dowel pin, providing it with 1 rotational DoF. this way all the minor manufacturing imperfections can be caught without large internal stresses. The bottom insulator mount includes one more dowel pin in a slot to keep the flexure upright. After the insulators are all placed onto the dowel pins they are clamped, solidifying their position.

Stability (✓)

The a-thermal properties of the set-up provide radial thermal stability. The extractor stability requirement is easily reached thanks to the identical thermal loop as concept 2. By pressing the parts together the thermal contact is decent and such the temperature difference are low. As for short term stability, optimizing for the eigenfrequency is critical. The mass is minimized and the stiffness is maximized, while keeping the stresses and forces due to thermal expansion inside the system minimal. The forces from the flexures are in the direction normal to the contact surfaces so there is little risk of stick-slip behaviour.

Thermal settling time (✓)

A very similar story to the one in concept 1 is relevant here. The temperature will be lower due to the improved thermal conductance. The thermal settling time can easily be achieved if the springs are balanced.

Vacuum at tip: (+)

The design is very open. The three leaf flexures do not have a major influence on the particles ability to escape. The temperatures are reduced by having decent thermal contact and direct connection between components, even if the flexures will have a more thermal resistance thanks to to smaller cross-sectional area. Outgassing will be quite low compared to concept 1. A downside of this idea compared to the other two is that there are many clamping surfaces created. This can be mitigated by drilling evacuation holes, but increased outgassing is unavoidable. The rating given to this concept for vacuum performance is positive.

Field stability: (++)

A major advantage of this concept is the cover on the triple junction. By installing the insulators radially the electrode can run on top and below the point of contact, greatly reducing the local field. This is done for all three electrodes. Electrode spacing is pretty good. Overall the performance of this concept performs the best among the three and receives an excellent rating.

Cost (+)

Both the insulators and electrode do not require special manufacturing techniques. The mounting is done manually, and may require some jigs or other special tools to be made once. There is little development cost required compared to concept 2. The material choice is quite flexible, but if AlN is used the cost can go up significantly. Combining these factors, the cost rating is positive.

5.3. Concept selection

All three concepts comply with the requirements and could be used. However, from the secondary objectives (Vacuum at tip, Field stability and Cost) shown in table Table 5.3 it should be clear that the third concept has the highest overall score. All concepts would provide enough for the vacuum requirements. The buried insulator of concept three takes the top spot when considering field stability. In cost, it does not have any major risks involved and development needed is minimal. Therefore concept three is continued. In the next chapter a 3D CAD model is presented, solving more practical aspects in this concept. This is still a conceptual design, and many small details are not solved yet.

Name	Stability	Thermal settling time	Vacuum at tip	Field stability	Cost
1. Ceramic balls	✓	✓	+	-	+
2. Fused insulators	✓	✓	++	o	- -
3. Buried insulators	✓	✓	+	++	+

Table 5.3: Summary of the three concepts.

6

Concept design

After selection of the concept (Buried insulators) a concept design was made in CAD. This is shown in section 6.1 where several details are provided. The flexure performance as a result of temperature variation is presented in section 6.2. The vacuum performance is estimated in section 6.3. It is stressed here that this is a CAD model based on a concept, and is not meant as a detailed design which claims to solve all the engineering problems.

6.1. Design considerations

The CAD model provides a visual aid to see how a design with the final concept could look like. It includes the design considerations outside the main concept as explained in section 5.1. The design as from the outside is illustrated in figure 6.1. Cross-sections are provided in the figures 6.2 to 6.5. This section will be dedicated to walking through the several solutions that were implemented with the cross-sections as a guide.

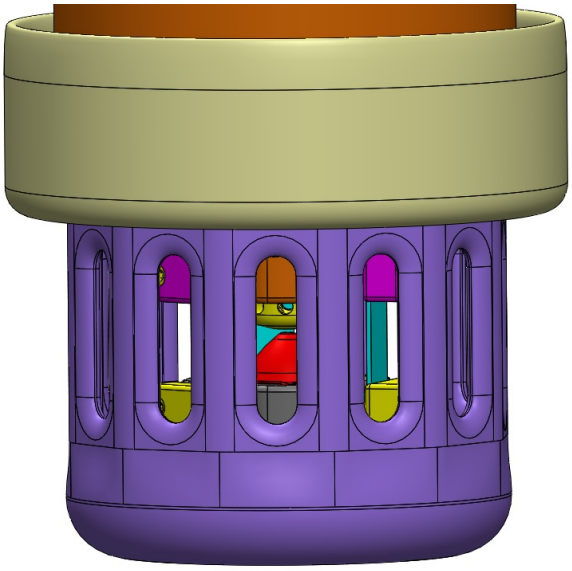

Figure 6.1: Outside view of the CAD model

We are starting with Figure 6.2, representing the cross-section as found in Figure 5.17. The figure shows the general working principles: The light blue double leaf spring, connected to the electrode and with a singular dowel pin in the top two. The swept back extractor (A) clearly shows the drastically improved viewing area of the tip. The gun lens is attached to the HV insulator by using the system (B) suggested in subsection 5.1.3. The connection with the aperture seat also ensures the aperture cannot escape (C). The C1 lens is the one conceived in subsection 5.1.2 with added features (D).

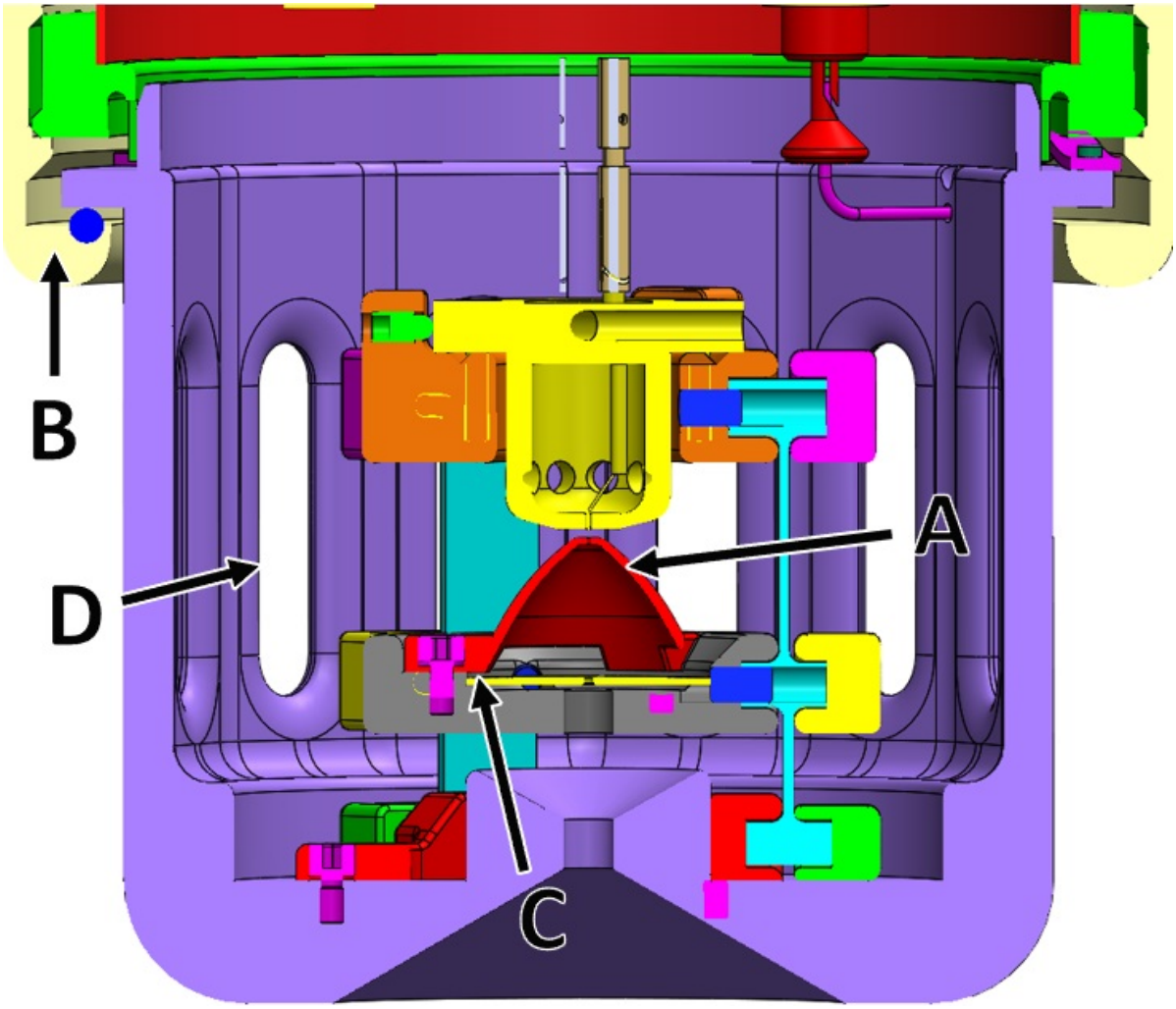

Figure 6.2: Cross-section. A: Swept back extractor geometry. B: HV insulator – gun lens interface. C: The aperture is held in place by stacking the extractor on top. D: Custom fillet shape on the C1 lens slots.

Figure 6.3 zooms in on the top side of the assembly. The aperture seat wire (E) goes up on the side of the electrode and bends inward slightly before inserting into the HV insulator connection. The inwards deflection is required for spacing of the connections. The C1 lens wire (F) is simple; it is similarly flattened at the electrode side, and a grub/set screw is used to secure its position. Even though the screw has sharp features, the local field remains limited as it is buried inside the lens. This principle is used for more bolts used in the design. The connections for the emitter are the off the shelf connections as discussed in subsection 5.1.5 (G). Their other end is connected to a HV insulator interface part which is not modelled in this design. Finally visible in this cross-section is the emitter centring screws (H). These are used in a similar way to the previous design to fix the position of the emitter in X and Y position. In this design the position can be aligned with respect to the aperture. This is possible because the aperture and emitter do not need to be installed into the C1 lens for their position to be determined. Therefore the alignment can be done outside the C1 lens, where there is much more possibility to reach and see the relevant areas for alignment. By having this feature the tolerances from parts connecting the emitter seat to the aperture can be loosened as is it corrected post production.

Next up is figure 6.4. This shows the design while the C1 lens is hidden, giving a good overview of the construction that will be inserted. Here it is clear to see the extractor being bolted onto the aperture seat (I). This view also shows the double dowel pin at the bottom (J). One defines the position of the leaf flexure, and the other is installed into a slot to define the rotation.The shape of the flexure clamp is pretty clear here (K). It is a simple rectangular box with round edges such that manufacturing is kept simple. The bolts are buried inside to minimize the field near the sharp edges. If this is found to be a problem, the sharp edges

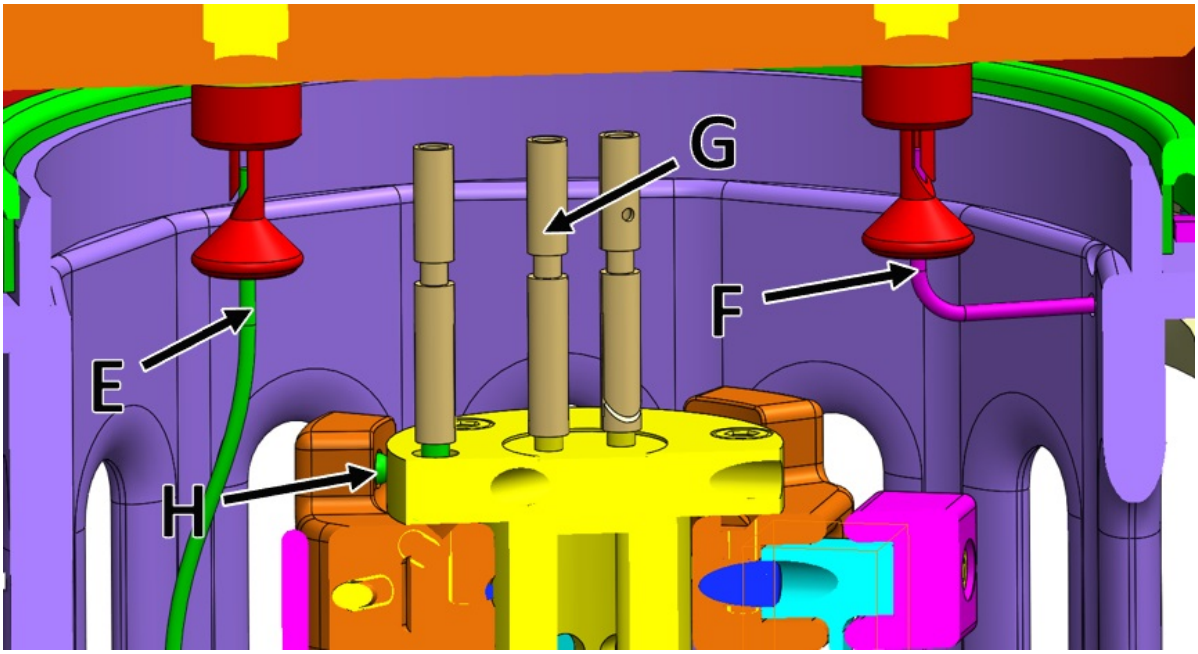

Figure 6.3: Cross-section. E: Extractor/aperture wire connection. F: C1 Lens wire connection. G: Emitter off-the-shelf parts connection. Connection to the HV insulator is not included. H: Emitter alignment set screw.

of the bolt can be rounded with a 0.5mm corner rounding end mill. Finally, the aperture seat wire (L) is not inserted directly next to this bolt, but at a slight angle. This allows the operator to reach the bottom electrode bolts when installing it into the C1 lens. The green wire reaches far enough such that the extractor is used to determine the rotation of the wire through the flattened face.

The final cross-section is Figure 6.5. This shows a flat cross-section of the emitter seat. Here you can clearly see that the flexure is only connected to the dowel pin and its end surfaces (M). By doing so the triple junction is hidden as far as possible away from any external field. It is not included for every hole in the CAD model, but here the vacuum venting holes are shown for blind holes which are closed off with a bolt (N). This should be done for each heavily closed off area to prevent virtual leaks. Once again the dowel pin can be seen here as inserted in the emitter seat (O). The flexure uses it as an initial guide and the dowel pin also provides some pre-stress to the flexure such that its relative position is not at risk of travelling thanks to temperature variations or vibrations. This idea is shown in Figure 6.7 but is not modelled in CAD. Moving on to the bolts (P), as they have a specific shape in order to comply with the local field stability. The bolt starts at the clamp, and moves through the vacuum to connect to the emitter seat. The exposed part of the bolt is smooth and does not have any thread. The thread would cause sharp points in the field and would drastically reduced the field stability. A final note for this cross-section is that the distance between the C1 lens and the other electrodes has been iterated on such that this distance is as large as possible (Q). The minimum distance is higher than the distances found in the design currently in the EBPG.

The electrodes have quite a lot of elements and tasks they need to fulfil. To show their shape properly Figure 6.6 has them illustrated. One of the most important aspects taken into account is the viability of these design; can it be made? Of course the tolerances can be loosened if a smart concept is conceived, but a bunch of 3D shapes will not make the constructor happy. In these electrodes the shapes are kept simple. Almost all operations on these parts can be performed on a lathe and 3-axis CNC mill with simple jigs. The fillets are kept simple such that the shape can be made with a simple pass of a corner rounding end mill. Some areas require more enhanced manufacturing machines to be time efficient and these are shown with the red circle. These can most likely be optimized such that also they are easier for the machine operator.

The design can be put together without much risk of damage or scratches. Construction of the design is as follows:

1. Install dowel pins in the three electrodes (emitter seat, aperture seat, bottom electrode).

2. Install suppressor wire extension on emitter.

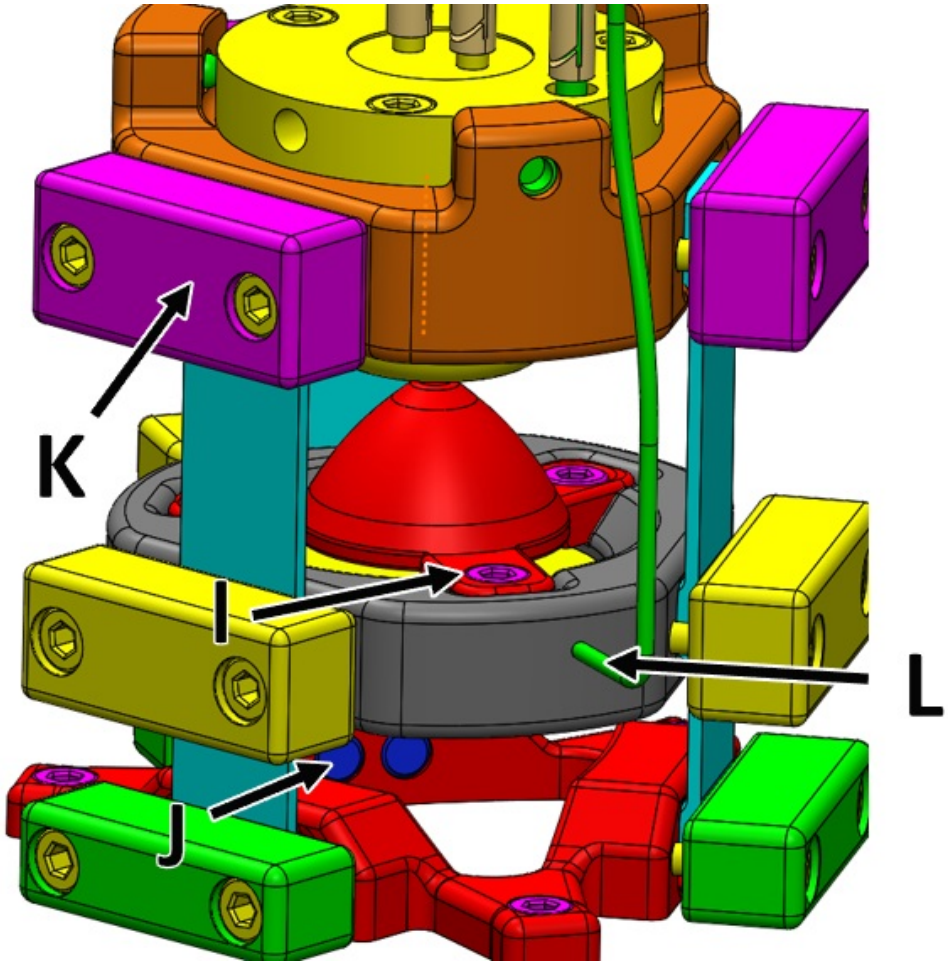

Figure 6.4: The design with the C1 lens hidden. I: The extractor is bolted onto the aperture seat. J: The bottom flexure endpoint has two dowel pins to constrain rotation. K: The flexure clamps have rounded and buried bolts to minimize discharge risk. L: The insert location of the aperture seat wire. The flat spot touches the extractor, forcing the upright orientation.

3. Install emitter in emitter seat.
4. Install aperture in aperture seat.
5. Insert aperture seat wire and install extractor, ensuring a fastened wire.
6. Insert flexures onto the dowel pins.
7. Clamp bottom clamps to the bottom electrode.
8. Softly clamp aperture seat and emitter seat clamps, tighten equally afterwards.
9. Align the emitter tip with the aperture using a microscope and alignment jig (not modelled).
10. Install electrode assembly into C1 lens.
11. Install C1 lens wire and secure with set screw.
12. Install dowel pins and pre-stress springs on C1 lens edge.
13. Push C1 lens slightly into kovar spring nest. Ensure wires are inserted into the female counterparts.
14. Install HV ring such that the gun lens is resting on the ceramic balls. Tighten HV ring until the mechanical stop is reached.

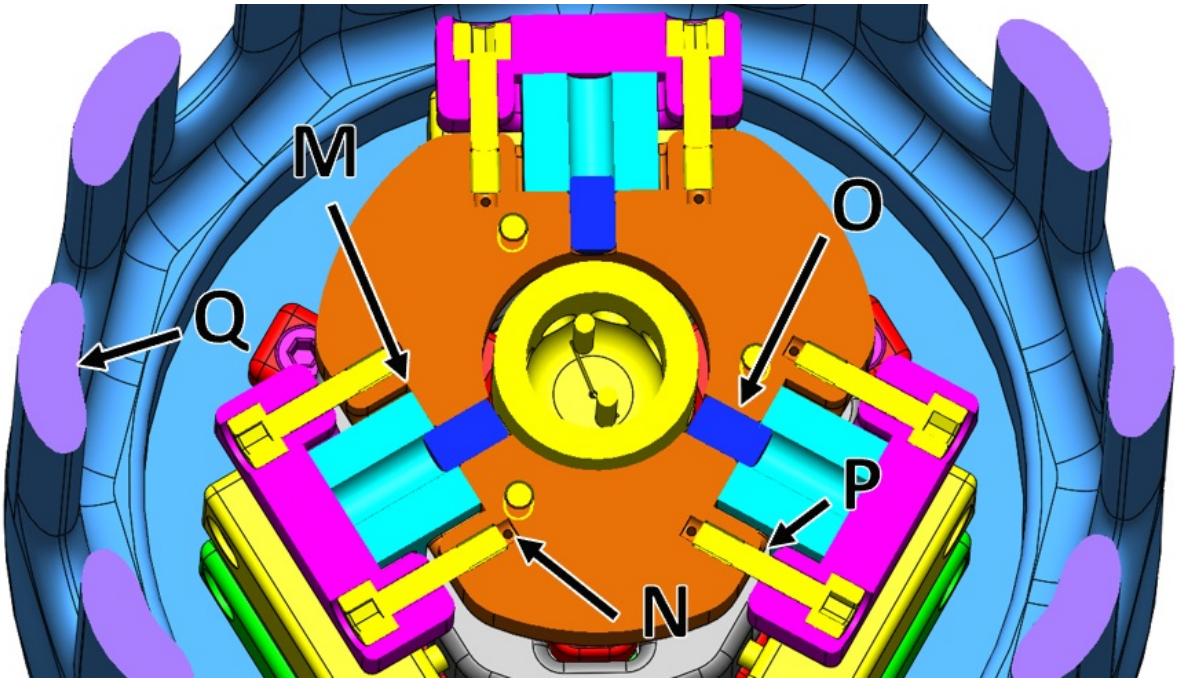

Figure 6.5: Horizontal cross-section through the emitter seat. M: The triple junction should be buried as much as possible. It only touches the electrode at the ends of the flexure endpoint. N: Enclosed holes have vacuum outgassing holes. O: The emitter and aperture have a singular dowel pin for a rotational DoF during installation. P: The bolts are smooth in between the clamp and the electrode such that electron emission is minimized. Q: Distance between the C1 Lens and the other electrodes is higher than the current design.

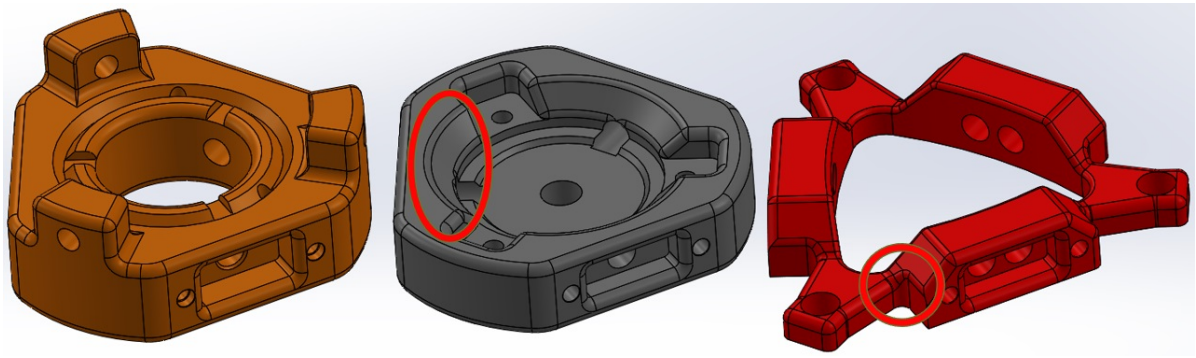

Figure 6.6: A view of the three electrodes. Manufacturing complexity has been taking into account in the design of the electrodes. Still improvements in this area could be made if necessary, especially in the indicated areas.

6.2. Flexure tuning

The eigenfrequency of the system can be quickly found through a simple simulation on COMSOL. For this simulation the connection from gun lens to HV insulator is assumed stiff, such that all vibrations are transmitted perfectly. The C1 lens is held fixed, and the eigenfrequency analysis shows that for a flexure thickness of 0.8mm the first eigenfrequency is determined by the flexures between emitter and aperture at 1173 Hz, see Figure 6.8 for the mode shape. The model could not handle the bolts inside the clamps properly, so these were removed. As you can see by the mode shape, these would provide some additional stiffness to the first eigenfrequency. Nevertheless the first eigenfrequency of the system can be increased by improving the stiffness of the flexures. By increasing the thickness to 1mm the stiffness of a singular leaf flexure in its normal direction is increased by a factor of $(1/0.8)^3 \approx 2$, which lifts the eigenfrequency above 1200 Hz. The second eigenfrequency is at around 2000Hz and is also related to the flexures. If Al_2O_3 is chosen as material for example, the stresses within the flexure remain acceptable up to a strain corresponding to 400K of temperature difference between the emitter and aperture seat, which is way above the requirement. This is verified by modelling a simple 2D flexure in COMSOL and finding the maximum strain up to the yield strength of the

Figure 6.7: Pre-stress idea by using a dowel pin with a slot cut in. The top side provides a reference surface, while the bottom side provides a spring force to the flexure. The flexure hole is not quite circular, but has a slightly decreased radius at the bottom so it interferes with the dowel pin.

material, see Figure 6.9. Choosing materials such as AlN will increase the margin even further.

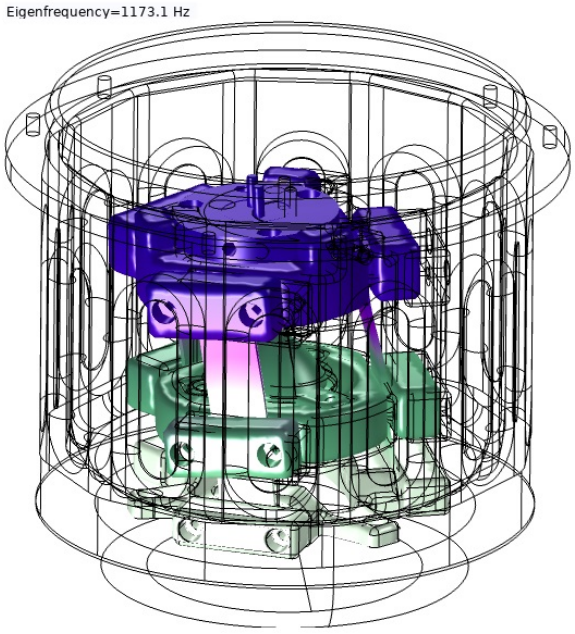

Figure 6.8: The mode shape of the first eigenfrequency. The shape can also be rotated 120 or -120 degrees

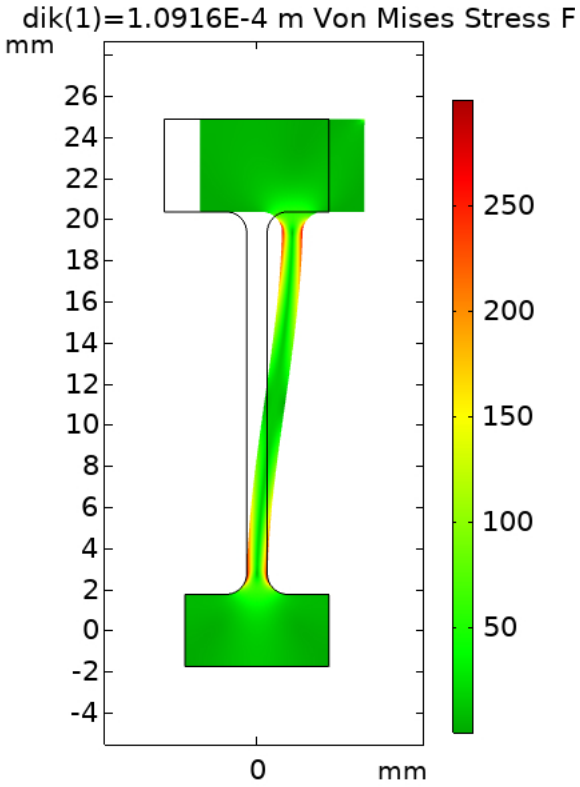

Figure 6.9: COMSOL viewport of the top flexure (Al_2O_3) at maximum strain before yield

6.3. Vacuum simulation

The design was entered into CERN Molflow similar to subsection 2.2.2. Some components were removed from the CAD model as they were not compatible with the inversion of the geometry. The result is shown in Figure 6.10 and compared with the current design. From the reduced chamber vacuum level it can be seen that the amount of outgassing has decreased. As the outgassing input is a constant per unit of surface area, the total surface area must have decreased. The tip vacuum has reduced from 8.5 times the chamber level to only 2 times. At the tip height the vacuum level is consistent. It is only inhibited by the C1 lens and the flexures

indicating that these components are the limiting factor to reducing the vacuum at the tip even further. By this heavy reduction of the local tip vacuum, a longer lifetime can be expected as is discussed in section 2.2.

This simulation does not give the full picture of the vacuum performance. It is only useful as a comparison to the previous design, but it does not take into account virtual leaks caused by clamped surfaces. Care should be taken to allow trapped air to escape through a simple drilled hole or to minimize these air traps in the first place. Furthermore the simulation inputs are simple and not completely accurate. Every material holds its own outgassing properties, especially if their temperatures are increased. The vacuum near the tip can be expected to be higher as the 1800K tungsten filament is expected to increase the local vacuum level. In any case, as the new design appears much improved advanced techniques as provided in section 2.2 to improve outgassing apart from the baking procedure do not seem necessary. There were no large virtual leaks that had to be removed in CAD, which is in sharp contrast with the current gun lens, where it took a long time to find and remove virtual leaks.

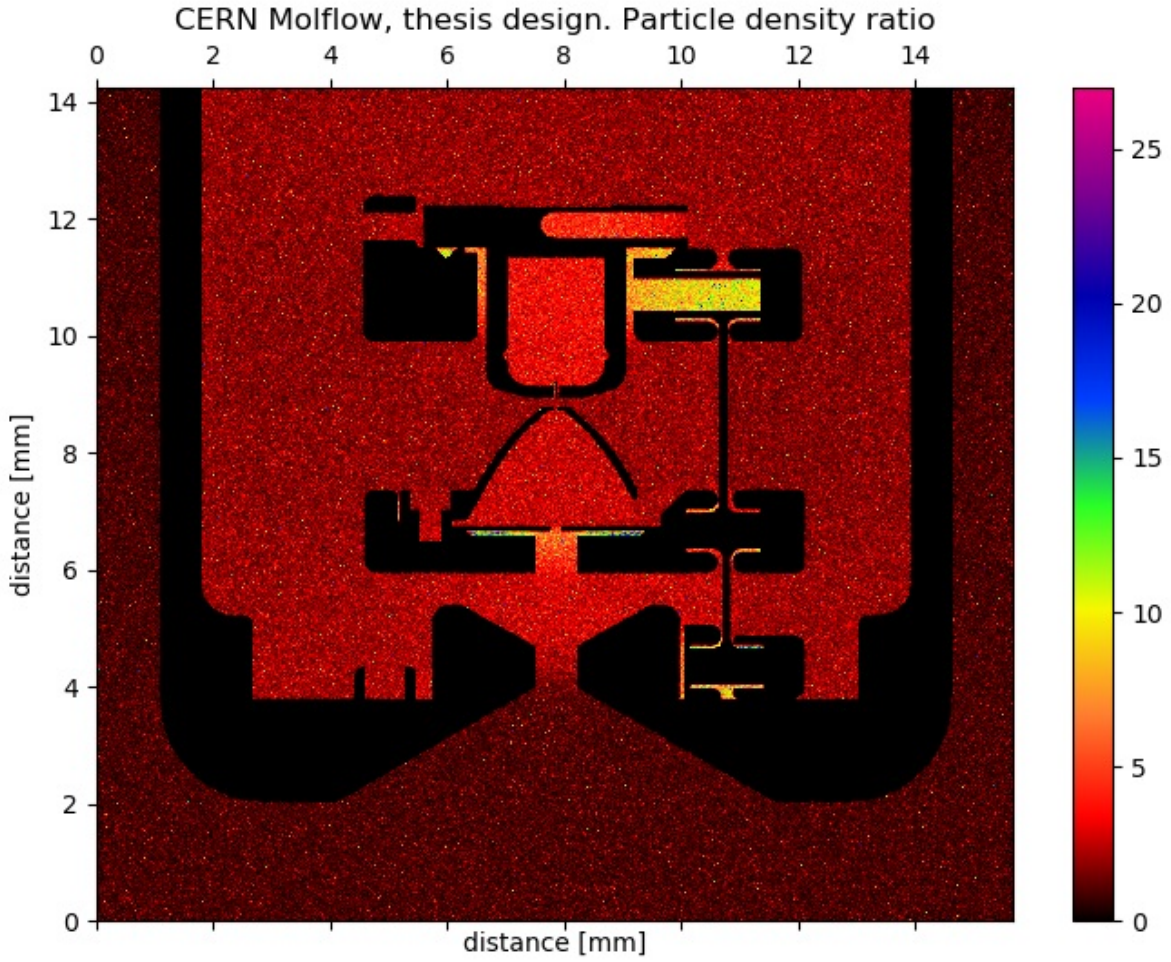

Figure 6.10: Simulation result of the concept design. Compared to Figure 2.8 the vacuum at the tip is greatly reduced. The blocking of electrodes is the biggest cause of this. This does come at a cost, as the insulators are now exposed to electrons exiting the emitter tip.

6.4. Requirement satisfaction

The required stabilities as given in **??** can all be achieved as is proven in chapter 5 and this chapter. If similar interface tolerances are used as compared to the current design the tolerances in the requirements are also easy to meet. As mentioned before the position of the emitter is determined by the alignment screws. These can be used to correct for unacceptable misalignments in the system. The roundness of the electrodes' inner diameter was discussed with the manufacturing party and is feasible.

Stability requirements are met by considering a couple of things. The X|Y drift is minimized by greatly

reducing the thermal sensitivity. The stiffness of the triple leaf spring setup is high enough to avoid resonance with any other components attached to the optical column. Lastly, by lowering the overall temperatures, Z drift through thermal expansion is reduced to levels far below the requirements.

The other requirements as given in Table 3.1 are also all achieved when this concept design is worked out into a full design. The beam stability requirements are achieved by complying with the mechanical stability requirements. The 'Module exit current' is achieved simply by keeping the aperture geometry with respect to the emitter the same. The 'Weight', 'Adjustable Optics', 'Forbidden Materials' are checked by verifying it with the concept design pictures and descriptions as shown above. It is uncertain whether the 'Cost of the module' remain equal or reduced, but the concept which was chosen did not require difficult manufacturing techniques or need additional research to make it work. It remains to be seen whether the 'Field stability' requirement is met, it is dependent on even the smallest details in a design which is out of the scope of this thesis. This can best be verified in practice. During the design much care was taken to improve the robustness, especially in the case of the triple junction. The 'Achievable chamber pressure' is possible if no virtual leaks exist in the design, which have not been found in the concept design. The 'Vacuum at the tip' is achieved as shown in the previous section. Finally, the 'Thermal settling time' is achieved when the flexure stiffness homogeneity is high enough. This can be ensured during the production phase.

7

Discussion

Throughout the thesis a great deal of effort went into ensuring the performance in all areas of physics. But with the limited manpower and time, a concept design is unable to solve in detail the problems that inevitably arise. Below are some unsolved aspects of the design which should/could (changing per aspect at the reader's discretion) be investigated before this concept can be called a fully detailed design.

First, the rotational symmetry has been lost to a certain degree by introducing the triple flexure system. The severity of this should be investigated further by exposing the design to an optical simulation. If the a-symmetry does not comply, the design can be altered by the introduction of an 'asymmetry shield' where a rotational symmetric shape is added onto the electrode to block the cause of asymmetry.

Next the vacuum performance of the design is hard to estimate. As stated before the vacuum level can be ruined by a simple human error. Even in a perfect world, the software to accurately estimate the vacuum levels with ease does not exist at this moment. It is a matter of waiting for a software package to be released which allows complex models such as these to be used and analysed. Capabilities to allocate complex outgassing properties to each surface, preferably time-dependent are necessary if an accurate result should be found.

In the concept design as shown in Figure 6.4 a potential problem is shown quite clearly: the electrons coming from the emitter tip are able to travel towards and charge the insulators. Impinging electrons on charged insulator surfaces can cause a secondary electron emission avalanche (SEEA) (depending on their energy [11, 53]) which poses a risk for breakdown events as gas particles are desorbed and ionized [38]. Several solutions could be implemented. For instance, the profile of the flexure can be made more complex such that the secondary electrons bouncing across the surface are stopped, as is done in [59] with ribs. This reduces the surface charge near the cathode triple junction (called field relaxation) which is the main source of new electrons. If the wave of electrons coming from the tip is high, this option does not solve the main problem. In that case the path of the electron from the tip to the insulator can be blocked off by use of the electrodes. This should be done with both the emitter seat and either the extractor or aperture seat. Rotational symmetry can be preserved by doing so, but will incur a significant cost in the local tip vacuum.

The transient behaviour of the design is important to determine the thermal settling time of the design. In the concept phase it was determined that all concepts would comply with the thermal settling time requirements. However this was not verified with a 3D simulation of the transient. The electrodes should heat up at around the same rate to quickly stabilize their temperature difference. This can be tweaked by changing the mass and surface area of the electrodes for example. The material choice, especially for the insulator is determinant in how well the transient behaviour of the electrodes is coupled. Further investigation in this area should be done to ensure a low thermal settling time. However anything below 6 hours is unnecessary as the emitter will need this time to stabilize its tip geometry. Therefore a stable beam can not be achieved before this time.

The short term dynamic behaviour of the gun lens and the column as a whole is still poorly understood. Steps have been taken to investigate some of the effects [55], but more work should be done if designs are to be made with this in mind. Requirements around the topic of vibrations and stiffness were vague out of necessity as very little was known about it.

The tuning of the flexures can most likely be done to a very high accuracy with the right setup, but will also result in an increase in cost. The accuracies in stiffness that can be achieved with low or high effort are

not clear and further work needs to be done or discussions need to be had with the manufacturing parties to find what is possible.

The flexures in the concept design are relatively simple. If the thermal conductance is to be increased, the central part of the leaf spring can be thickened, as the majority of the strain occurs at the endpoints of a leaf flexure as seen in Figure 6.9. This would require new FEM simulations to ensure the ceramic can absorb the increased stresses at the endpoints.

Finally, discussions with the manufacturing team should continue up to the point of finishing the design and making the first prototype. Costs of the design were kept down by using simple shapes-, but improvements can always be made if it is analysed more properly from different angles of expertise.

8

Conclusions

By combining the practical knowledge of a mechanical engineer with the theory of gun lenses, a new concept design was made for the gun lens of Raith's EBPG. Without mechanical requirements, the engineer is unable to formulate a design which can be proven to work. Therefore this design process started at the fact that the optical performance is always dependent on the mechanical positioning of its electrodes. By making this translation through optical simulations clear mechanical requirements could be formulated from what Raith desired from its optical column. As the gun lens is focused around an 1800K tip the thermal aspect of the design posed the largest challenge in finding something that could remain stable with such large temperature changes and within a short time-frame as well. By including the theory on gas discharge mechanics and vacuum science a concept was conceived which not only complied with the mechanical requirements, but also improved upon the aforementioned aspects drastically. As for the mechanics a stacked triple leaf flexure was used to give the design an a-thermal centre. The improvement on discharge is hard to quantify, but a lot of tools and methods have been introduced to allow this design to reduce the risk of field breakdown dramatically. The largest contributor is the burying of the triple junction, which is a notorious source of electron emission and a cause of gas discharge. The vacuum at the tip was improved by 86% according to simplified Monte-Carlo simulations. Overall the concept design presented in chapter 6 provides a practical answer to the original research question and is a strong reference point for a multidisciplinary team to start from and formulate an even better design.

Bibliography

[1] Francesco Avallone. Application of non-intrusive experimental techniques to roughness-induced in hypersonic flows. 2015.

[2] Mahzad BastaniNejad, Abdelmageed A. Elmustafa, Eric Forman, Steven Covert, John Hansknecht, Carlos Hernandez-Garcia, Matthew Poelker, Lopa Das, Michael Kelley, and Phillip Williams. Evaluation of electropolished stainless steel electrodes for use in DC high voltage photoelectron guns. *Journal of Vacuum Science & Technology A: Vacuum, Surfaces, and Films*, 33(4):041401, jul 2015. ISSN 0734-2101. doi: 10.1116/1.4920984.

[3] A. V. Batrakov, A. B. Markov, G. E. Ozur, D. I. Proskurovsky, and V. P. Rotshtein. The Effect of Pulsed Electron-beam Treatment of Electrodes on Vacuum Breakdown. *IEEE Transactions on Dielectrics and Electrical Insulation*, 2(2):237–242, 1995. ISSN 10709878. doi: 10.1109/94.388246.

[4] Amrit S. Brah. *A detailed study of the mechanical and electrical aspects of microparticle impact phenomena*. PhD thesis, Aston University, 1977.

[5] Merijn Bronsgeest. *Physics of Schottky Electron Sources*. Pan Stanford Publishing Pte. Ltd., 2014.

[6] Aernout Christiaan Zonnevylle, Thomas Verduin, Cornelis W. Hagen, and Pieter Kruit. Deflection properties of an electrostatic electron lens with a shifted electrode. *Journal of Vacuum Science and Technology B: Microelectronics and Nanometer Structures*, 31(6), nov 2013. ISSN 10711023. doi: 10.1116/1.4826250.

[7] A. M. Clausing and B. T. Chao. Thermal contact resistance in a vacuum environment. *Journal of Heat Transfer*, 87(2):243–250, 1965. ISSN 15288943. doi: 10.1115/1.3689082.

[8] Comsol Inc. *COMSOL 5.5 [Computer Software]*. retrieved from https://comsol.com, Burlington, USA, 2020. URL `https://www.comsol.com`.

[9] Ben Cook, Merijn Bronsgeest, Kees Hagen, and Pieter Kruit. Improving the energy spread and brightness of thermal-field (Schottky) emitters with PHAST-PHoto Assisted Schottky Tip. *Ultramicroscopy*, 109(5): 403–412, 2009. ISSN 03043991. doi: 10.1016/j.ultramic.2008.11.024.

[10] D Coyne. LIGO Vacuum Compatible Materials. *LIGO Scientific Collaboration*, Advanced L, 2011.

[11] John R. Dennison, Alec Sim, and Clint D. Thomson. Evolution of the electron yield curves of insulators as a function of impinging electron fluence and energy. *IEEE Transactions on Plasma Science*, 34(5 II): 2204–2218, 2006. ISSN 00933813. doi: 10.1109/TPS.2006.883398.

[12] R.F. Egerton. *Physical Principles of Electron Microscopy*. Springer, Edmonton, BA, 2016. ISBN 9783319398761.

[13] Mohamed M El-Gomati. *Modern Electron Optics and the Search for More Light: The Legacy of the Muslim Golden Age*, pages 119–144. Springer International Publishing, Cham, 2016. ISBN 978-3-319-31903-2. doi: 10.1007/978-3-319-31903-2_6. URL `https://doi.org/10.1007/978-3-319-31903-2{_}6`.

[14] Engineering Toolbox. Emissivity Coefficient Materials, 2003. URL `https://www.engineeringtoolbox.com/emissivity-coefficients-d{_}447.html`.

[15] FEI. Thermo Fisher Scientific, 2020. URL `https://www.fei.com/`.

[16] ERWIN FRIED and FREDERICK A. COSTELLO. Interface Thermal Contact Resistance Problem in Space Vehicles. *ARS Journal*, 32(2):237–243, 1962. doi: 10.2514/8.5977.

[17] M. Gesley. On the design and effective strength of stigmators for electron beam lithography. *Journal of Vacuum Science & Technology B: Microelectronics and Nanometer Structures*, 9(6):2977, 1991. ISSN 0734211X. doi: 10.1116/1.585352.

[18] Thomas Gietzelt, Volker Toth, and Andreas Huell. Diffusion Bonding: Influence of Process Parameters and Material Microstructure. *Joining Technologies*, 2016. doi: 10.5772/64312.

[19] Raymond Gillibert, Jiao Qi Huang, Yang Zhang, Wei Ling Fu, and Marc Lamy de la Chapelle. Explosive detection by Surface Enhanced Raman Scattering. *TrAC - Trends in Analytical Chemistry*, 105:166–172, 2018. ISSN 18793142. doi: 10.1016/j.trac.2018.03.018. URL https://doi.org/10.1016/j.trac.2018.03.018.

[20] M. Haïdopoulos, S. Turgeon, C. Sarra-Bournet, G. Laroche, and D. Mantovani. Development of an optimized electrochemical process for subsequent coating of 316 stainless steel for stent applications. *Journal of Materials Science: Materials in Medicine*, 17(7):647–657, 2006. ISSN 09574530. doi: 10.1007/s10856-006-9228-4.

[21] C. Hernandez-Garcia, M. Poelker, and J. Hansknecht. High voltage studies of inverted-geometry ceramic insulators for a 350 kV DC polarized electron gun. *IEEE Transactions on Dielectrics and Electrical Insulation*, 23(1):418–427, 2016. ISSN 10709878. doi: 10.1109/TDEI.2015.005126.

[22] Okubo Hitoshi. Development of Electrical Insulation Techniques in Vacuum for Higher Voltage Vacuum. *XXIInd Int. Symp. on Discharges and Electrical Insulation in Vacuum*, 2006.

[23] Ideal Vacuum Products LLC. Power, Crimp Style, Push-On Connectors, for 0.05 in. dia. pin, Be-Cu, UHV Rated, 10-Pack, 2020. URL https://www.idealvac.com/Power/pp/P108805.

[24] S. S. Inayoshi, Y. Sato, K. Saito, S. Tsukahara, Y. Hara, S. Amano, K. Ishizawa, T. Nomura, A. Shimada, and M. Kanazawa. Chemical polishing of stainless steel for ultrahigh vacuum wall material. *Vacuum*, 1999. ISSN 0042207X. doi: 10.1016/S0042-207X(98)00422-9.

[25] Sukmin Chung Inkyu Chun, Boklae Cho. Outgassing rate characteristic of a stainless- steel extreme high vacuum system. *Journal of Vacuum Science & Technology*, 2636(April 1996), 1996.

[26] G.H. Jansen. *Coulomb interactions in particle beams*. PhD thesis, Delft Universiy of Technology, 1988.

[27] Burkhard Jüttner. Vacuum breakdown. *Nuclear Inst. and Methods in Physics Research, A*, 268(2-3):390–396, 1988. ISSN 01689002. doi: 10.1016/0168-9002(88)90541-4.

[28] B. H. Koek, T. Chisholm, A. J. v. Run, J. Romijn, and J. P. Davey. An electron beam lithography tool with a Schottky emitter for wide range applications. *Microelectronic Engineering*, 23(1-4):81–84, 1994. ISSN 01679317. doi: 10.1016/0167-9317(94)90109-0.

[29] Bert H. Koek, Thomas Chisholm, Julian P. Davey, Johannes Romijn, and Arnold J.V. Run. A Schottky-Emitter Electron Source For Wide Range Lithography Applications. *Japanese Journal of Applied Physics*, 32(12 S):5982–5987, 1993. ISSN 13474065. doi: 10.1143/JJAP.32.5982.

[30] Kruit. Introduction to charged particle Optics, 2010.

[31] Pieter Kruit, M. Bezuijen, and J. E. Barth. Source brightness and useful beam current of carbon nanotubes and other very small emitters. *Journal of Applied Physics*, 99(2), jan 2006. ISSN 00218979. doi: 10.1063/1.2162270.

[32] Derry Lappin, Abdolreza Rashidi Mohammadi, and Kenichi Takahata. An experimental study of electrochemical polishing for micro-electro- discharge-machined stainless-steel stents. *Journal of Materials Science: Materials in Medicine*, 23(2):349–356, 2012. ISSN 09574530. doi: 10.1007/s10856-011-4513-2.

[33] R V Latham. *High Voltage Vacuum Insulation BASIC CONCEPTS AND TECHNOLOGICAL PRACTICE*. ACADEMIC PRESS, Birmingham, 1995.

[34] N M Laurendeau. *Statistical Thermodynamics: Fundamentals and Applications*. Cambridge University Press, 2005. ISBN 9781139446181. URL https://books.google.nl/books?id=QF6iMewh4KMC.

[35] Minxu Li and H. F. Dylla. Model for water outgassing from metal surfaces. II. *Journal of Vacuum Science & Technology A: Vacuum, Surfaces, and Films*, 12(4):1772–1777, 1994. ISSN 0734-2101. doi: 10.1116/1.579004.

[36] H. Liebl and B. Senftinger. Low-energy electron microscope of novel design. *Ultramicroscopy*, 36(1-3): 91–98, 1991. ISSN 03043991. doi: 10.1016/0304-3991(91)90140-2.

[37] Md Abdullah A. Mamun, Abdelmageed A. Elmustafa, Marcy L. Stutzman, Philip A. Adderley, and Matthew Poelker. Effect of heat treatments and coatings on the outgassing rate of stainless steel chambers. *Journal of Vacuum Science & Technology A: Vacuum, Surfaces, and Films*, 32(2):021604, 2014. ISSN 0734-2101. doi: 10.1116/1.4853795.

[38] H. Craig Miller. Surface Flashover of Insulators. *IEEE Transactions on Electrical Insulation*, 24(5):765–786, 1989. ISSN 00189367. doi: 10.1109/14.42158.

[39] A. F. Mills. *Basic Heat and Mass Transfer*. Temporal Publishing, LLC, 2014.

[40] H Moscicka-Grzesiak and H Gruszka.] INFLUENCE OF ELECTROPOLISHING CU AND AL ELECTRODES ON PREDISCHARGE PHENOMENA AND BREAKDOWN OF VACUUM GAPS. Technical report, 1983.

[41] Viet Nguyen-Tuong. Vacuum outgassing of artificial dielectric ceramics. *Journal of Vacuum Science & Technology A: Vacuum, Surfaces, and Films*, 12(4):1719–1721, 1994. ISSN 0734-2101. doi: 10.1116/1.579043.

[42] Jon Orloff. *Handbook of charged particle optics*. CRC Press, 1997.

[43] Raith. High resolution lithography: EBL tool EBPG5200. https://www.raith.com/products/ebpg5200.html, 2020. URL `https://www.raith.com/products/ebpg5200.html`.

[44] Ari Riihim, Christina Yin Vallgren, and R Jyrki. Outgassing Studies of Some Accelerator Materials. 64, 2019.

[45] Y. Tito Sasaki. Reducing SS 304 and 316 hydrogen outgassing to 2×10-15torrlcm-2s-1. *Journal of Vacuum Science & Technology A: Vacuum, Surfaces, and Films*, 25(4):1309–1311, jul 2007. ISSN 0734-2101. doi: 10.1116/1.2734151.

[46] O Scherzer. Über einige Fehler von Elektronenlinsen. *Zeitschrift für Physik*, 101(9):593–603, 1936. ISSN 0044-3328. doi: 10.1007/BF01349606. URL `https://doi.org/10.1007/BF01349606`.

[47] Scientific Instrument Services. *SIMION® 8.1.1.32 [Computer Software]*. retrieved from https://simion.com, Palmer, MA, 2020. URL `https://simion.com/`.

[48] Yu P. Shlykov and Ye A. Ganin. Thermal resistance of metallic contacts. *International Journal of Heat and Mass Transfer*, 7(8):921–929, 1964. ISSN 00179310. doi: 10.1016/0017-9310(64)90147-4.

[49] Stephen A. Smee. A precision lens mount for large temperature excursions. *Modern Technologies in Space- and Ground-based Telescopes and Instrumentation*, 7739:77393O, 2010. ISSN 0277786X. doi: 10.1117/12.858038.

[50] Herman Soemers. *Design Principles for precision mechanisms*. Universiteit Twente, 2017.

[51] P. Spolaore, G. Bisoffi, F. Cervellera, R. Pengo, and F. Scarpa. The large gap case for HV insulation in vacuum. *IEEE Transactions on Dielectrics and Electrical Insulation*, 4(4):389–393, 1997. ISSN 10709878. doi: 10.1109/94.625353.

[52] Bert Suurmeijer. *Basisboek Vacuümtechniek*. Bert Suurmeijer, 1 edition, 2000.

[53] C. H.De Tourreil and K. D. Srivastava. Mechanism of Surface Charging of High-Voltage Insulators in Vacuum. *IEEE Transactions on Electrical Insulation*, EI-8(1):17–21, 1973. ISSN 00189367. doi: 10.1109/TEI.1973.299238.

[54] Unknown. Agilent Technologies UHV Seminar, 2011. URL `https://www.agilent.com/cs/library/training/Public/UHV{_}Seminar{_}Handbook.pdf`.

[55] S.A. van den Boogaart. Metrology design for improving the beam stability in an e-Beam Lithography machine. Technical report, Unversity of Technology Delft, 2020.

[56] T. Verduin, B. Cook, and Pieter Kruit. Influence of gun design on Coulomb interactions in a field emission gun. *Journal of Vacuum Science & Technology B, Nanotechnology and Microelectronics: Materials, Processing, Measurement, and Phenomena*, 29(6):06F605, nov 2011. ISSN 2166-2746. doi: 10.1116/1.3660798.

[57] Shu Watanabe, Satoshi Kurokouchi, Shigeki Kato, and Masakazu Aono. Achievement of extremely high vacuum in an electrolytically polished stainless steel vacuum chamber. *Journal of Vacuum Science & Technology A: Vacuum, Surfaces, and Films*, 16(4):2711–2717, jul 1998. ISSN 0734-2101. doi: 10.1116/1.581405.

[58] Db Williams and Cb Carter. Electron Sources. In *Transmission electron microscopy: a textbook for materials science*, pages 73–89. 2009. doi: 10.1063/1.2883909. URL http://books.google.com/books?hl=en{&}lr={&}id=dXdrG39VtUoC{&}oi=fnd{&}pg=PR10{&}dq=Transmission+electron+microscopy:+a+textbook+for+materials+science{&}ots=rNamNIuerI{&}sig=oplPlufRtVoHYT{_}z7HClfXPyG9U.

[59] O Yamamoto, T Hara, H Matsuura, Y Tanabe, and T Konishi. Effects of corrugated insulator on electrical insulation in vacuum. *Vacuum*, 47(6-8):713–717, 1996.

[60] Takanori Yasuoka, Tomohiro Kato, Katsumi Kato, and Hitoshi Okubo. Discussion of electrode conditioning mechanism based on pre-breakdown current under non-uniform electric field in vacuum. *IEEJ Transactions on Power and Energy*, 128(12):19–22, 2008. ISSN 03854213. doi: 10.1541/ieejpes.128.1445.

[61] Lixin Zhang, Mathijs W.H. Garming, Jacob P. Hoogenboom, and Pieter Kruit. Beam displacement and blur caused by fast electron beam deflection. *Ultramicroscopy*, 211(December 2019):112925, 2020. ISSN 18792723. doi: 10.1016/j.ultramic.2019.112925. URL https://doi.org/10.1016/j.ultramic.2019.112925.

A

Preceding literature study

See unredacted version for literature study